# The Application of Atomic Force Microscopy in the Surface Analysis of Polymeric Biomaterials

by Kevin Shakesheff

.

Thesis submitted to the University of Nottingham
for the degree of Doctor of Philosophy, November, 1995

The results presented in this thesis have contributed towards the following papers:

In situ AFM visualization of the degradation of melt crystallized poly(sebacic anhydride).
K.M. Shakesheff, M.C. Davies, A. Domb, C.J. Roberts, S.J.B. Tendler and P.M. Williams , *Macromolecules,* 28, 1108, 1995.

In situ imaging of polymer degradation in an aqueous environment.
K.M. Shakesheff, M.C. Davies, C.J. Roberts, S.J.B. Tendler, A.G. Shard and A. Domb, *Langmuir,* 10, 4417, 1994.

The release of protein from a poly(ortho ester) film during surface erosion studied by *in situ* atomic force microscopy.
K.M. Shakesheff, M.C. Davies, J. Heller, C.J. Roberts, S.J.B. Tendler and P.M. Williams, *Langmuir,* 11, 2547, 1995.

The degradation of a thin polymer film studied by simultaneous in situ atomic force microscopy and surface plasmon resonance analysis
X. Chen , K.M. Shakesheff, M.C. Davies, J. Heller, C.J. Roberts, S.J.B. Tendler and P.M. Williams, *Journal of Physical Chemistry,* 99, 11537, 1995.

Imaging silica particles by atomic force microscopy: A novel sample preparation method.
K.M. Shakesheff, M.C. Davies, D.E. Jackson, C.J. Roberts, S.J.B. Tendler, P.M. Williams, D.A. Barratt, V. Brown and R.W. Brown, *Surface Science Letters,* **304,** L393, 1994.

The imaging of poly(athylene oxide) sphemlites by atomic force microscopy.
K.M. Shakesheff, M.C. Davies, D.E. Jackson, G.J. Leggett, C.J. Roberts, S.J.B. Tendler, and P.M. Williams, *Nanobiology,* 3, 41, 1994.

Relating the phase morphology of a biodegradable polymer blend to erosion kinetics using simultaneous in situ atomic force microscopy and surface plasmon resonance analysis.
K.M. Shakesheff, X. Chen , M.C. Davies, A.Domb, C.J. Roberts, S.J.B. Tendler and P.M. Williams, *Langmuir,* 11, 3921, 1995.

The role of scanning proba microscopy in drug delivery research.
K.M. Shakesheff, M.C. Davies, C.J. Roberts, S.J.B. Tendler and P.M. Williams, *Critical Reviews in Therapeutic Drug Delivery,* in press.

Surface analysis of biodegradable polymer blends of poly(sebacic anhydride) and poly(DL-lactic acid).
Davies M.C, Shakesheff K.M., Shard A.G., Domb A.†, Roberts C.J., Tendler S.J.B. and Williams P.M., *Macromolecules,* in press.

Dynamic surface events measured by simultaneous probe microscopy and surface plasmon detection.
Chen X., Davies M.C, Roberts C.J., Shakesheff K.M., Tendler S.J.B., Williams P.M.,*Analytical Chemistry,* submitted.

## Abstract

When a polymeric biomatarial is employed within a living system an interface is created between the solid surface of the polymer and an aqueous environment. The processes that occur at this interface will determine if the biomaterial is accepted by the patient and often will determine if the specific function of the biomatarial can be achieved. Increasingly, novel biomaterials are expected to perform more sophisticated functions and, therefore, their surfaces must be designed to realize precise interfacial events, such as specific interactions with proteins and calls or controlled biodegradation.

To design polymeric biomaterials with specific surface properties it is necessary to develop surface analytical techniques that can accurately characterize these properties. The work described in this thesis has aimed to investigate the potential contribution of the atomic force microscope (AFM) to this characterization.

The advantages of utilizing AFM in the study of polymeric biomaterials lie in the ability of the instmment to visualize insulating surfaces at a high resolution within a variety of environments, including gaseous and liquid environments. Therefore, it is possible to image the nanoscopic organization of polymeric biomaterials within environmental conditions that are similar to the conditions encountered within living systems.

Initial studies have concentrated on imaging the surface morphology of poly(ethylane oxide) (PEG) samples in air. These studies highlighted the high resolution capability of the AFM on untreated polymer samples. On sphemlitic samples, the AFM has visualized the lamellar organization of crystalline fibres. These lamellae had widths of between 10 and 30 nm and height variations of less than 15 nm. The ability of the AFM to resolve such stmctures, without the introduction of an etching or staining procedure required by transmission electron microscopy, relies on the sensitivity of the instrument to changes in the height of the topography. This sensitivity has been further utilized to image polymer strands with recorded widths of 8 nm. This width represents an over-estimation of the tme dimensions of the strand due to the finite size of the AFM probe apex and using the circular probe model it has been calculated that the strands have tme widths of less than 0.8 nm, indicating that they are composed of one or two PEG molecules. Furthėr studies on PEG have demonstrated the

ability to control polymer surface morphology through changes in the temperature of thin film preparation and changes in the method of polymer solution deposition.

The work on PEG surface morphology acts as the foundation for the remaining studies, which employ the AFM to study biodegradable polymers within aqueous environments. This *in situ* application of the AFM has recorded the changes in surface morphology that occur to poly(sebacic anhydride) (PSA) during surface erosion in alkaline conditions. These studies have visualized the preferential degradation of amorphous regions of sphemlites over the crystalline fibres for solution cast and melt-crystallized samples. It has been found that rapid cooling during the solidification of PSA increases the amount of amorphous material at the surface of samples. However, once this outer layer has bean eroded the underlying material is dominated by crystalline fibres. *In situ* AFM studies have also demonstrated the pH dependence of the rate of PSA surface erosion.

The AFM techniques developed to visualize the evolution of surface changes during PSA erosion have then been employed to investigate the degradation of immiscible blends of PSA and the polyester poly(DL-lactic acid) (PLA). PLA degrades at a slower rate than PSA and therefore, as these blends eroded the surface morphology became dominated by PLA, revealing the phase separation of the material. For solution cast samples on mica substrates it was found that at high PSA content the PSA formed a continuous network around islands of PLA. However, as the relative content of PLA increased the morphology reversed and the PLA formed the network around islands of PSA.

The interest in studying biodegradable polymers is derived from their application in surface eroding dmg delivery systems. Having demonstrated the potential of the AFM to visualize dynamic interfacial changes occurring to these polymeric biomaterials, the *in situ* studies were extended to investigate the release of a model protein dmg from a degrading polymer film. The system under investigation was a poly(ortho ester) film containing particles of bovine serum albumin. The AFM visualized the initiation of dissolution of some protein particles within minutes of the exposure of the sample to a pH 6 environment. Other particles, however, displayed retarded dissolution behaviour and did not appear to dissolve until the sample had bean exposed to the pH 6 environment for over 1 hour. To assist the interpretation of these studies computational methods of calculating changes in volume during polymer

degradation and protein dissolution have been developed on the Genesis II system.

In the final experiments of this thesis, the application of a novel combined atomic force microscopy/surface plasmon resonance instmment is described. This instrument allows the simultaneous acquisition of topographical data by the AFM and kinetic data by the surface plasmon resonance instmment (SPR). The instmment is first applied to a simple poly(ortho ester) system to demonstrate that the changes surface morphology and polymer film thickness can be simultaneously monitored. Then, the PSA/PLA blends were re-analysed. This analysis highlighted the synergistic information obtained by the combined AFM/SPR and revealed new data on the relationship between polymer phase separation and biodegradation kinetics.

Table of Contents

## List of Figures

# List of Tables

# Chapter 1 Introduction

This thesis is directed towards the development of atomic force microscopy as a new surface analytical technique for characterizing polymeric biomaterials. This introductory chapter aims to explain the importance of polymeric biomaterial surfaces and to outline the potential of the atomic force microscope to advance the understanding of these surfaces.

## 1.1 The Use of Polymers as Biomaterials

A biomaterial is a non-viable substance, other than a food or dmg, employed within a therapeutic system to improve the functioning of a patient (1-3). Biomaterials are extensively utilized in a wide range of disease states, as demonstrated by the examples of application shown in Table 1.1. Each application of a biomaterial demands different properties from the employed material. For example, a hip replacement joint must be composed of a material with a high tensile strength to allow transmission of loads from the pelvis to the femur (7), whilst in achieving controlled dmg delivery it may be desirable for a biomaterial to degrade within the body over a short period of time (13). This range of predetermined desirable properties has led to a large number of different types of material being used to engineer biomaterials (17). Increasingly, the use of polymers as biomaterials is dominating many areas of this field (2). This dominance may be attributed to the flexibility of properties of polymeric materials (18). Desirable properties, such as high tensile strength and biodegradability, can be introduced into polymers by changing their chemical stmcture or physical organization. The extended chain stmcture of polymers and the ability to generate branched, cross-linked, co-polymerized and blended polymeric materials ensures that there are an enormous number of potential chemical changes that can be made to polymeric biomaterials (18). In addition, many established fabrication methods exist to convert polymers in biomaterial devices.

| Area of Application | Example of Biomaterial Function | Reference |
|---|---|---|
| Cardiovascular system | Vascular graft<br>Heart Valve<br>Artificial heart | **4**<br>**5**<br>**6** |
| Protheses | Hip replacement<br>Reconstmctive surgery | **7**<br>**8** |
| Skin | Artificial skin graft | **9** |
| Tissue engineering | Guidance of nerve regeneration | **10** |
| Renal function | Kidney dialysis membrane<br>Urinary catheters | **11**<br>**12** |
| Controlled dmg delivery | Biodegradable implants<br>Transdermal patches | **13**<br>**14** |
| Surgical | Sutures | **15** |
| Ophthalmic | Contact and Intraocular Lenses | **16** |

Table 1.1 Examples of the applications of biomaterials.

## 1.2 The Influence of Polymer Surfaces on Biomaterial Function

When a biomaterial is employed within the body, a synthetic surface is exposed to the complex environment of the host and a solid/aqueous interface is created. The behaviour of the synthetic biomaterial surface at this interface, and the surface properties of biomaterials is highlighted by the categorization of the characteristics of biomaterials by D.F. Williams into biofunctionality and biocompatibility (3). The biofunctionality is the purpose for which the biomaterial is applied within the body. For many biomaterials, in particular controlled dmg delivery systems, the biofunctionality is entirely determined by the behaviour of the surface. For example, if we consider a biodegradable polymer implant whose biofunction is to slowly release dmgs within the body as a result of hydrolytic surface erosion of the polymer, this function will be achieved by the hydrolysis of polymer molecules at the polymer/aqueous interface . This hydrolytic activity will be determined by surface properties such as hydrophobicity, which controls water permeation, and presence of chemical groups which are susceptible to hydrolytic attack (13).

Even for those biomaterials whose biofunctionality is not directly dependent on surface properties, the second characteristic, biocompatibility, ensures the importance of the biomaterial surface. Biocompatibility has been defined as the ability of a material to perform with an appropriate host response in a specific application (19). To achieve biocompatibility, a biomaterial must be acceptable to the living system in which it is applied. This acceptability is achieved through the surface properties of the biomaterial initiating appropriate responses from the living system, in particular, the appropriate adsorption of extracellular proteins (20) and adhesion of cells (21). If these processes do not occur, then the synthetic material will be rejected by the living system leading to an inflammatory response. Therefore, if we again consider the functioning of a hip replacement, the biofunctionality is achieved by the bulk properties of the biomaterial generating sufficient tensile strength, however, if the surface properties are not conducive to biocompatibility then the hip replacement will have to be surgically removed and will be unable to achieve its function.

## 1.3 Methods of Surface Analysis of Biomaterials

The importance of surface interactions demands that the surface properties of polymeric biomaterials should be extensively characterized and controlled. In general, the surface properties of a material are very different from the bulk properties, because molecules at a surface are not surrounded by similar species, but are exposed to an interface (22, 23). This interface significantly modifies molecular behaviour and, therefore, can generate molecular orientations and properties which are dissimilar to the bulk material.

The technological importance of surfaces has encouraged the development of a variety of techniques that can measure surface properties (24, 25). These techniques have to be very sensitive to the properties of the surface that they are analyzing and must exclude any signal from the bulk material. In practise this surface sensitivity is difficult to achieve due to small amount of material that is truly at the surface. Despite this constraint there are now a growing number of surface analytical techniques which can be applied to polymeric biomaterials. The information in Table 1.2 summarizes the attributes of a number of these techniques and gives examples of there application in biomaterial science.

Each surface analytical technique has its own advantages and limitations. In the field of surface chemical analysis both XPS and SSIMS possess exceptionally high sensitivities and can generate data on the outermost 10 A of a sample (26-28), however, both require ultrahigh vacuum conditions. For polymeric biomaterials, which are employed within an aqueous environment, performing chemical analysis in an ultrahigh vacuum may be inappropriate, without cryogenic preparation of the sample, due to the potential surface restmcturing which can occur (36). The ATR spectroscopies have the advantage of avoiding sample exposure to ultrahigh vacuum conditions, however, their application in biomaterial analysis is restricted by their relatively high penetration depth which samples chemical data from a region of 1 to 5 μm below the boundary of the sample (25). In the morphological analysis of polymeric biomaterials, the most intensely used microscope, the SEM, is limited by the low electron density and electrical insulating nature of polymers. The practical implications of these characteristics are that many polymer samples must be coated with a thin metallic film or stained with an electron dense

| Surface Information | Technique | Reference |
|---|---|---|
| **Chemistry** | | |
| Elemental analysis | X-ray photoelectron spectroscopy | 26,27 |
| Molecular species | Static secondary ion mass spectrometry (SSIMS) | 27,28 |
| Surface distribution of molecular species | SSIMS imaging | 29 |
| Chemical bond type | Attenuated total internal reflection - infrared spectroscopy (ATR-IR) | 30 |
| Chemical bond type | Photoacoustic infrared spectroscopy (PA-IR) | 31 |
| **Morphology** | | |
| Nano to millimetre resolution | Scanning electron microscopy (SEM) | 32 |
| Nano to millimetre resolution | Confocal microscopy | 33 |
| Nano to micrometre resolution | Photon tunneling microscopy (PTM) | 34 |
| **Energetics** | | |
| Critical surface tension and related surface energy parameters | Contact angle measurement | 35 |

Table 1.2 Examples of the surface analysis of biomaterials.

material before SEM analysis (37). The major limitation of contact angle measurement studies for the determination of the surface energetics of polymers is the very low spatial resolution achieved. For homogeneous one component polymeric biomaterials spatial resolution may unimportant. However, many polymeric biomaterials are complex systems of co-polymers or blends and for such systems, any relevant surface analysis must ensure that the spatial resolution matches the spatial heterogeneity of the chemical and morphology characteristics of the sample.

The limitations of many surface analysis techniques does not prevent them from generating valuable data which has substantially improved the understanding of polymeric biomaterial surface properties. However, as highlighted in a recent review of current issues in biomaterial design by Peppas and Langer (1), there is a need for new surface analysis techniques which can complement the existing techniques, particularly in the area of the behaviour of polymeric surfaces at interfaces within aqueous environments.

Recently, a new family of techniques, called the scanning probe microscopes (SPMs), have been developed which have the potential to advance the study of polymer surfaces. These SPM techniques can provide high resolution images of the topography of surfaces to nanometre resolution and this imaging can be performed under liquid and gas, as well vacuum conditions. In addition, SPM techniques can measure the local mechanical properties of surfaces and the forces of interactions experienced between molecular or colloidal species in close proximity. These attributes have resulted in the SPM techniques making a considerable impact in materials science.

## 1.4 The Scanning Probe Microscopes

The scanning probe microscopes comprise a growing number of interrelated instmments, their common feature is a probe which interrogates the local surface properties as it is scanned over the sample. The most extensively employed SPM techniques are scanning tunneling microscopy and atomic force microscopy which measure local changes in conductivity and force, respectively, to generate three-dimensional representations of sample surface topography.

### 1.4.1 Scanning Tunneling Microscopy

The scanning tunneling microscope (STM) was the first SPM to be described (38) and the importance of the instmment to surface science was demonstrated by the presentation of the 1986 Nobel Prize in Physics to the inventors within 5 years of the first published description. The STM obtains images of the surface topography of samples by monitoring the tunneling current flowing between a sharp metallic probe and the sample surface. A schematic representation of a STM instmment is shown in Figure 1.1. The sharp metallic probe is mounted on a piezoscanner tube which rasters it across a surface with a probe/surface separation distance of less than 1 nm. As the probe moves over the surface, the magnitude of the tunneling current is determined by the probe/surface separation, with a 1Å change in the separation producing an order of magnitude change in the tunneling current. Therefore, if the probe scans over a raised area of the surface, the tunneling current will increase. To compensate for this increase, the piezoscanner tube moves the probe up, hence increasing the probe/sample separation and returning the timneling current to its original value. By plotting the lateral position of the STM probe against the piezoscanner-controUed height of the probe, a three-dimensional representation of the sample surface is obtained.

The sensitivity of the relationship between probe/sample separation and tunneling current, and the precision movement of the STM probe by the piezoscanner tube is such that the instmment can achieve atomic resolution (39). However, the apphcation of the STM in the biomedical and polymer science has been restricted by the requirement for the sample surface to be conductive. This requirement has not been as restrictive as might, at first, be perceived because it has been found that thin films of isolated insulating molecules can be imaged with the STM if they are themselves deposited on a conductive substrate (40, 41).

### 1.4.2 Atomic Force Microscopy

The atomic force microscope (AFM) was first described in 1986 (42) and is a direct descendant of the STM. The stimulus for its design was the desire to use SPM techniques on totally insulating materials, and hence open the possibility

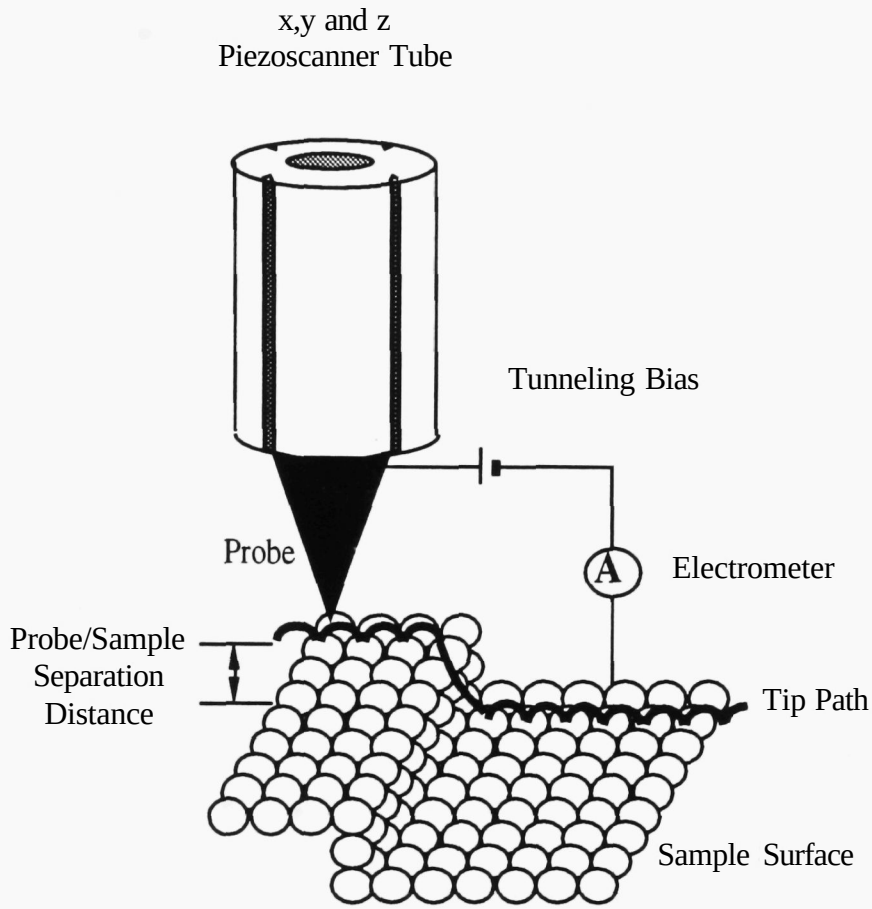


Figure 1.1 A schematic representation of the STM (drawn by C.J. Roberts).

of using these instmments on a wide range of biological and polymeric samples. In terms of analyzing polymeric materials, the AFM has three major attributes, which may explain the influence that the instmment is having on surface analysis and microscopy. These attributes are:

- *The AFM can achieve very high resolution of sample features in three dimensions.*

For example the AFM can resolve individual polymer molecules, either as part of a crystal surface (43) or as an isolated entity on a substrate (44).

- *The AFM can obtain sample topographies without surface treatment or coating.*

For electron microscopy techniques, the low electron density and insulating nature of most polymers dictates that samples must be treated prior to image acquisition. Commonly, this necessitates the exposure of the polymeric sample to a vacuum environment or a staining procedure. With the AFM, the sample can be imaged in its natural state, hence the potential incidence of sample preparation induced artifacts is reduced.

- *The AFM can acquire images within a liquid environment.*

Surfaces can be analyzed when exposed to an aqueous or other liquid environment. Hence the AFM provides a method of imaging surfaces at solid/water interfaces. In addition, because the surface is untreated, any surface changes resulting from behaviour at this interface can be visualized. This ability has enabled dynamic surface events, such as the aggregation of fibrin, to be recorded in real-time (45).

#### 1.4.2.1 AFM Design and Modes of Operation

The basic configuration of an AFM is shown schematically in Figure 1.2. The AFM creates three-dimensional representations of the sample surface by monitoring the forces of interaction experienced between the sample and a sharp proba, as the proba scans over the surface. The forces of interaction may be repulsive (Bom repulsion) or attractive (van der Waals) and this gives rise to the different modes of operation of the AFM. Historically, the first AFM instmments monitored repulsive forces and the mode of operation was termed

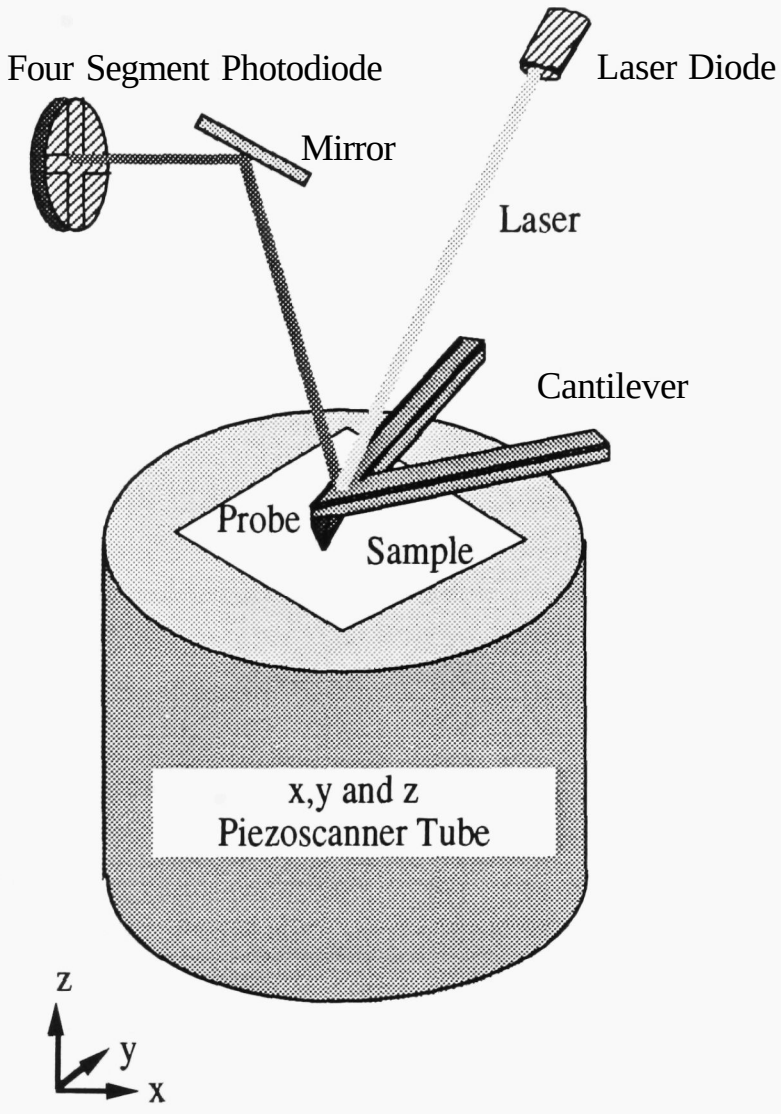


Figure 1.2 A schematic representation of the AFM.

contact mode. This mode is still the most frequently used and will form the basis of this discussion.

The central component of an AFM is the microfabricatad probe and cantilever (46). The probe commonly consists of a silicon nitride pyramid with a very sharp tip (the terminal radius of the tip is approximately 20 nm). This probe is grown on the end of a flexible silicon cantilever. A typical AFM probe and cantilever is shown in the SEM micrographs in Figure 1.3. The cantilever acts as a soft spring of known spring constant which obeys Hookes Law:

$F = -kz$ *where F is the force acting on the cantilever*
*k is the cantilever spring constant*
*z is the vertical displacement of the end of the cantilever.*

Therefore, it is possible to measure the forces acting on the AFM probe by monitoring the vertical displacement of the cantilever (z). A number of detection systems have been utilized to measure z. The simplest detection system, and the most commonly used, measures the angle of reflection of a laser from the upper side of the cantilever (see Figure 1.2) (47). Alternative detection systems include the utilization of electron tunneling (48), interferometry (49), capacitance (50) and piezoresistive strain (51).

In most AFM designs, the piezoscanner tube is positioned beneath the sample and hence, scanning is achieved by moving the sample relative to the stationary probe. Before obtaining an image it is necessary to set-up the desired repulsive force between the probe and the surface. This is achieved by raising the sample, using the piezoscanner tube, until the surface of the sample just contacts with the tip of the AFM probe. This contact creates a repulsive force due to the overlap of the outer electron shells of the sample surface and the probe. By precisely controlling the height of the sample relative to the probe, it is possible to maintain repulsive forces lower than 1 nN. This repulsive force is recorded by the deflection of the cantilever which, in turn, is monitored by the angle of reflection of the laser as measured by the four quadrant photodiode (see Figure 1.2).

The method of obtaining an image of the sample surface is analogous to

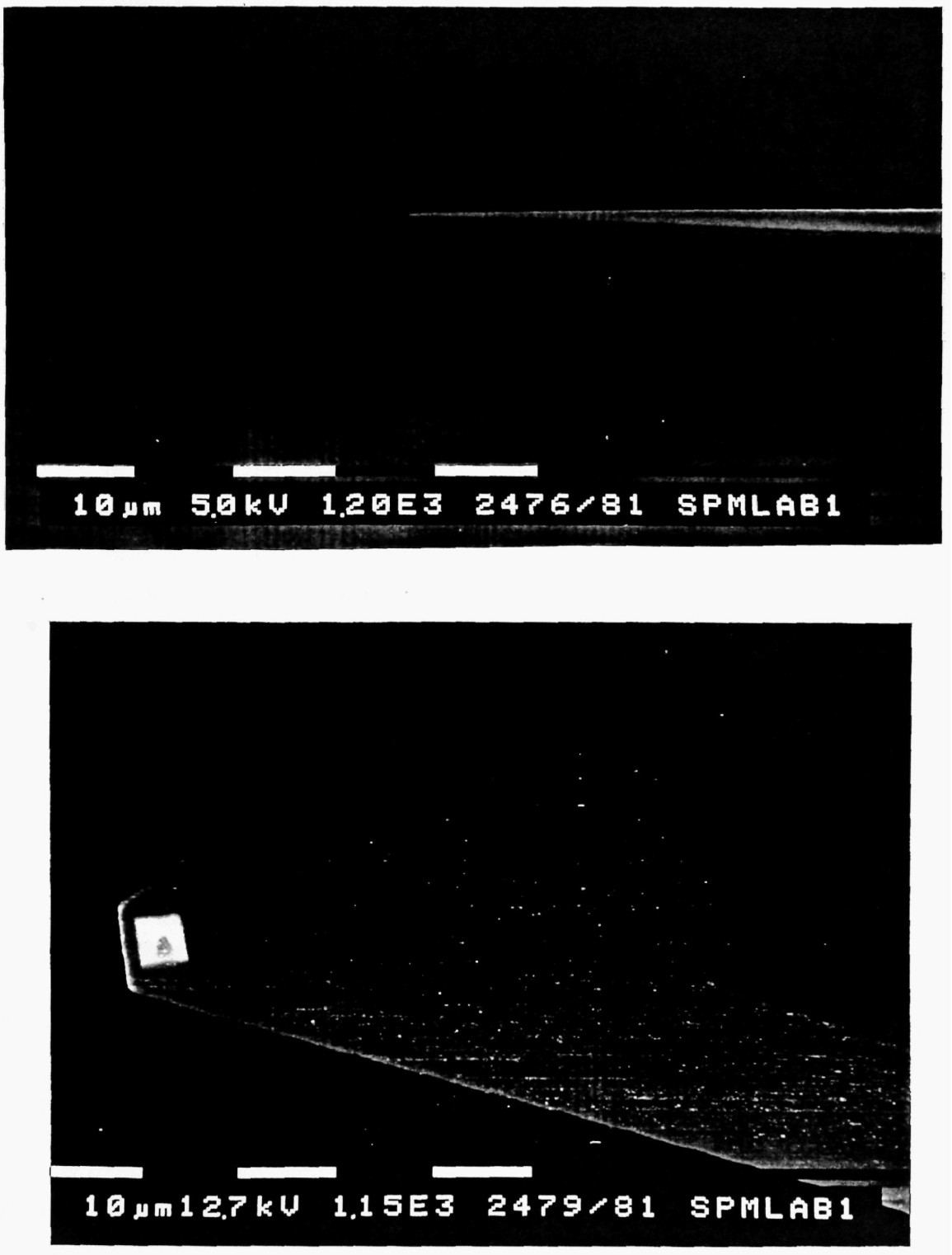


Figure 1.3 - Electi-on micrographs of an AFM probe

the method used by the STM. If the AFM probe scans over a raised area, the repulsive force increases because the electron orbitals are forced to overlap further. A feedback loop from the photodiode to the piezoscanner tube then acts to lower the sample and hence, restore the preset repulsive force. Three-dimensional images of constant force are obtained by plotting the sample height against the lateral probe position.

One limitation in the operation of the AFM in contact mode, is the potential for the probe to damage the surface of soft samples during scanning (52). To overcome this problem other modes of operation have been designed which avoid the continual close contact of the probe and surface. These modes of operation are displayed schematically in Figure 1.4. In non-contact attractive mode (53), the AFM cantilever is forced to vibrate close to its resonant frequency a short distance above the sample surface and the forces measured are attractive (mainly van der Waals) (54). Recently, a new method of operation has been introduced in which the AFM cantilever is vibrated as in non-contact mode, but at the lowest point in the modulation cycle, the probe tip touches the sample surface. This mode of operation has been termed 'tapping mode' and combines the high resolution capability of contact mode imaging with the non-destmctive nature of non-contact mode imaging (55).

The AFM is not limited to obtaining topographical data from a sample surface, in addition the instmment can generate data on the frictional and mechanical properties whilst simultaneously visualizing the surface topography. The measurement of frictional properties is utilized in lateral force microscopy (LFM) (see Figure 1.5), in which the twisting of the AFM cantilever is monitored as it scans across friction boundaries (56). Mechanical properties such as elasticity and adhesion can also be recorded by monitoring the relationship between probe/sample separation and interaction force (54).

The STM and AFM account for a large majority of investigations performed with the scanning probe microscopes. However, there is a rapid pace of development of new microscopes, which arc based on these instmments and measure alternative surface properties (57). Examples of these new instruments include; the scanning near-field optical microscope (NSOM) which combines the high resolution of the SPM techniques with the contrast mechanisms of

Contact Mode

Probe constantly in contact with sample surface

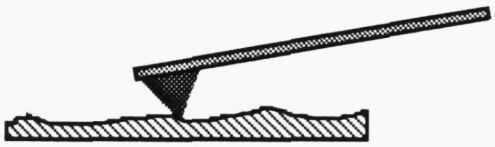

Non-Contact Mode

Cantilever modulated at resonant frequency above surface

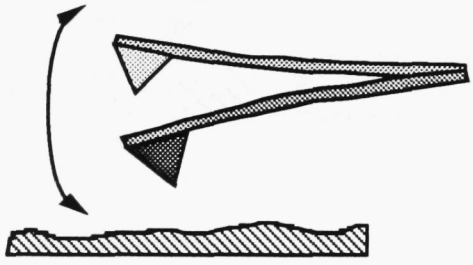

"Tapping" Mode

Cantilever modulated at resonant frequency with probe touching surface at low point

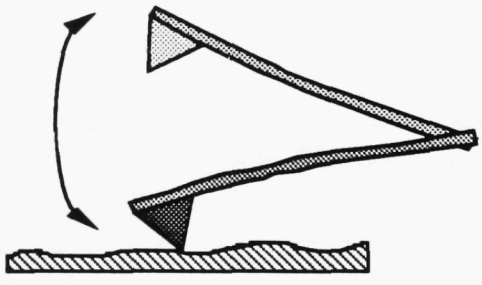

Figure 1.4 The three topographical imaging modes of the AFM.

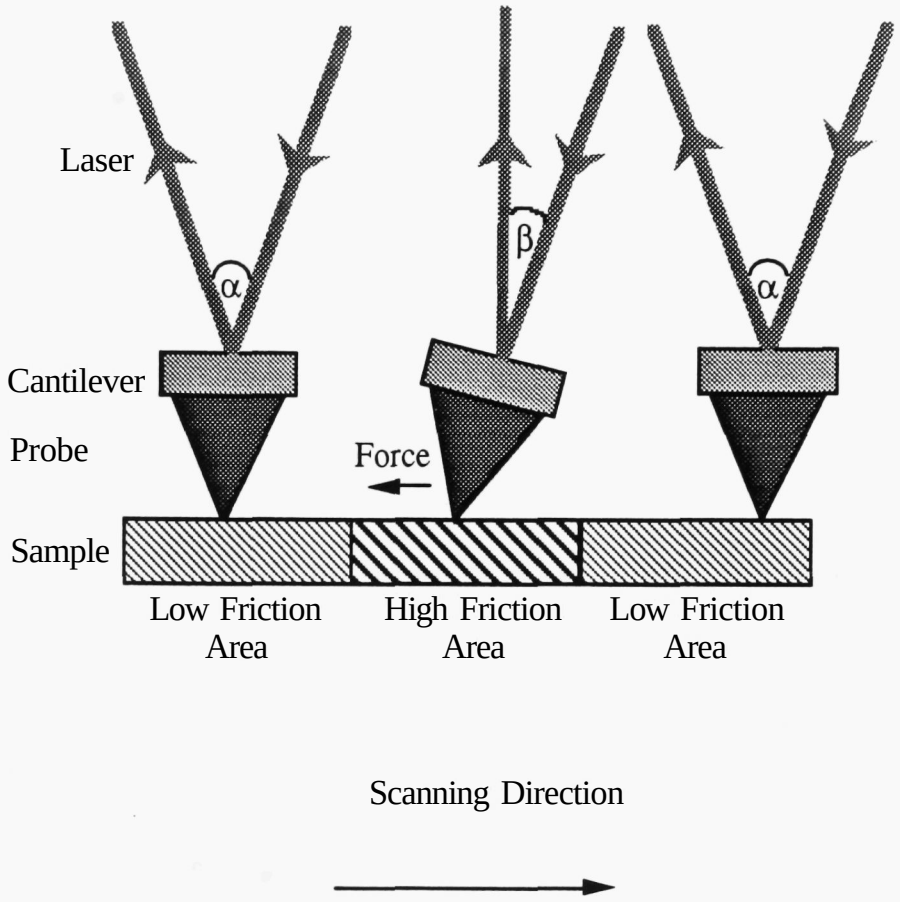


Figure 1.5 Lateral force microscopy detecting changes in the frictional properties of a surface. On a low friction area, the lateral position of the AFM cantilever is normal and the angle of reflection of the laser from the upper side of the cantilever is $\alpha^{\circ}$. When the AFM probe scans across onto a high friction area the retardation of movement of the probe causes a lateral twisting of the cantilever and hence, the angle of reflection of the laser is decreased to $\beta^{\circ}$.

conventional light microscopy (58), scanning thermal microscopy which monitors local changes in temperature over surfaces (57), and AFM detection of magnetic resonance (59).

## 1.5 The Impact of SPM in Materials Science

The SPM technologies have provided researchers with a new and powerful method of resolving the local surface properties of materials. The value of such techniques can be judged by the rapid and extensive impact of the instmments in materials analysis in a relatively short period of time.

STM is providing new insights into the atomic and molecular stmcture of the surfaces of metals (60), semi-conductors (61) and organic layers (62). Successes in these areas include the imaging of the 7x7 reconstmction of the Si(l 11) surface (63) and the imaging of arrays of individual benzene molecules (62).

In the analysis of insulating materials, AFM has opened new possibilities in surface imaging and this has had a major impact in the study of biomolecular stmcture (64) and the forces of binding between individual ligand receptor pairs (65, 66), cell membrane organization (67), crystal growth (68), Langmuir-Blodgett film stmcture (69), and self-assembled monolayers (70).

Given the range of SPM applications in materials science it is not surprising that the instmments have contributed to the analysis of polymeric materials. The next section of this introduction reviews the areas in which the AFM has advanced our understanding of polymer surface morphology.

## 1.6 The Utilization of the AFM in the Analysis of Polymer Surface Morphology

### 1.6.1 Early Studies

The first accounts of the use of the AFM to study polymers came in 1988 when

Marti *et al* described experiments during which parallel rows of polymer molecules with spacings of approximately 0.5 nm were resolved (71). Their sample consisted of polymerized monolayers of n-(2-aminoethyl)-10,12-tricosadiynamide which forms rows of tightiy packed hydrocarbon tails along the direction of polymerization. The authors were careful to eliminate the possibility of attributing molecular structure to artifactual data through a comparison of the topographies of the polymer sample and the glass slide substrate. In addition, by varying the rate of scanning and the orientation of the sample it was possible to determine that the 0.5 nm wide cormgations were created by the molecular features and not instrumental noise.

Also in 1988, Albrecht *et al* described the imaging of ultrathin polymeric film prepared by a Langmuir-Blodgett technique (72) and Drake *et al* described the first example of the imaging of a poly(amino acid) film within an aqueous environment (45). Since the publication of these early studies there has been a rapid rate of growth of polymer analysis by AFM. Much attention still concentrates on achieving molecular resolution, however, the scope of analysis has broadened to incorporate the study of co-polymers, polymer blends, fabricated and treated surfaces and the study of the mechanical properties of polymers.

### 1.6.2 Molecular Resolution

To achieve molecular resolution with the AFM there are two fundamental sample requirements which must be realized. The first requirement is that the area of the sample to be imaged must be very flat on the nanometre length scale. This flamess is necessary to ensure that only the apex atoms of the probe contact with the sample. Molecular resolution cannot be achieved on rough samples because the resolution limit of the AFM becomes dependent on the terminal radius of the AFM probe (73) which is currently at least 5 nm (74). The second requirement is that the molecular stmcture of the sample is rigid enough to withstand the scanning motion of the AFM probe. In the first study of Marti *et al* the sample was chosen due to its high stmctural integrity. Mora recent developments in AFM technology have facilitated the study of many other sample types because the force exerted by the AFM probe have been decreased (54) and the cantilever detection sensitivity has improved (47). Despite the

developments in AFM probe design and force minimization strategies the range of samples which can be molecularly resolved is still limited to crystals, mechanically oriented thin films and epitaxially-grown films.

In the study of polymer crystals, the AFM is being applied to study the morphology of the fold surface. Since Keller proposed the chain-fold modal of polymer crystallization (75) there has been interest in determining the conformation and arrangement of polymer chains at fold surfaces and in particular in the relative importance of regular adjacent re-entry versus the switchboard model (76). Initial studies in the imaging of fold surfaces used alkane samples (77). Although not polymeric materials, the alkanes acted as well defined models for polyethylene and the AFM images supported an adjacent reentry model of the chain folding. Patil and Reneker have described the AFM imaging of molecular folds in polyethylene single crystals and measured fold spacings consistent with the orthorhombic and monoclinic unit cell (78). This paper also demonstrated the difficulty of molecular resolution studies because for many of the polyethylene samples low quality images were obtained when small scans were recorded. This low quality has been attributed to either multiple contact between the AFM probe and the sample or the presence of amorphous polymeric material at the crystal surface. Sykes *et al* have attempted to improve the AFM imaging of fold stmcture by etching polymer crystals prior to AFM analysis (79). In their studies, they imaged the surfaces of poly($\beta$)hydroxybutyrate and hydroxybutyrate oligomer crystals. The oligomer crystals are known to possess a tightiy folded structure and the lack of amorphous material enabled the AFM to image features on the crystallographic *b* axis which were separated by only 0.7 nm. These features were attributed to either chain endings or folded stmctures. The poly($\beta$)hydroxybutyrate crystals ware estimated to be covered with an 0.6 nm amorphous layer. Attempts to etch away this layer were performed by partially degrading the crystals in a methylamine aqueous solution and encouraging the sample retained enough rigidity to be imaged by AFM after this treatment, although further studies are required to ascertain if chain folds can be resolved.

The AFM has also been applied to study extended-chain crystals. Annis *et al* analyzed fracture surfaces of polyethylene extended-chain crystals (80). Having identified flat regions on the fracture surface they performed high

resolution imaging to visualize atomic scale features but these features could not be assigned to expected polymer chain dimensions. Snétivy *et al* have described the AFM imaging of polyoxymethylene extended-chain crystals (81). They achieved molecular resolution on the surfaces of microfibrillar features and the AFM recorded dimensions of the crystal lattice were in excellent agreement with the X-ray crystallography data. In addition, the authors tried to address the problem of the image-contrast mechanism which can generate molecularly resolved images. They proposed that the well-resolved sections of their images corresponded to areas of the sample where the methylene groups were exposed.

The mechanical-orientation of polymer films is employed to produce commercial materials with exceptionally high mechanical strength and modulus (82). These desirable mechanical properties are achieved through the uniaxial orientation of polymer chains and tiie commercial optimization of these materials can be assisted by the use of the AFM to image the effect of fabrication on the polymer morphology. Magonov *et al* have analyzed cold-extruded (83) and gel-drawn (84) samples of polyethylene. For the gel-drawn materials they observed four levels of morphological organization with crystalline polyethylene molecules packing to form nanofibrils which, in tum, form microfibrils which bundle together to produce micron scale fibres. A number of AFM studies have analyzed the molecular stmcture of poly(tetrafluoroethylene) oriented films (85,86). These films can be generated by simply mbbing a bar of the polymer against a glass support. Commercially, the molecular organization of these films is of interest because a secondary material can be oriented by deposition onto the poly(tetrafluoroethylene). The poly(tetrafluoroethylene) molecules act as a template and the AFM has successfully imaged the organization of the polymer at the molecular and fibrillar length scale.

Other examples of the molecular resolution of mechanically oriented polymers include the studies on isotactic polypropylene (87, 88), isotactic polystyrene (89), and poly(butene-1) (90).

A final area in which the AFM has provided new insights into the molecular stmcture of polymers is in the epitaxial growth of thin films. Stocker *et al* have employed the AFM to ùnage isotactic (91) polypropylene epitaxially grown on organic surfaces. Their studies have been correlated with electron diffraction and electron microscopy work. In the analysis of isotactic

polypropylene (91) the authors highlighted tiiat only the AFM could determine the molecular organization of the polymer in contact with the organic substrate.

### 1.6.3 Sub-micron Film Morphology

In many areas of polymer technology, imaging the molecular stmcture of materials is not as important as understanding the way in which the polymer molecules organize into larger-scale features. For example, the mechanical properties of semi-crystalline polymer films are often determined by the stmcture and distribution of spharulitas. Whan the idea of the AFM was originally conceived the major stimulus was the desire to image atomic features on insulator surfaces. However, there has been a realization in materials science, including polymer technology, that the instmment is well suited to imaging supramolecular organization.

The work of Goh *et al* provides a good example of the benefits of using the AFM to image sub-micron film morphology (93). They have studied the surface stmcture of cast poly(butyl methacrylate) latex films and then monitored the changes in film morphology on annealing. Casting aqueous solutions of the latex particles onto a freshly cleaved mica surface resulted in the formation of face-centred cubic stmctures which were stable below the glass transition temperature of the polymer. When the films were heated to a temperature above the glass transition, polymer diffusion caused a rearrangement of the particle surface stmcture which was observed by the AFM as a decrease in the vertical height of the particle. The AFM provided two distinct benefits in these studies. Firstly, because the samples required no surface coating prior to image acquisition, re-examination of the morphology after a number of annealing steps was possible. Secondly, the polymer diffusion and particle surface rearrangement can only be appreciated through a three-dimensional representation of the fihn.

The high vertical resolution of the AFM has bean utilized by Stange *et al* to characterize very thin films of polystyrene spin-coated onto silicon surfaces (94). As the concentration of polystyrene in the spin cast solution was increased the film morphology changed from isolated particles to Voronoi tessellation like networks to continuous films. The maximum vertical height differences between

the polymer film and substrate were less then 5 nm. The vertical resolution capability of the AFM has also been used by Snétivy and Vancso to image screw dislocations in poly(ethyIene oxide) and to characterize the disintegration of the crystal lamellae (95). Comparison of the height of lamellae features before and after disintegration indicated a thickening caused by refolding of the polymer chains.

In section 1.4.2.1 new modes of operation of the AFM were discussed. The group of Magonov have investigated the application of lateral force and tapping modes on the sub-micron resolution imaging of polyethylene tapes (96). They noted that in comparison to contact mode imaging, both lateral force and tapping modes generated improved resolution of nanofibrillar stmctures. Nisman *et al* have also used LFM to study lamellar crystals of poly(oxymathylane) (97). They observed a direction-dependent friction as the AFM probe scanned across two different segments of the crystal surface. This frictional change can be attributed to the alignment of chain folds within each segment.

### 1.6.4 Co-polymers and Polymer Blends

The need to characterize surface organization is particularly apparent in complex polymeric systems such as co-polymers or polymer blends (98). These types of materials offer the advantage of combining the mechanical and functional properties of two or more polymers into one fabricated material. However, this combination is considerably complicated by surface properties which can induce major morphological changes, such as surface enrichment of one component or phase separation. The morphological changes are often not predictable from the bulk behaviour of the polymers, ie. the changes are induced by the presence of a solid/liquid or solid/gas interface (99). The AFM has proved to be very successful in this area of materials characterization.

In the study of block co-polymers the AFM has been used to identify surface specific enrichment and separation processes. Collin *et al* imaged the free surface of a poly(styrene-*b*-*n*-butyl methacrylate) diblock copolymer and were able to record the time dependent evolution studies of island stmctures during annealing (100). Annis *et al* have recorded the surface enrichment of the

butadiene component of a block co-polymer of styrene and butadiene and recorded the effect of molecular mass on the lamellar surface morphology (101).

Nick et *al* have introduced a method of determining which constituent of a block co-polymer film is responsible for particular surface morphological characteristics (102). They developed this method on diblock co-polymers of poly(styrene-*b*-methyl-methacrylate) films spun cast on mica. To assign the topographical features of each block they selectively degraded the methyl methacrylate block using electron beam radiation. Using this technique of contrast enhancement it was shown that the methyl methacrylate blocks preferential resided in contact with the mica substrate with the styrene blocks forming prominent features at the polymer/air interface.

Motomatsu *et al* were able to identify polystyrene and poIy(methyl methacrylate) domains in immiscible blend fdms and co-polymer systems using the AFM, using both conventional contact mode imaging and LFM (103). The image contrast in the LFM images was derived from differences in the co-efficients of friction of the two polymers and this allowed the different phases to be identified in addition to topographical characterization.

Polymer blend systems have also been studied by Saraf (104). In this study a blend of two polyimide precursor polymers were mixed in *N*-methylpyrrolidonone (NMP) solvent and spun cast onto single-crystal silicon wafers. On baking, the spun cast film phase separated during which the acidic precursor polymers complexed with solvent molecules to form nanoscopic hill stmctures above the basic precursor. Atomic force microscopy enabled this phase separation to be visualized and led to the characterization of the effect of blend film formation on the phase morphology.

### 1.6.5 Treated and Fabricated Polymers

Many of the above examples of the imaging of polymers have used model sample preparation methods to produce thin films which are suited to AFM analysis. In addition to these studies, a number of research groups have used the AFM to characterize the effect of secondary processing or fabrication methods on polymer surface morphology.

Corona discharge treatment is a secondary process used to improve the adhesive and wettability properties of polymers. Ideally, the process should induce polymer chain cross-linking and oxidation. However, morphological changes generated by the treatment, in particular the roughenimg of the polymer surface, can decrease the effectiveness of corona discharge. The AFM has been employed to assess the surface roughening of polymer films during corona discharge ti"eatment and the high vertical contrast of the images generated has given a new insight into the inducement of morphological changes. Ovemey *et al* have studied treated polypropylene films using simultaneous AFM and LFM (105). AFM images recorded the presence of 'dropletlika protmsions' on the polymer surface after corona treatment and the dimensions of the protmsions were found to be proportional to the corona dose. LFM images indicated that the AFM probe experienced high frictional resistance as it scanned over the protmsions and this was attributed to a change in the chemical composition of the protmsions compared to the bulk materials. Ryan and Badyal studied the surface texturing of poly(tetrafluoroethylene) films on corona treatment in the presence of a variety of different elements (106). They found that oxygen treatment generated the highest degree of surface roughening, whilst noble gas plasma caused the formation of fibrillar textures.

Another area of secondary processing that has utilized the AFM is the generation of aligned polymer stmctures used in the production of liquid crystal material. Zhu *et al* used the AFM to observe the alignment of polyimide films on mbbing (107). The images showed the alignment of aggregates of the polymer, but not the alignment of individual molecules and therefore, have provided an improved understanding of the mechanism of alignment. With similar applications in mind, Hirako and Sendova used the AFM to image the laser-induced generation of periodic structure on a variety of polymer films (108).

As the use of the AFM to study polymer surface morphology becomes more widespread the instmment is being accepted as a tool for studying fully fabricated polymeric materials. The morphology of core shell particles of poly(butyl acrylate) (PBA) and PMMA has been successfully imaged by Sommer *et al* (109). These AFM studies clearly resolved the tiiree-dimensional stmcture of these particles, showing that the surface possessed a "raspberry-like" stmcture. This work also clearly demonstrated the advantages of using tapping mode imaging over conventional contact mode. In contact mode the

frictional effects of scanning the probe over the particles resulted in a considerable deterioration in the image resolution. This deterioration was cause by the penetration of the AFM probe into tiie soft PBA core and by lateral particle movement.

The surface morphologies of contact lenses fabricated by different methods have been compared using the AFM by Baguet *et al* (110). This paper demonstrated that the AFM could image polymeric materials in a hydrated form. The authors found that a molden fabrication procedure produced smoother surface morphologies than lathe-cut fabrication which, in tum, indicated that the molden lenses should spoil less during use.

The AFM has also proved valuable in determining the three-dimensional stmcture of polyvinylidene fluoride microfiltration membranes (111). In this work by Fritzsche *et al,* the AFM visualized a nodular stmcture for the polymer at the surface of the membrane and the AFM data allowed the dimensions of pores to be measured.

### 1.6.6 Inducing Surface Morphology Changes

A fascinating feature of the AFM is that it can be used to modify the surface morphology of certain polymer samples. This modification is made possible by the close relationship between the AFM proba and sample surface during image acquisition. Under certain scanning conditions, namely high imaging forces and slow scan rates, the AFM probe can induce plastic changes in the organization of polymer films. This mode of operation of the AFM has two promising applications in polymer science. Firstly, by monitoring the response of the polymer to the probe it is possible to characterize the elastic/plastic properties of the sample, and secondly, inducing morphological changes promises to generate new material properties for commercial exploitation.

The first report of the modification of a polymer surface by an AFM probe was published by Leung and Goh (52). In this study the surface of a polystyrene thin film was modified. Initially, the AFM probe was held stationary a few nanometres above the polymer surface and a lump of polymer

grew under the probe. The authors attributed this time-dependent growth to the probe pulling polystyrene molecules out of the thin film. When the AFM was scanned across the surface, a regular rippled surface texture was developed.

Meyers *et al* have similarly modified the surfaces of polystyrene films (112) and have used their results to explore the elastic/glassy behaviour of the polymer at different molecular weights. At molecular weights of less than 24k, polymer surface abrasion occurred to the polymer film. As the molecular weight was increased above 24k the AFM probe caused an oriented surface pattem to be generated. The authors speculated that at molecular weights above the entanglement molecular weight, the AFM probe acted to pull surface polystyrene molecules away from the bulk causing a partial disentanglement

The oriented patterns in polystyrene mn perpendicular to the direction of AFM probe scanning. Another method of inducing morphological changes is to physically scratch the polymer film and hence produce groove features in the direction of scanning. This approach has been employed to create features in polyacetylene films enabling nanolithography to be performed (113). Riietschi *et al* have employed a similar method to produce liquid crystal waveguides in the surface of nylon films (114).

## 1.7 Applying Atomic Force Microscopy to Polymeric Biomaterial Surface Analysis

The above examples of the utilization of the AFM to image polymer surfaces stress the advances that has been made in the field and highlight the progression of studies from model films to fully fabricated polymer systems. It is apparent that the AFM has much to offer to the surface analysis of polymeric biomaterials, but at the start of this Ph.D. project in 1992, no AFM studies had been specifically devoted to biomaterial applications. The work described in this thesis has aimed to realize some of the potential, particularly in the area of polymer biodegradation. This area is of central importance to polymeric biomaterial research because for many applications it is vital that the polymer be broken down by the body to avoid long-term toxicity problems. Additionally, in controlled dmg delivery applications of biomaterials, biodegradation is the

utilized as a mechanism of achieving dmg release within the patient.

In the next chapter, Chapter 2, the instmmentation used in all studies is described in detail. This chapter will act a reference for the experimental work described subsequentiy.

Chapter 3 describes the initial studies performed with the AFM on polymeric biomaterials. This work aimed to develop sample preparation and imaging methods suitable for these materials. The studies concentrated on the semi-crystalline polymer poly(ethylene oxide) (PEO) and the effect of sample preparation parameters involved in solution casting on surface morphology are explored.

Having determined suitable methods of imaging and preparing polymeric samples, the work described in Chapter 4 illustrates the benefits of visualizing polymer surface morphology under aqueous conditions. The main aim of this chapter was to visualize changes occurring to the surface morphology of biodegradable polymers during surface erosion. The first biodegradable system analyzed was poly(sebacic anhydride) and it has been demonstrated that the AFM can visualize the preferential degradation of amorphous material over crystalline material for both solution cast and melt crystallized films of this semi-crystalline polymer. Then, the influence of the phase morphology of an immiscible blend of two biodegradable polymers is studied using the *in situ* AFM technique.

In Chapter 5, the work progresses to visualize the release of a protein dmg from a poly(ortho ester) film. This Chapter also introduces the concept of measuring volume changes occurring to AFM data during a dynamic interfacial process.

In the final experimental chapter, Chapter 6, the application of a new combined AFM/surface plasmon resonance instmment in the analysis of polymer degradation is described. This new instmment has bean designed and constructed by researchers at the Laboratory of Biophysics and Surface Analysis and enables the simultaneous acquisition of kinetic and topographic data during dynamic surface events. The instrument is applied in the analysis of poly(ortho ester) and polymer blend systems and provides new insights into the

role of polymer surface morphology in determining the kinetics and mechanism of surface erosion.

# Chapter 2 Instrumentation

## 2.1 Atomic Force Microscopy

Two types of AFM have been used in the studies described in this thesis; the Topomatiix Explorer (Topometrix U.K., Saffron Walden) and the Rasterscope 3000 (Danish Microengineering, Herlev DK2730, Denmark). The majority of work has used the Topometiix Explorer and therefore, the AFM description will concentrate on this instmment. Variations in the design and operation of the Rasterscope 3000 will be described in section 2.1.5. All imaging has been performed in contact mode.

### 2.1.1 Instrument Design

The Explorer is a free-standing AFM instmment in which the piezoscanner assembly is sited above the AFM probe. The AFM can be employed with a 3 μm or 150 μm lateral range scanner. The schematic diagram in Figure 2.1 shows a cross-sectional representation of the Explorer as set up for the 150 μm scanner. Lateral movement of the AFM probe is generated by the x and y piezoceramics positioned towards the top of the scanning tower. The scanning tower design incorporates the laser, mirror assembly and photodetector and hence, all three maintain the same relative position throughout the scanning motion. Vertical movement of the AFM probe during image acquisition is produced by the z-piezoceramic sited at the base of the scanning tower. Coarse vertical movement, required to bring the AFM probe towards the sample surface prior to image acquisition, is achieved using three height adjusting screws. One of the three screws is controlled by a stepper motor, which can be controlled by the operator via the instmment software, or by the AFM electronic control unit. The stepper motor controlled screw is utilized for fine approaching of the AFM probe to achieve contact with the sample surface.

For higher resolution imaging, the 3 μm tube scanner is employed. A schematic representation of a tube scanner is shown in Figure 2.2. This scanner design consists of a hollow tube of piezoceramic. The outside and inside of the

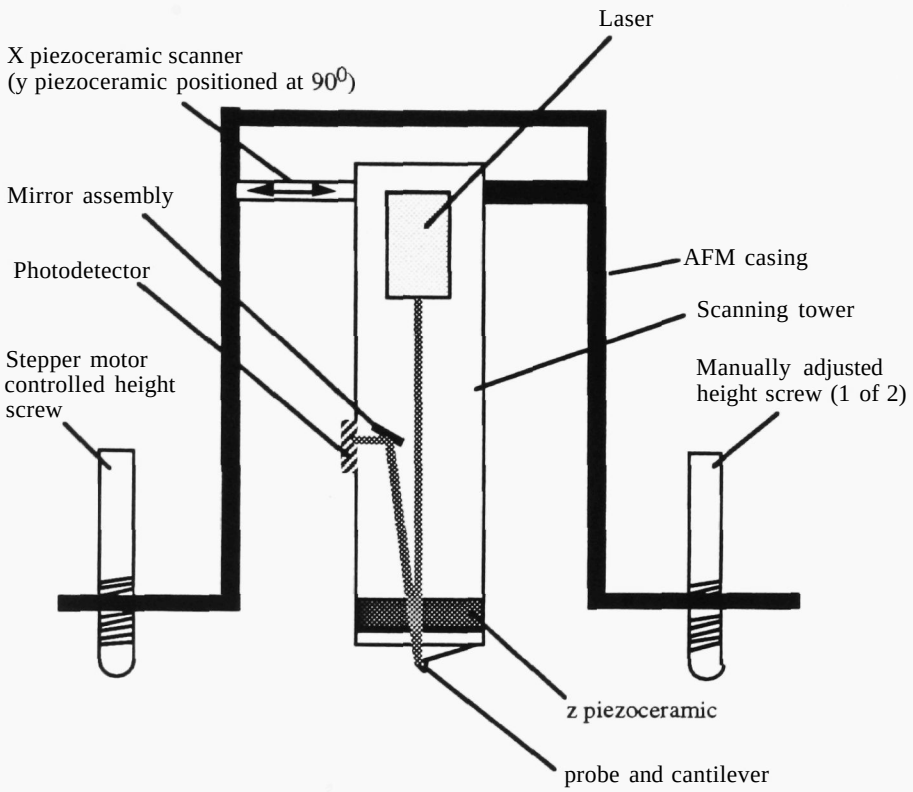


Figure 2.1 Cross-sectional schematic of the Explorer AFM.

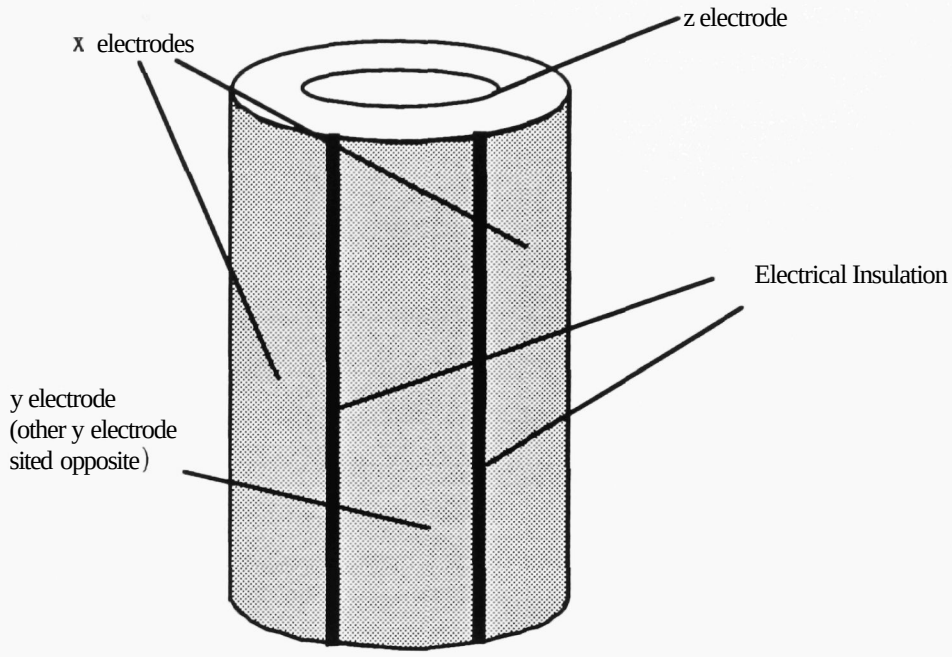


Figure 2.2 Schematic diagram of a tube scanner.

tube are coated with a thin layer of metallic material to generate electrodes. The outer surface electrode is further divided into four segments. Lateral movement is produced by applying a voltage across opposite outer electrodes and vertical movement is achieved by applying a voltage between the inside and outside of the tube (115). For operation of the Explorer with the tube scanner, the z piezoceramic unit used for the 150 μm scanner is removed and replaced with the tube scanner and the scanning tower is held stationary by a locking screw.

### 2.1.2 AFM Probes and Cantilevers

Imaging was performed with microfabricated silicon nitride probes on triangular cantilevers (46) (the complete unit will be termed a probe unit). Two suppliers of probe units were used in these studies; Topometrix Corporation Inc. (Santa Clara, USA) and Park Scientific Instruments (Sunnyvale, USA). The Topometrix probe units are pre-mounted onto the metallic holders which can be fixed to the scanning tower as purchased. The Park Scientific probe units are supplied as a wafer from which individual probe units can be separated. Once separated the probe units are then attached to the metallic holders with an epoxy resin adhesive.

The diagram in Figure 2.3 shows a schematic representation of a typical probe unit A number of important design features can be identified. The overall stmcture of the cantilevers is designed to maximize its resonant frequency, however, for many imaging applications of the probe unit the cantilever spring constant should be minimized. The minimization of spring constant can be achieved by producing cantilevers which are soft, thin and long but this must be balanced against the need for a high resonance frequency which dictates that the cantilevers be very light (54). The spring constants, lengths and thicknesses of the probe units used in this project are listed in Table 2.1. For all data displayed in the experimental chapters the probe unit type used was B,C or H unless otherwise stated. The triangular shape of the cantilever is designed to minimize the influence of lateral forces on the reflected angle of the AFM laser (54).

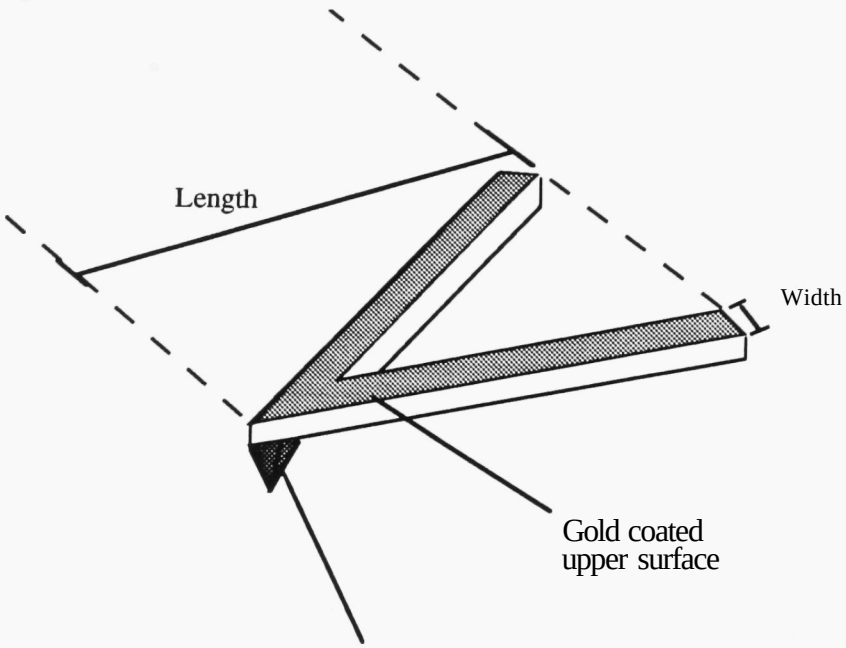


Figure 2.3 Schematic diagram of a probe unit.

Park Scientific Probe Units

| Cantilever Type | Length (μm) | Width (μm) | Spring Constant (N/m) |
|---|---|---|---|
| A | 320 | 22 | 0.01 |
| B | 220 | 22 | 0.03 |
| C | 180 | 18 | 0.05 |
| D | 140 | 18 | 0.1 |
| E | 85 | 18 | 0.5 |
| F | 200 | 18 | 0.032 |
| G | 200 | 36 | 0.064 |

Topometrix Inc. Probe Units

| Cantilever Type | Length (μm) | Width (μm) | Spring Constant (N/m) |
|---|---|---|---|
| H | 200 | 18 | 0.032 |
| I | 200 | 36 | 0.064 |

Table 2.1 Properties of Park Scientific and Topometrix cantilevers. All cantilevers have a thickness of 0.6 μm.

### 2.1.3 Image Acquisition

The first step in acquiring an AFM image of a sample surface is to direct the AFM laser onto the end of the cantilever. This is achieved by moving the position of the laser generator within the scanning tower relative to the probe unit The reflected laser light is detected by the photodetector which is divided into four quadrants labelled top (t), bottom (b), left (1) and right (r). Each quadrant detects light intensity independentiy and records a value in nA. The photodetector can provide three types of information about the reflected light; the intensity, the lateral position and the vertical position. The intensity value is generated by adding the total light detected in all four quadrants (t+b+l+r). This is maximized by moving the laser to an optimum position. The lateral position is generated by subtracting the light detected in the right quadrant from the left quadrant (l-r). This value is set to 0 nA by rotating the mirror assembly in the horizontal plane. The vertical position is generated by subtracting the bottom detector value from the top (t-b). This t-b value is the measure of the angle of the laser reflecting from the probe unit and, therefore, is a measure of the deflection of the probe unit and hence a measure of the force experienced between the AFM probe and the sample surface (see section 1.4.2.1). The t-b value is set to a negative value (typically -16 nA) by rotating the mirror assembly in the vertical plane.

Once the laser and mirror assembly position are optimized the AFM probe can be lowered onto the sample surface to generate the repulsive force required for contact imaging. This repulsive force produces a positive deflection of the cantilever and is detected by an increase in the t-b value. The graph in Figure 2.4 is a schematic force-distance plot of the relationship between probe-surface separation and t-b reading of the photodetector for an AFM probe approaching a sample surface in air. Initially, at a relatively large probe-surface separation the t-b value is at the preset value of -16 nA. As the stepper motor lowers the AFM head the probe-surface separation decreases. At large separations this decrease has no influence on the t-b value, however, as AFM probe comes within approximately 10 nm of the surface the t-b value rapidly decreases. This decrease is caused by an attractive force acting on the AFM probe. The attractive force is caused by a capillary force generated by a thin layer of water associated with the sample surface (116). As the proba and surface approach closer and contact occurs, the Bom repulsion force begins to

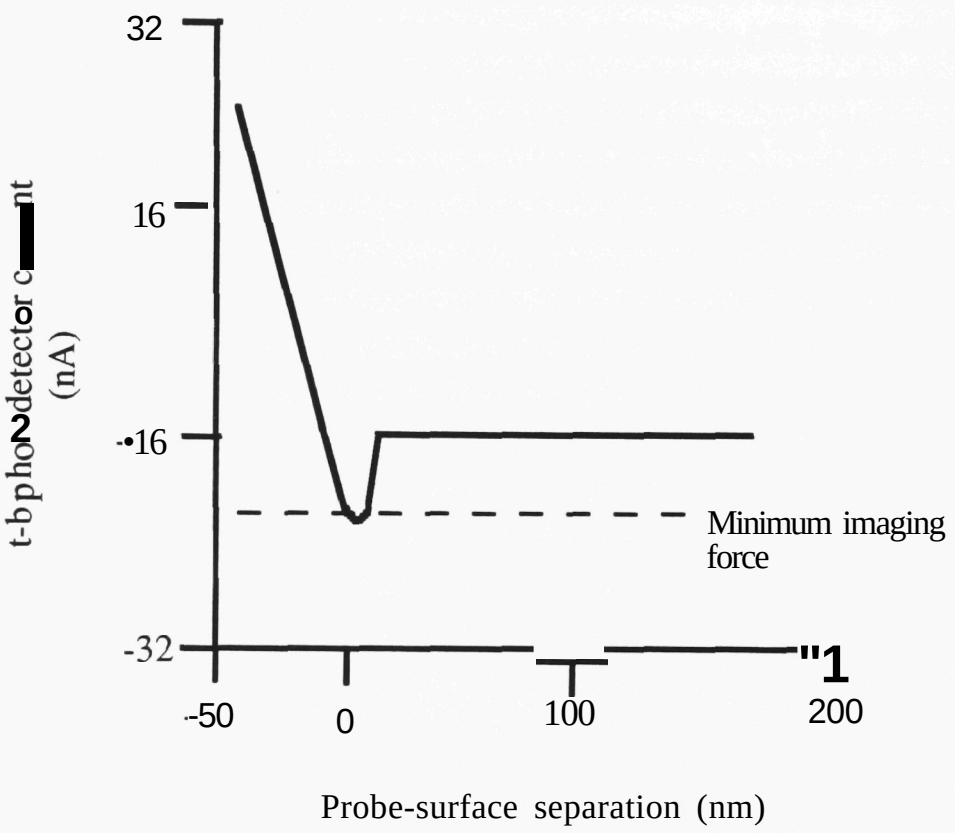


Figure 2.4 Schematic force-distance curve displaying the forces of interaction between an AFM probe and a sample surface in air. Note: negative values for the probe-surface separation indicate a movement of the piezoceramic after contact has been achieved.

overcome the attractive capillary force and the t-b value increases. If the stepper motor continues to lower the AFM height after contact the t-b value will continue to increase at a rate proportional to the spring constant of the cantilever. The control unit senses that the AFM probe has contacted with the sample surface when the t-b value increases to a preset value (typically 0 nA).

The next step in the image acquisition process is the minimization of contact force. This is necessary to minimize the occurrence of probe induced damage occurring to the sample surface during imaging (52). The precise repulsive force can be calculated from the spring constant of the cantilever and the force-distance curve. However, this calculation does not have to be performed for minimization procedure because it is only necessary to decrease the t-b value to the lowest value attained after contact This position is indicated on the force-distance curve in Figure 2.4. and can be achieved by decreasing the set-point from the original value. One problem that is commonly encountered during image acquisition in air is that the attractive force caused by the capillary action of the water layer decreases the t-b value below the sensitivity of the photodetector (-32 nA). If this occurs the set-point cannot be lowered to the optimum value and repulsive forces will be correspondingly higher. Therefore, if sample damage is occurring during imaging, the air environment must be replaced with a liquid environment in which capillary forces are eliminated (116).

After force minimization has been performed, the topography of the sample surface can be analyzed. The equivalent magnification is determined by the preset scan size. For each scan size an appropriate scan speed must be employed. The Explorer can move the probe unit at speeds of up to 600 μm/s allowing 100 scan lines of 3 μm length to be acquired per second (200 Hz). However, at such high acquisition frequencies the linearity and accuracy of the piezoceramics is decreased and, in addition, there is insufficient time for the z piezoceramic to respondent to changes in sample topography causing increased contact forces. Therefore, the scan frequency of images presented in this thesis was kept at 10 Hz unless otherwise stated.

The pixel resolution of the AFM images can be set between 100 x 100 to 500 x 500 in 100 pixel divisions. All images presented are at 200 x 200 pixel resolution unless otherwise stated.

A final parameter which can be controlled during image acquisition is the degree of amplification of the feedback loop between the photodetector and the z piezoceramic. This amplification is controlled by the proportional, integral and derivative values (termed the PID values). As the PID values are increased, the speed of response of the z piezoceramic increases and the AFM images will correspond more accurately to the sample topography. However, if the PID values are too high the z piezoceramic will over-compensate for sample topography causing an oscillation to occur. For all images in this thesis the PID values were set at P = 1, I = 0.5, D = 0.1 for the 3 μm scanner and P = 0.15, I = 0.15 and D = 0.5 for the 150 μm scanner unless otherwise stated.

### 2.1.4 Image Display

AFM images are initially acquired in grey scale mode in which the height value of each pixel is represented by the shade. The highest pixels in an image are shown in white, the lowest pixels in black and intermediate heights are represented by different shades of grey. The height difference between a white and black pixel is quoted with the image. An example of a two-dimensional grey-scale image of a diffraction grating is shown in Figure 2.5a. The software of the Topometrix can also translate a two-dimensional grey-scale image into a three-dimensional representation as shown in Figure 2.5b.

Another image display mode frequentiy used in this thesis is shaded mode. In shaded mode, the AFM image is displayed as if a light source has been shone at the surface at an angle of 45° and fine detail in the image topography is highlighted. Two- and three-dimensional shaded representations of the diffraction grating are displayed in Figures 2.5c and d.

### 2.1.5 Variations for the Rasterscope 3000

The major design variation for the Rasterscope 3000 is that the piezoceramic tube are sited below the sample and the probe unit remains stationary in the x and y dimensions during scanning. One tube scanner head with a maximum lateral displacement of approximately 5 μm was used for all AFM analysis.

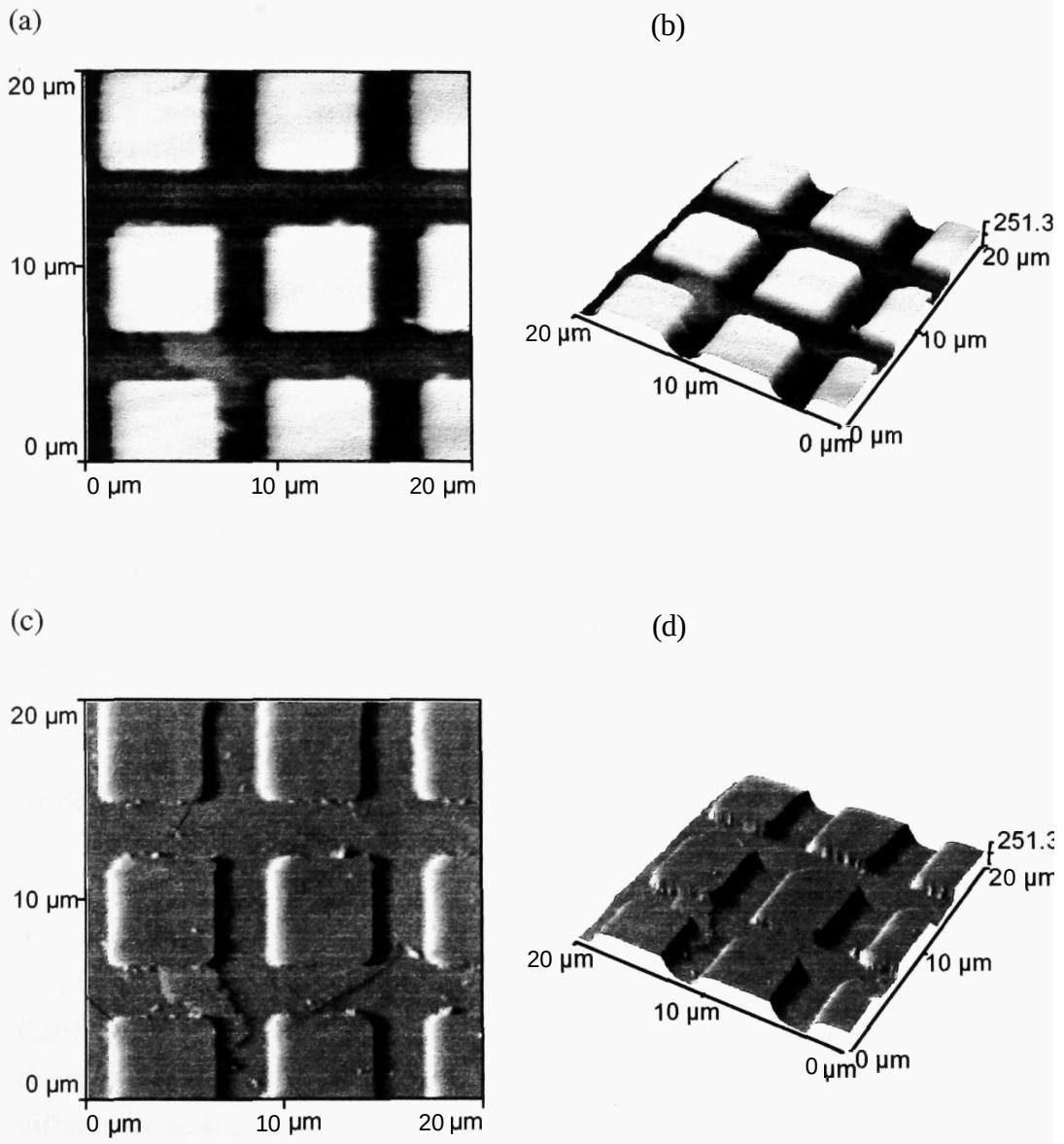


Figure 2.5 Display modes for data acquired by the Explorer.
(a) Two-dimensional grey scale mode.
(b) Three-dimensional grey scale mode.
(c) Two-dimensional shaded mode.
(d) Three-dimensional shaded mode.

The image acquisition procedure is similar to the procedure for the Explorer, but the Rasterscope 3000 uses a two-quadrant photodetector (top and bottom only). The Rasterscope 3000 provides no precise value for t-b in nA but instead estimates an actual repulsive force in nN. The relative repulsive force can be varied during imaging by changing this value, but for imaging in air the actual force will not be the same as the quoted force due to the attractive capillary force described in section 2.2.4. For all the Rasterscope 3000 AFM data presented in this thesis the nominal repulsive force was sat at 1 nN, unless otherwise stated.

The pixel resolution of AFM images can be set to 64 x 64, 128 x 128, 256 x 256 or 500 x 500. All image acquired on the Rasterscope 3000 are 256 x 256 pixel resolution unless otherwise stated.

The feedback loop amplification is controlled by one parameter, termed the loop gain which performs the same function as the PID values of the Explorer. The loop gain value was set to 0.25 unless otherwise stated. In general, this loop gain value was acceptable for all 5 μm x 5 μm images but needed to be lowered as the scan size was decreased to avoid cantilever oscillation.

All Rasterscope 3000 generated AFM images are displayed in grey-scale mode in three-dimensional representations.

### 2.1.6 Calibration

Calibration of the piezoscanners of the AFM is necessary in all three-dimensions. The most common method of calibration was to image a standard diffraction grating sample as demonstrated in Figures 2.5a to d. From the known dimensions of the grating the piezoceramic movements can be calibrated over lateral length scales of 1 to 150 μm. AFM imaging of the diffraction grating was performed on a daily basis to ensure that the proba unit was functioning prior to analysis of polymeric samples. Calibration of the AFM from the diffraction grating images was performed regularly.

The length scale of the divisions in the diffraction grating are on the

micron scale and therefore, this method of calibration cannot be used for higher resolution images from which nanometric measurements are to be made. Instead, other calibration samples, possessing known lateral and vertical dimensions have been employed.

For calibration on the atomic scale, freshly cleaved muscovite mica (Agar Scientific, Cambridge, UK) was used as a calibration sample. Mica is a three layered stmcture of $KAl_2(Si_3Al)O_{10}(OH)_2$ which can be cleaved along the 001 plane. The 2.9 nm x 2.9 nm AFM image in Figure 2.6a shows an image of the atomic surface stmcture of mica obtained with the Rasterscope 3000. Lin and Meier have attributed the features observed on such images to pairs of oxygen atoms, with a known separation of 0.53 nm, tetrahedrally coordinated to the underlying silicon layer (117). The ability to obtain atomic resolution of mica and other mineral surfaces has been demonstrated by many groups (118-123). The imaging mechanisms of these atomic scale topographs is a controversial subject. For imaging in contact mode, at a relatively high contact force, it appears that the AFM topograph is observing changes in friction as the top layer of the mica is pushed over the lower layers (118). Despite difficulties in understanding the imaging mechanism this method of calibration remains valid, while the features may not be generated by the actual surface topography, the spatial resolution of the features is still generated by the separation of the oxygen groups.

One drawback with the use of atomic scale imaging for calibration is that no height information can be obtained and therefore z calibration cannot be performed. To overcome this limitation the imaging of 5 nm diameter colloidal gold samples has been employed. The 500 nm x 500 nm AFM image in Figure 2.6b shows a typical image of a sample prepared by drop casting a 0.01 % w/v solution of colloidal gold (Polysciences Inc., Warrington, UK) in water onto freshly cleaved mica. The minimum steps in height that are observed correspond to the height difference between monolayers of the gold particles and can be used for nanometre scale z calibration. Multilayer steps can also be observed on the images and, therefore, it is important to obtain a number of images and find the minimum step height change.

A final technique used for calibration has been the imaging of arrays of polymer microparticles. Two-dimensional arrays of microparticles can be

(a)

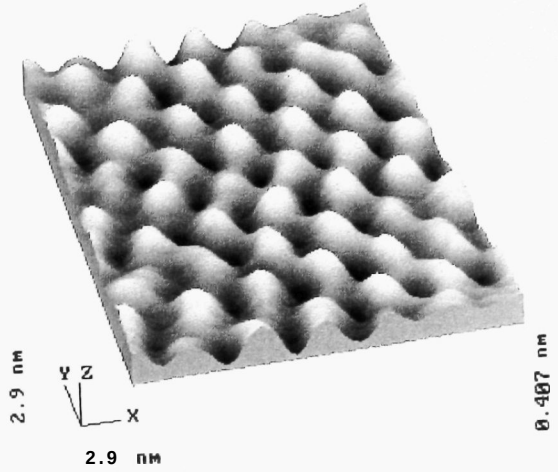


(b)

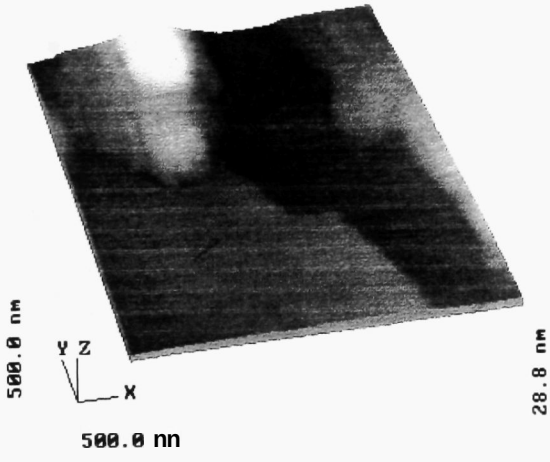


Figure 2.6 CaUbration of the AFM.
(a) Atomic resolution of mica, the image contrast is generated by pairs of oxygen atoms (nominal imaging force 50 nN, scan frequency 100 Hz).
(b) Imaging layers of 5 nm diameter colloidal gold, the arrow indicates a step between layers.

**(c)**

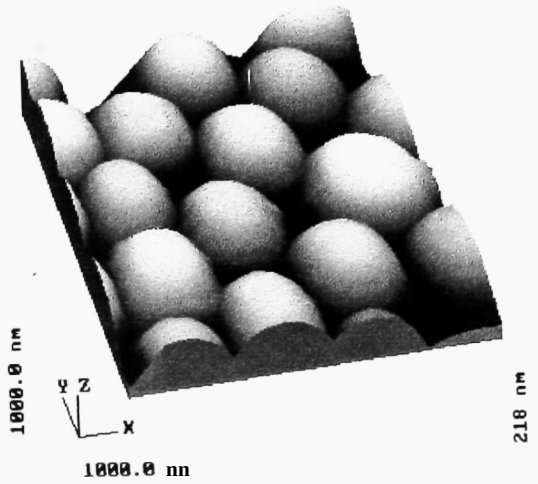


(d)

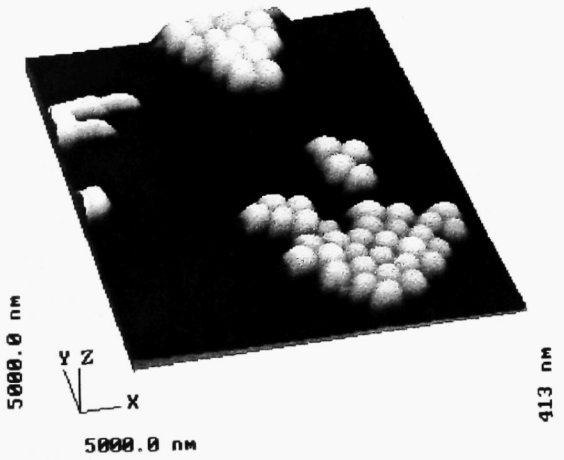


Figure 2.6 Calibration of the AFM.
(c) Two-dimensional array of 250 nm diameter polystyrene particles.
(d) Height calibration using a sub-monolayer coverage of the particles on mica.

prepared by drying a dilute suspension onto a flat substrate such as mica. The 1 µm x 1 µm AFM image in Figure 2.6c shows an array of 250 nm diameter polystyrene particles. X and y dimension calibration from this type of sample can be performed by fmding areas of the topography in which the particles form a face-centred-cubic morphology and measuring tiie average particle diameter. Calibration in the z-dimension can be performed by finding an area where there is a sub-monolayer coverage of the substrate by the particle array. An example of this type of area is displayed in Figure 2.6d. Cross-sectional analysis of the step height between the substrate and the particles then enables z calibration.

### 2.1.7 Image Analysis

The analysis and measurement of the three-dimensional features of AFM data has been performed with the Genesis II graphics system. This system has been developed by Philip Williams at the Laboratory of Biophysics and Surface Analysis (123) with the aim of correlating SPM data with complementary biophysical tools such as molecular modelling and X-ray crystallographic data. For the purposes of the work in this thesis the Genesis II graphics system has been employed to perform accurate measurement of features in the z-dimension and the quantification of changes in matrix volume during polymer degradation.

Prior to analysis on the Genesis system, AFM data acquired on either the Explorer or Rasterscope 3000 instmments is stored and categorized on a 12 Gb optical disk drive. Analysis is then performed on a three-dimensional bitmap of the original AFM image. The full procedure for volume analysis was developed as part of this thesis and will be fully described in Chapter 4.

## 2.2 Surface Plasmon Resonance Analysis

### 2.2.1 Theory

Surface plasmon resonance (SPR) analysis is a technique used to monitor changes in the optical properties of thin films. For the work in this thesis, the technique has been employed to monitor the kinetics of polymer degradation. The application of SPR analysis in biomedical research will be reviewed in

Chapter 6. Here, the basic theory of the technique is described.

A schematic representation of an SPR with a Kretschmann configuration (124) is shown in Figure 2.7. The sample to be analyzed is coated onto an SPR sensor, which consists of a glass with a thin layer of silver (approximately 50 nm thick) evaporated onto the upper surface. The SPR sensor is placed onto the hemi-cylindrical prism and the refractive indices of the glass slide and the prism are matched using microscope immersion oil (Resolve©, Stephens Scientific, Riverdale, USA). The plane polarized laser is shone though the lens to generate a convergent beam which is directed through the prism onto the underside of the SPR sensor. At angles greater than the critical angle ($\theta_c$), the convergent laser is totally internally reflected from the underside of the silver film. The reflected light passes through a second lens and the intensity is measured by the array of photodetectors.

SPR analysis is based on phenomena that occur at the interface between the sample and the silver film. At this boundary, the surface electrons can oscillate at discrete frequencies to generate a charge-density wave (called a surface plasmon) which propagates along the metal surface (125). The wave vector of the surface plasmon ($K_{sp}$) can be approximated by (126):

$$K_{sp} = \frac{w_o}{c}\sqrt{\frac{\varepsilon_m \eta_s^2}{\varepsilon_m + \eta_s^2}} \qquad [2.1]$$

where $w_o$ = plasma frequency

$c$ = speed of light in a vacuum

$\varepsilon_m$ = dielectric constant of silver film

$\eta_s$ = refractive index of sample

As a result of the incident laser interacting with the metal film an evanescent field is generated on the sample side of the silver film. The wave vector of this

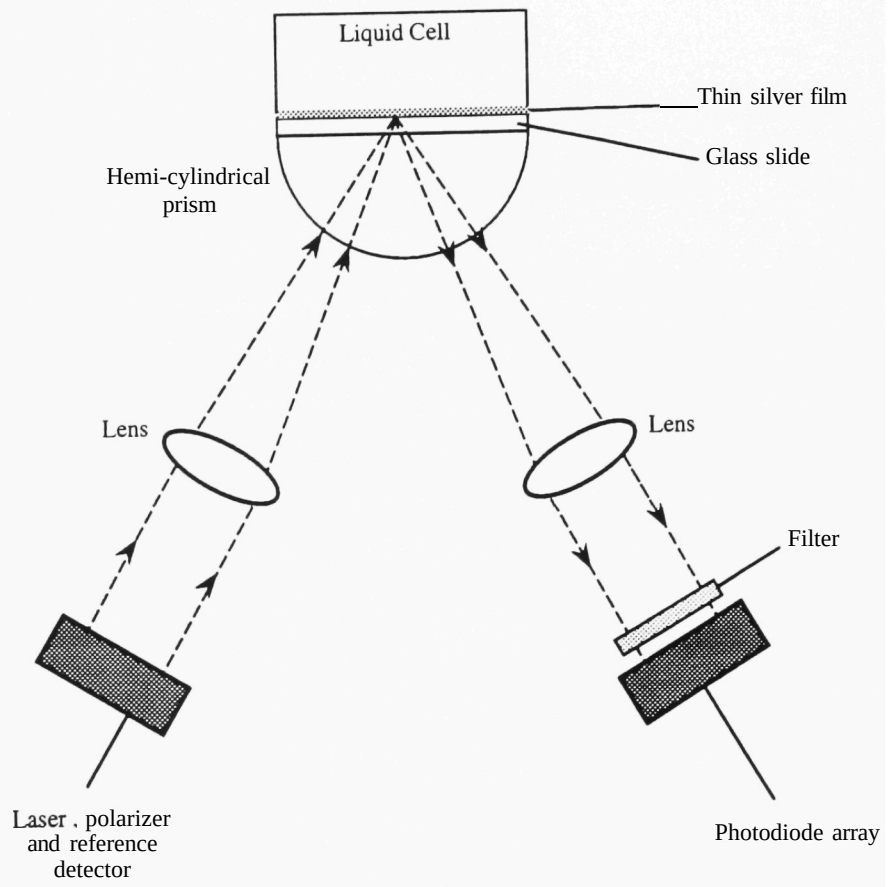


Figure 2.7 Schematic diagram of a surface plasmon resonance instrument.

field is given by:

$$K_{ev} = \frac{w}{c}\eta_g \sin\theta \qquad [2.2]$$

where $w_o$ = frequency of incident light

$\eta_g$ = refractive index of the prism

$\theta$ = angle of incidence of laser on SPR sensor

At a specific angle of incidence of the laser on the SPR sensor $K_{sp} = K_{ev}$ and the surface plasmon is resonantiy excited. This excitation is caused by the transfer of energy from the laser to the metal boundary electrons and can be detected by a decrease in the intensity of light detected by the array of photodetectors. Because the laser source is convergent, a portion of the light will be at the correct angle to excite the surface plasmon (this angle is termed the SPR angle, $\theta_{sp}$). An experimental example of the detection of $\theta_{sp}$ for an uncoated SPR sensor is shown in Figure 2.8.

Examination of equation [2.1] shows that $K_{sp}$ is determined by the refractive index of the sample ($\eta_S$). This refractive index will be determined by two factors: the refractive index of the polymer film ($\eta_{POLY}$) and the refractive index of the liquid ($\eta_{LIQ}$) above the film but within the detection range of the SPR. If the value of $\eta_{POLY}$ or $\eta_{LIQ}$ decreases, then $\theta_{sp}$ will be shifted to a lower value. Alternatively, if the polymer film degrades and becomes thinner, then the contribution of $\eta_{LIQ}$ to the overall refractive index of the sample will increase. Therefore, if the liquid refractive index is lower than the polymer refractive index, then $\theta_{sp}$ will again be shifted to a lower value.

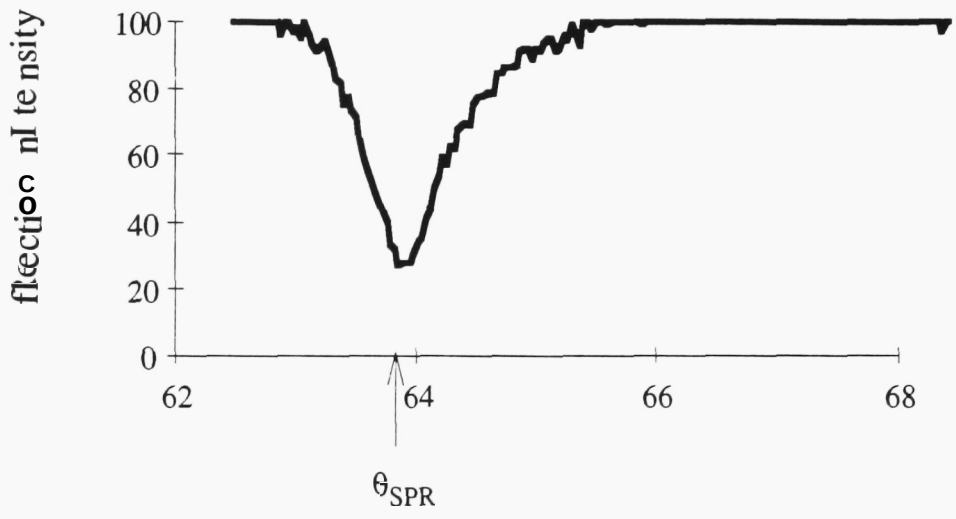


Figure 2.8 Detection of $\theta_{sp}$ for an uncoated SPR sensor.

### 2.2.2 Instrument Design

The SPR instmment was supplied by Johnson & Johnson Clinical Diagnostics (Amersham, UK). The instmment employs a monochromatic laser light source at a wavelength of 780 nm and a hemi-cylindrical prism with a refractive index of 1.518. The SPR sensors were purchased from Johnson & Johnson Clinical Diagnostics where they are manufactured by evaporation coating of silver onto the glass. During data acquisition the WINSPR software plots $\theta_{sp}$ against time. $\theta_{sp}$ can be simultaneously recorded from 9 areas within the laser spot at any one time. Each sampling area has an area of 3.2 x 10* $\mu m^2$ (127).

The aqueous cell above the SPR sensor is divided into three channels. Each channel can be filled with an independent liquid or gaseous environment and this environment can be changed during SPR data acquisition using a syringe driver that can pump liquid into the channels at rates between 0.5 and 64 $\mu l/s$.

### 2.2.3 Sample Preparation

Each sample was prepared on new SPR sensor as supplied. Polymer films were applied to the silver surface of the SPR sensor by spin casting a chloroform solution of the polymer. Unless otherwise stated in the experimental chapters, a polymer concentration of 10 mg/ml and a solution volume of 100 $\mu l$ were used for spin casting at a spin rate of 1000 revolutions per minute. Prior to SPR analysis the sample was allowed to dry under ambient conditions for a period of 1 hour.

## 2.3 Combined AFM/SPR analysis

The combined AFM/SPR instmment is a novel instrument designed and constructed by researchers at the Laboratory of Biophysics and Surface Analysis (128). The aim in designing the instmment was to combine the complementary abilities of the AFM and SPR to visualize dynamic surface events and to quantify the kinetics of these events respectively.

A schematic diagram of the combined AFM/SPR instrument is shown in Figure 2.9 and the major design features are described in the corresponding figure caption. From a design perspective, the combination of the SPR with an SFM is attainable since the SPR signal is accessed from below the sample surface and the AFM accesses the surface topography from above. The SPR instmment described in section 2.2.2 possesses an open sample architecture suitable for combination with an AFM and the positioning of the piezoceramics of the Explorer AFM above the AFM probe unit also renders this instmment ideal for the combination (section 2.1.1).

A number of modifications were required to realize the combined instmment The Explorer AFM was modified to allow the scanning of the probe unit within a flowing liquid environment through the construction of an enclosed cell. This modification involved shaping the macor casing of the AFM scanner head to allow a tight seal to be made with a silicone 0-ring. The SPR was positioned on the underside of a heavy gauge adaptor plate at a point where an opening for the silver coated sample slide was located. The mass of the plate helped to reduce mechanical vibration induced noise in the AFM data The SPR power supply, cooling system and other electrical components were also positioned extemal to the combined instmment in a remote housing to further diminish instmmental noise. Slots were milled into the SPR top plate to allow the precise location of the AFM and hence probe over the SPR slide.

During data acquisition both the AFM and SPR components were employed as described in their respective sections (AFM section 2.1.3, SPR section 2.2.2). To minimise the influence of flowing liquid on AFM imaging, the syringe pump of the SPR unit which initiates fluid flow was switched off during the short time of image acquisition.

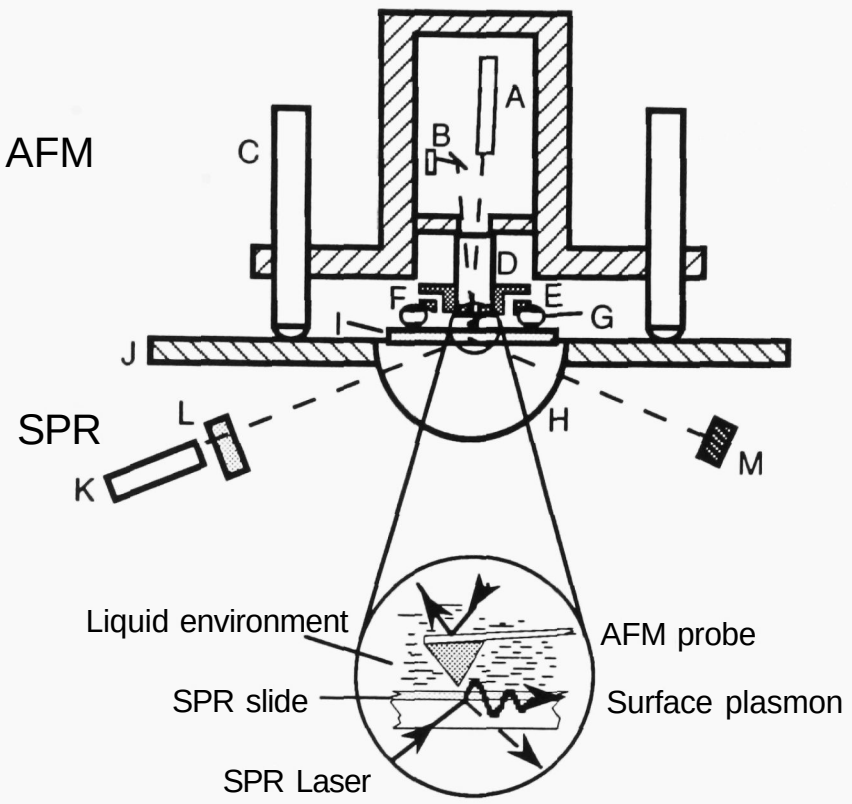


Figure 2.9 Schematic diagram of the combined AFM/SPR.

The key is as follows: A: AFM laser; B: photodiode detector; C: AFM height screws; D: scanner tube; E: liquid inlet; F: liquid outiet; G: silicon 0-ring; H: semi-cylindrical prism; I: silver coated SPR slide; J: SPR top plate; K: SPR laser; L: polariser; M: ccd detector. The SPR was positioned on the underside of a heavy gauge adaptor plate at a point where an opening for the silver-coated sample slide was located. The mass of the plate helped to reduce mechanical vibration induced noise in the SFM data. The SPR power supply, cooling system and other electrical components were also positioned extemal to the combined instmment in a remote housing to further diminish interference effects. Slots were milled into the SPR top plate to allow the precise location of the AFM and hence the probe over the SPR slide. The macor housing on the piezo scanner of the AFM was bevelled at its edges so as to secure a soft silicon 0-ring on the scanner tube. This contacts to the SPR slide thus forming an enclosed liquid tight cell. The softness of the 0-ring avoids excessive transmission of vibrations from the SPR to the SFM. Diagram by C.J. Roberts.

# Chapter 3

## Initial Studies of Polymer Surface Morphology by Atomic Force Microscopy

The surface properties of polymeric biomaterials define many of the interactions that occur when a biomaterial is employed in the body. In Chapter 1, it was emphasised how these interactions control the biocompatibility and functionality of the biomaterial (section 1.2). The general term "surface properties" encompasses both the chemical and morphological nature of the surface. The chemical nature of the constituent polymers will govern the thermodynamics of interfacial interactions such as the wetting of the polymer by the aqueous environment and specific interactions with biomolecules. However, to understand the *in vivo* behaviour of biomaterials it is also necessary to consider the way in which the individual polymer molecules are organised at the surface, i.e. the surface morphology.

The importance of surface morphology to biomaterial science can be illustrated by its influence on two key areas of biomaterial function, biodegradation and protein/cell adhesion. In the characterization of polymer biodegradation it has been demonstrated that the rate of surface erosion of semi-crystalline polyanhydrides is not determined solely by the inherent lability of the anhydride linkage, but also by the relative contribution of amorphous and crystalline polymer morphologies to the overall polymer matrix (129). In this example, the influence of surface morphology is exerted through the different water permeability of amorphous and crystalline material. In second area of biomaterial function, protein and cell adhesion, it has been shown that the tendency for these processes to occur can be directly linked to the roughness (130) and porosity (131) of implant surfaces.

The influence of surface morphology is acknowledged by the inclusion of microscopy studies in many published papers on biomaterials. At present, the vast majority of surface microscopy is performed with a scanning electron microscope (SEM) or a light microscope operating in a reflected mode. The development of the AFM has provided a new microscopy technique which can complement the data obtained from polymeric biomaterials by these

conventional microscopes. The work described in this Chapter explores the advantages and disadvantages of applying the AFM to tiiis field. Before these can be considered, it is necessary to briefly summarize tiie contributions of SEM and light microscopy.

## 3.1 Microscopy of Polymeric Biomaterial Surfaces

There exists a wide range of microscopy techniques available to study polymer morphology. However, only a limited number of these techniques can be used to obtain stmctural information from the surface of a polymer sample. In general, only data obtained from electrons or light reflected from a sample can be used to characterize surfaces. Techniques such as transmission electron microscopy and polarized light microscopy require the probe (ie. electrons or photons) to pass through the sample and so the data is dependent on the intemal stmcture of the sample.

### 3.1.1 Scanning Electron Microscopy (SEM)

SEM is the dominant form of microscopy used to characterize polymeric biomaterial surfaces. Images of the surface are obtained by monitoring the intensity of secondary electrons emitted from a sample as a fine electron beam is rastered across the surface (132).

The resolution of the SEM is dependent on the interaction volume of the imaging electrons, which is controlled by the diameter of the electron beam ($\geq$ 10 nm), the electron density of the sample surface and the voltage applied to accelerate the electrons. On an ideal surface this allows features of approximately 10 nm diameter to be resolved (133).

An important attribute of the SEM is large depth of field of data (132). The depth of field is the vertical distance over which the microscope can provide adequate definition of sample features. The depth of field of a conventional SEM is approximately 100 times greater than that of light microscopy, making SEM images of rough and porous samples easy to interpret.

A number of problems complicate the analysis of polymeric biomaterials

by SEM. The low electron density of the polymers and their electrically insulting nature prohibits direct imaging. These two characteristics would result in the chemical mpturing of bonds of the polymer and the build up of negative charge if the sample was imaged without further preparation. Therefore, it is a standard procedure to coat polymers with a thin metallic layer before SEM analysis (134). The application of the metallic fihn to the surface morphology of the sample can obscure fine topographical features reducing the resolution of the technique.

For most biomaterial surfaces the attributes of the SEM more than outweigh the problems. The instmment is now widely available and is responsible for the majority of published studies on biomaterial surface morphology. The examples in Table 3.1 give an indication of the many areas of biomaterial science in which SEM is applied.

Recently, a number of new types of SEM have been described and employed to record surface information from polymeric biomaterials. These new types of SEM aim to overcome the limitations imposed by the interaction between electrons and insulating, low electron density, polymers.

Cryogenic SEM has been demonstrated in the analysis of the formation gel layers in sodium alginate controlled release devices (139). The advantage of using cryogenic technology is that the polymer surface is preserved is its hydrated morphology. The development of cryogenic SEM addresses the potential problem of exposing polymeric biomaterials to vacuum conditions during the coating process.

Environmental SEM (ESEM) represents a major advance in the microscopy of polymeric biomaterials because it allows samples to be analysed within a gaseous environment The ESEM has been defined as "..an SEM capable of maintaining a minimum water vapour pressure of 609 Pa in its specimen chamber." (140,141). The implication of this definition is that liquid water is present on the surface because at room temperature 609 Pa is the saturation pressure of water. In addition, to ensuring the presence of water on the samples surface, the presence of a gas in the chamber has the beneficial effect of suppressing the build of negative charges on the sample, hence, polymers can be imaged without the application of the thin metallic coating,

| Biomaterial | Information Obtained | Reference |
|---|---|---|
| Biodegradable polymer | Surface microstructure changes during erosion | 135 |
| Vascular grafts | Spherulite organization of block co-polymers | 136 |
| Cell transplantation scaffolds | Pore size | 131 |
| Membrane implants | Granular stmcture of film surface | 137 |
| Surface coated dacron | Change in coating stmcture due to washing | 138 |

Table 3.1 Examples of areas of application of SEM in biomaterial surface analysis.

although the lateral resolution of ESEM is limited compared to the conventional SEM. The ESEM has considerable potential in biomaterial analysis. Its use has been successfully demonstrated in the investigation of the effect of ultrasound on polyanhydride matrices (142) and the behaviour of thermoresponsive microspheres (143).

### 3.1.2 Light Microscopy

In the general field of polymer microscopy, Ught microscopy is extensively and successfully employed (144). The term light microscopy covers a number of different techniques, such as transmission, polarized and phase contrast microscopy, which harness different properties of the interactions between light and polymeric materials. However, most of the successful forms of light microscopy provide information on the intemal organization of polymer samples. Reflected modes of light microscopy are often less informative due to the low surface reflectivity of most polymers. As a result most surface studies have relatively poor image contrast and resolution in comparison with SEM images.

Despite the limitations of conventional light microscopy for surface analysis, the technique still has an important role in biomaterial science due to the non-destructive nature of the imaging mechanism and low cost of the instmment. Recent examples of reflected light microscopy studies include the measurement of spherulite density on the surface of poly(L-lactide) fihns (145) and the surface organization of a blend of poly(L-lactide) and lactic acid (146). In both these studies the lateral resolution was not higher than 10 μm and the image contrast was low.

One potential method of enhancing the use of light microscopy for the analysis of surfaces is the use of interference techniques. In this form of microscopy a beam splitter is employed to generate a sample and reference beam. The sample beam is directed onto the polymer surface and on reflection from the surface is re-combined with the reference beam. Image contrast is enhanced by the pattems of interference generated by this re-combination. Examples of the application of this type of microscopy and the related Nomarski interference microscope include the visualization of fibrils on the surface of

polypropylene (132, 144).

The work described in this Chapter has aimed to investigate the potential role of the AFM in analyzing the surface morphology of polymeric biomaterials and to assess how the instrument can augment the established electron and light microscopes. The AFM has specific attributes which can be exploited in biomaterials analysis, such as the high vertical sensitivity of the technique and the simple sample preparation procedures required prior to imaging. These attributes are explored on fdms of poly(ethylene oxide) (PEO) (600k).

PEO is a semi-crystalline polymer which displays excellent biocompatibility properties (147). This biocompatibility has been attributed to the unique interactions that occur between PEO and water. In comparison with poly(methylene oxide) and poly(propylene oxide), PEO displays a higher than expected solubility in water. This is believed to be caused by PEO molecular stmcture allowing 4 water molecules to hydrogen-bond with the polymer unit cell without distortion of the water lattice stmcture (147). It is thought that when PEO is present at the surface of biomaterials within the body, the interactions with water lead to the hindering of protein adsorption and therefore the presence of PEO can delay the rejection of synthetic materials by the body (148).

The results presented in this Chapter address three issues in the application of AFM in biomaterial analysis. The first study investigates the type of morphological data that can be obtained from a sphemlitic PEO film. This study aims to introduce the potential strength of the AFM in characterizing polymer organization over a wide range of length scales. The second study investigates how the organization of the PEO material on the nanometre scale can be influenced by sample preparation parameters. Finally, some of the adverse interactions which can occur as the AFM probe scans the PEO samples are described.

## 3.2 Experimental Methods

### PEO solution preparation

PEO (600k) (Aldrich, Dorset, U.K.) aqueous solutions were prepared by leaving the solid polymer in contact with high purity deionized water (purified

on an ELGA water system) without agitation. Polymer solutions were used after 6 hours contact between polymer and solvent. For experiments requiring temperature control during sample preparation (see section 3.3.2.2) both the polymer solid and water were warmed or cooled to the desired temperature before mixing. The concentration of the PEO solution is noted in the relevant section of the Results and Discussion.

**Film formation**

Drop cast films were produced by dropping a 2 μl aliquot of the polymer solution onto freshly cleaved mica (Agar Scientific, Cambridge, U.K.). Films were dried in laboratory conditions for 1 hour before AFM analysis. Spray deposition of the polymer solution was performed horizontally onto mica at a distance of approximately 30 cm by introducing a 20 μl aliquot of the polymer solution into a stream of nitrogen gas.

## 3.3 Results and Discussion

### 3.3.1 Surface Morphology of PEO spherulites

Two-dimensionally constrained sphemlites were produced by drop casting a 10mg/ml PEO solution (aq) onto the mica substrates. These sphemlites provide an excellent morphology on which to study the ability of the AFM to image polymer organization on a wide range of length-scales. The AFM image in Figure 3.1a shows an example of this sphemlitic morphology on a 80 μm x 80 μm scan. The sphemUte consisted of a nucleating centre (indicated by the label) which had the appearance of a dense mass of fibres. Away from the nucleating centre the PEO material had been deposited in a radiating pattem. A large number of fibres, with diameters between 500 nm and 1 μm could be observed in this area. The surface lacked a distinct morphology between the fibres. In the latter stages of film formation polymer material from neighbouring sphemlites impinged and distinct grain boundaries formed. The AFM image in Figure 3.1b shows an area where grain boundaries had formed between three neighbouring sphemlites.

The fibrous morphology of the sphemlites was further explored in a series of 5 μm x 5 μm images. Figure 3.2 displays typical AFM images at this

(a)

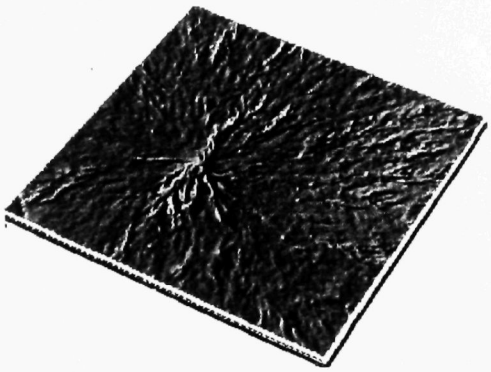

(b)

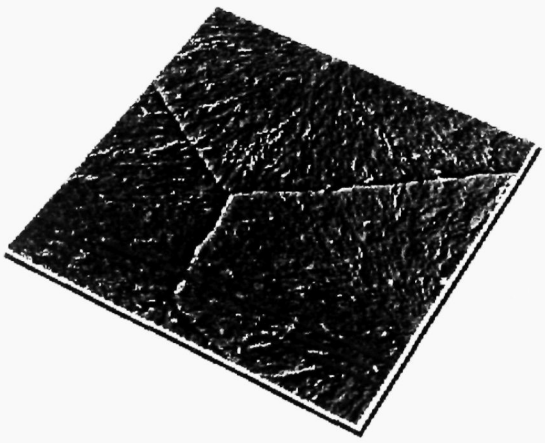

Figure 3.1 (a) 85.85 μm x 85.85 μm AFM image of a PEO sphemUte. Shaded view, scan frequency 5 Hz. Maximum height of image feature 2000 nm.
(b) 150 μm x 150 μm AFM image showing grain boundaries between three PEO sphemUtes. Shaded view, scan frequency 5 Hz. Maximum height of image feature 1735 nm.

(a)

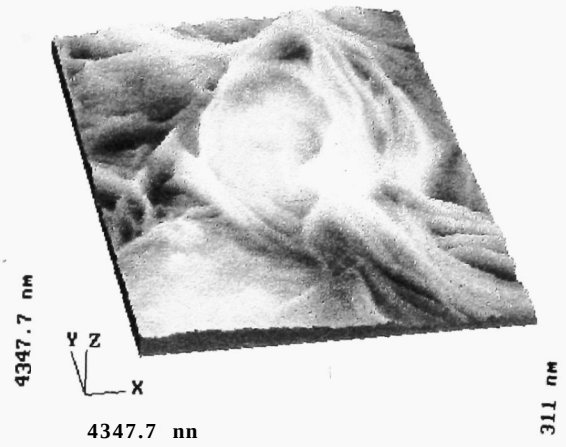


(b)

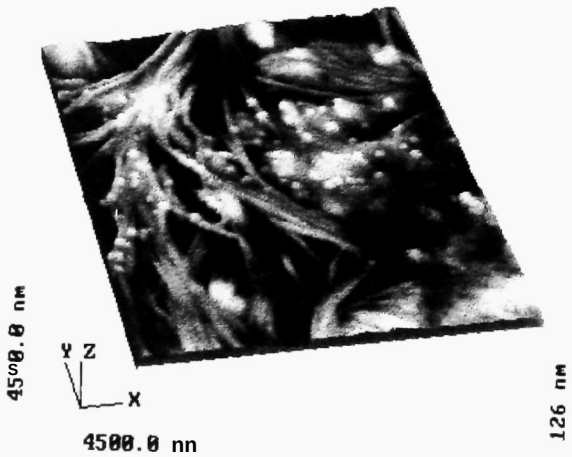


Figure 3.2 (a) and (b) 5 μm x 5 μm AFM images showing the fibrous morphology of the PEO sphemUtes. Grey-scale view, loop gain (a) 0.7 (b) 0.3, nominal force (a) 1.2 nN (b) 0.2 nN.

length scale. The AFM analysis revealed that the 500 nm to 1 μm fibres identified on the large scale AFM images in Figure 3.1 were, in fact, composed of smaller fibres bundled together. The diameters of the smaller fibres ranged between 40 and 100 nm. Also evident on the AFM images in Figure 3.2 are areas between the fibre bundles which lack any directional orientation.

The surface morphology observed in the AFM images in Figures 3.1 and 3.2 can be adequately explained by current theories of sphemlite formation (150). For solution cast polymer morphologies, the theory of Keith and Padden explains the presence of the radiating fibres and the areas between these fibres. The theory states that sphemUte formation begins with the nucleation of polymer crystallization on the substrate surface. Nucleation sites are most commonly associated with impurities on the substrate or within the polymer solution. Once the nucleating site has formed, polymer chains form lamellar sheets to generate a single crystal morphology. The boundaries of these lamellae radiate out to fill space from the nucleating centre. However as growth continues entangled polymer chains and impurities form a non-crystallizable layer around the lamellae and single crystal growth is prevented. New polymer addition to the crystal can only occur by fibre formation with the non-crystallizable material vitrifying around the growing fibres. This non-crystaUizing material generates amorphous material around the crystalline fibres. The AFM images in Figure 3.2 clearly distinguish both the crystaUine fibres and the amorphous areas of the morphology.

The next stage in the AFM analysis of the PEO sphemlites was to examine the lameUar organization of the fibrous material. Lamellae are the fundamental buUding blocks of all semi-crystalline polymer morphologies. The existence of lamellae and the intemal organization of polymer chains within crystals was first described in 1957 by Keller (75). Keller observed single crystals of polyethylene and found that the thickness of the lameUae was 12 nm. He proposed that to form such a morphology the long polymer chains had to fold to generate a chain-fold pattem. This chain-fold pattem is shown schematically in Figure 3.3. Within single crystals, lamellae can form large sheets which can be easily imaged with the AFM. The images in Figure 3.4 show the stmcture of lamellae within two PEO single crystals which were grown in a solution of toluene over a 5 day period. The lameUae are apparent as steps in crystal stmcture and the height of the steps is determined by the lameUar width.

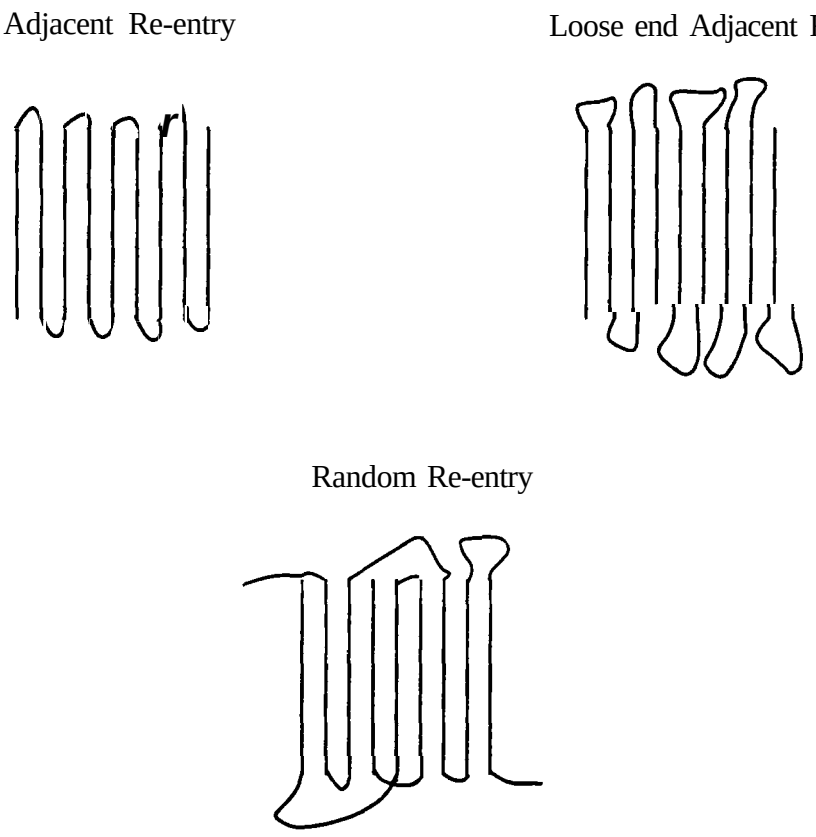


Figure 3.3 Schematic diagram of the chain-folding of polymer molecules into lamellae. The three model differ by the type of folds between neighbouring crystaUized chains.

(a)

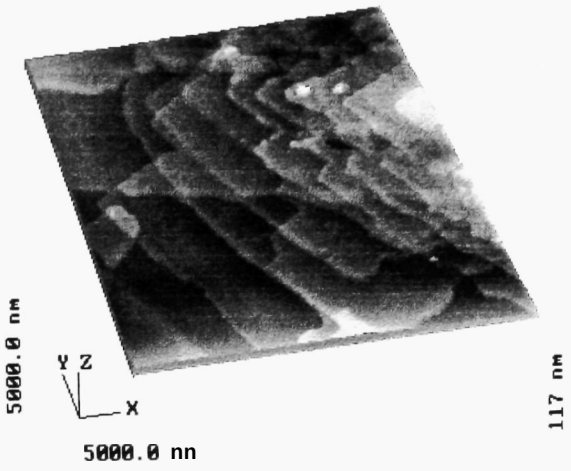


(b)

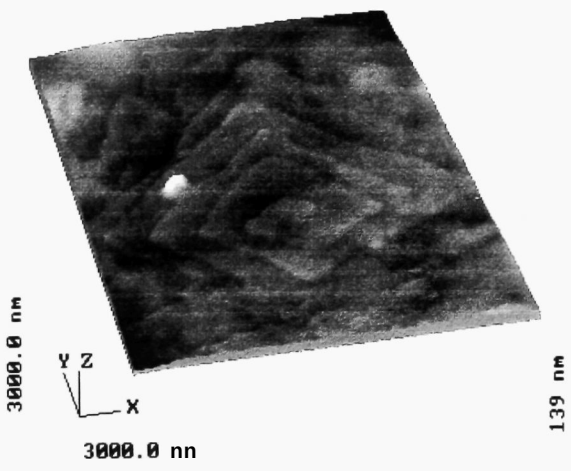


Figure 3.4 (a) 5 μm x 5 μm AFM image of a PEO single crystal growth from a toluene solution. Grey-scale view.
(b) 5 |im x 5 μm AFM image of a PEO single crystal with a screw dislocation. Grey-scale view.

Observation of lamellar units within sphemUtic polymer morphologies was unattainable for a considerable time after Keller proposed the chain fold lameUae model. Prior to the development of tiie AFM, the ti-ansmission electi-on microscope was the dominant tool for studying molecular organization within sphemUtes (37). To obtain resolution of the lamellar detail with TEM requires considerable sample preparation because the low electron density of polymeric material prohibits the direct imaging of most samples. These sample preparation methods have been extensively reviewed by Bassett (37). In general, the sample preparation procedures involve etching the surface of thin sections of the polymer to remove amorphous material from around the lamellae, and hence, increase the potential contrast of the TEM image. In addition, it is common to produce a carbon repUca of the polymer surface after etching and to analyze the topography of the replica.

Using the AFM it is possible to directly image the lamellar stmcture of sphemlite fibres. The AFM image in Figure 3.5 was recorded from the surface of one of the fibres previously observed on the 5 μm x 5 μm image shown in Figure 3.2a. The image shows ribbons stmctures mnning along the lengths of a number of fibres. A cross-section of the AFM image across four of the ribbons is also displayed in Figure 3.5. This cross-section shows that the ribbons have widths between 10 and 30 nm which is in good agreement with the known dimensions of PEO lameUae (95).

Therefore, it has been demonstrated that the AFM can directiy resolve lamellar detail of the surface of two-dimensional PEO sphemlites. This resolution exceeds that of the SEM and matches that of the established TEM procedures. However, AFM imaging avoids the extra sample preparation methods. This is potentially important because it has been demonstrated that etching can alter the crystaUine morphology (37). In addition, etching procedures are not available for all semi-crystalline polymer. Therefore AFM offers the potential to broaden the sample types which can be analyzed at high resolution.

The attribute of the AFM which allows this high resolution on polymer surfaces is the sensitivity of the instmment to height (z) variations in the topography. The cross-section in Figure 3.5 shows that the height variation between neighbouring lamellae is between 5 and 15 nm. The resolution in the z

(a)

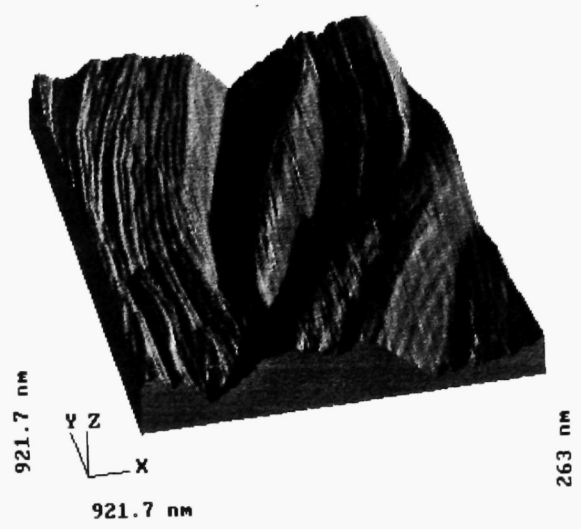


(b)

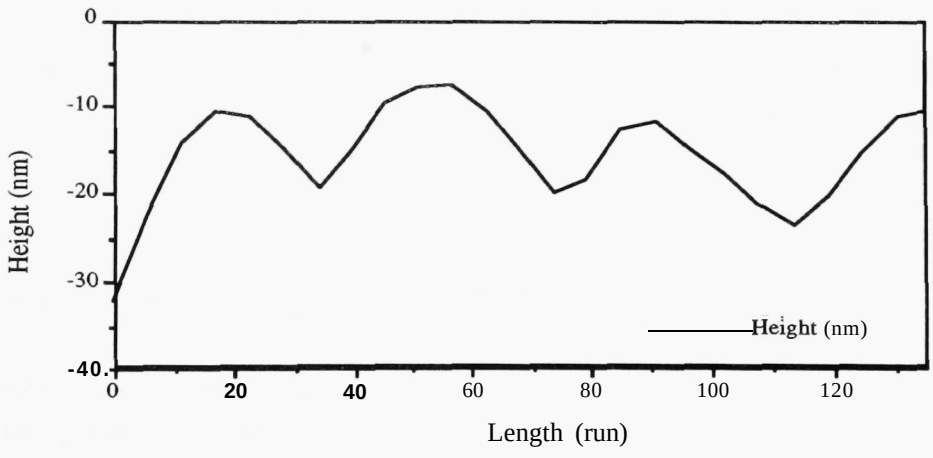


Figure 3.5 (a) 921.7 nm x 921.7 nm AFM image of PEO fibre shown lamellae ribbons. Shaded view, loop gain 0.7, nominal force 1.3 nN.

(b) Cross-sectional data of four neighbouring lamellae.

direction is determined by the sensitivity of the cantilever deflection detection system (ie the laser, mirror and photodiode). Theoretically this resolution limit is less than 1 A (54). Therefore, visualizing the lamellar organization of the PEO fibres is weU within the expected vertical resolution of the AFM.

Attempts were made to resolve the molecular stmcture of the lamellae, however, no finer detail was recorded on smaller AFM scans. The inability to achieve molecular resolution is most likely caused by the amorphous material associated with the folds of chains in lamellae (as shown schematicaUy in Figure 3.3 as part of the random re-entry model). The review of molecular resolution studies in Chapter 1 (section 1.6.2.) stressed that the imaging of individual polymer molecules within films required an organized and rigid surface. These requirements were not achieved due the presence of the amorphous material.

### 3.3.2 The Effect of Sample Preparation on PEO Film Morphology

For semi-crystalline polymers, sphemlites are the dominant morphological feature for thin film samples. In this section, methods of generating non-sphemUtic morphologies are investigated. These methods involve changing the concentration of the PEO solution, changing the temperature of PEO film formation, and changing the method of solution deposition onto the substrate. These studies highlight the importance of sample preparation in controlling the surface morphology of polymeric biomaterials.

#### 3.3.2.1 Polymer Solution Concentration

When the concentration of PEO was decreased to 1 mg/ml the surface coverage of the polymer following drop casting on the mica was insufficient to completely cover the substrate. The AFM image in Figure 3.6 shows a network stmcture typical of the morphology found when this concentration of PEO was used. Such network stmctures have been described for other polymer/substrate systems (94) and result from holes developing in the polymer gel during drying. As drying continues the polymer film contracts and the network forms by expansion of the holes pushing the polymer material into strands.

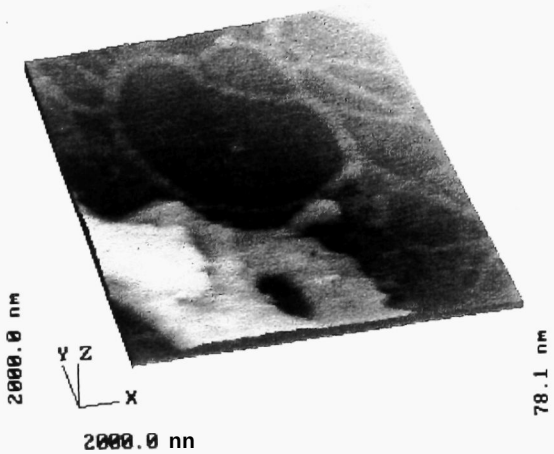


Figure 3.6 2 μm x 2 μm AFM image of a 1 mg/ml PEO concentration sample showing a network structure.

When the concentration of PEO was further decreased to 0.1 mg/ml the polymer morphology shown in the AFM images in Figure 3.7 were observed. In Figure 3.7a, the 3 μm x 3 μm AFM images shows a strand of polymer composed of three distinct ribbons where the PEO appears to have crystaUized. In the areas around this strand there is an indication of fine stmcture which would not be expected for an uncoated mica substrate. The AFM images in Figures 3.7b and c show that this fine detail is composed of polymer strands. These strands have average widths of approximately 8 nm. However, because the strands are isolated features on the flat substrate, the AFM recorded diameter will be an over-estimation of the tme dimensions as shown in the schematic diagram in Figure 3.8. The over-estimation is caused by the tip apex of the AFM probe being larger than the sample feature. Therefore, if we assume that the polymer strand is approximately cyUndrical and that the AFM tip apex is approximately spherical, then the sample feature will first contact with the tip apex at a point some distance *(w* nm) from the tme apex of the tip. Then, after the tme probe apex has scanned over the apex of the molecule, the probe will remain in contact with the molecule for a further *w* nm. The broadened image of the polymer strand wiU therefore have a width of *2w* instead of the tme width of *2q*.

Models have been developed to convert the broadened width to the real width. Thundat *et al* have proposed the circular probe model (151) for which the broadened width is given by:

$$w = 2(Qq)^{1/2} \qquad [3.1]$$

where w = broadened width
Q = radius of probe apex
q = radius of molecule

If this model is applied to the polymer strands in Figure 3.7, then assuming the radius of the probe apex to be greater than 20 nm, the tme width of the features decreases to less tiian 0.8 nm. X-ray crystallography records a value of 0.3 nm for the diameter PEO (152). Therefore, the AFM data appears to have imaged a polymer strand composed of one or two PEO molecules. This hypothesis is supported by the recorded height of the polymer strands above the mica being

(a)

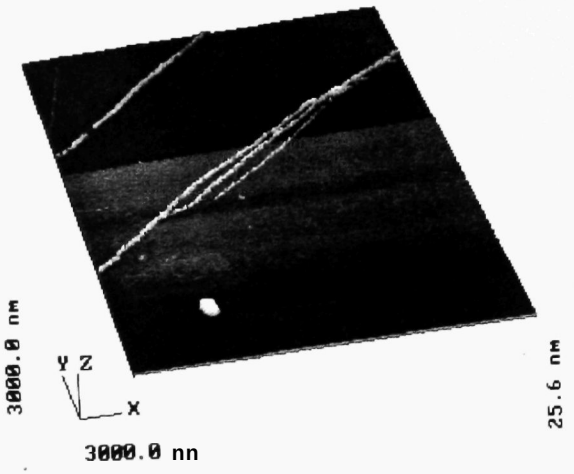


(b)

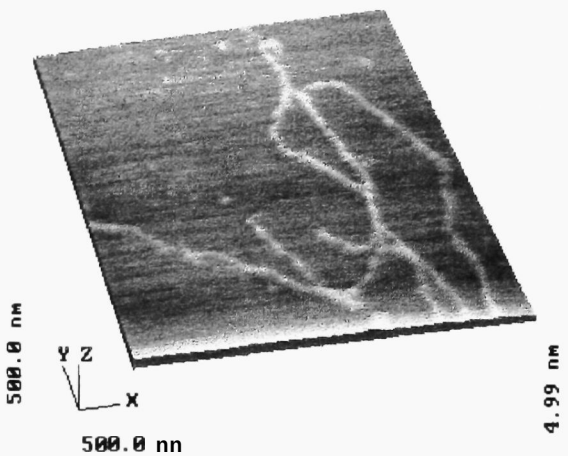


Figure 3.7 AFM images of a 0.1 mg/ml PEO concentration sample.
(a) 3 μm x 3 μm image showing ribbon structures. Grey-scale view, nominal force 0.05 nN.
(b) 500 nm x 500 nm image of single strand structure. Grey-scale view, nominal force 0.07 nN, scan frequency 30 Hz.

**(c)**

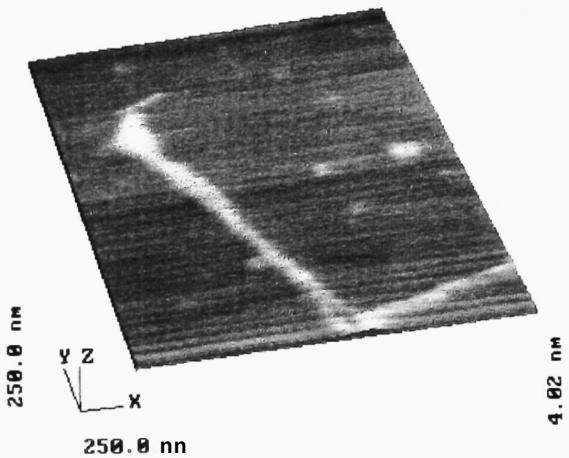


Figure 3.7 (c) 250 nm x 250 nm AFM image of single strand structure. Grey-scale view, nominal force 0.07 nN, scan frequency 60 Hz.

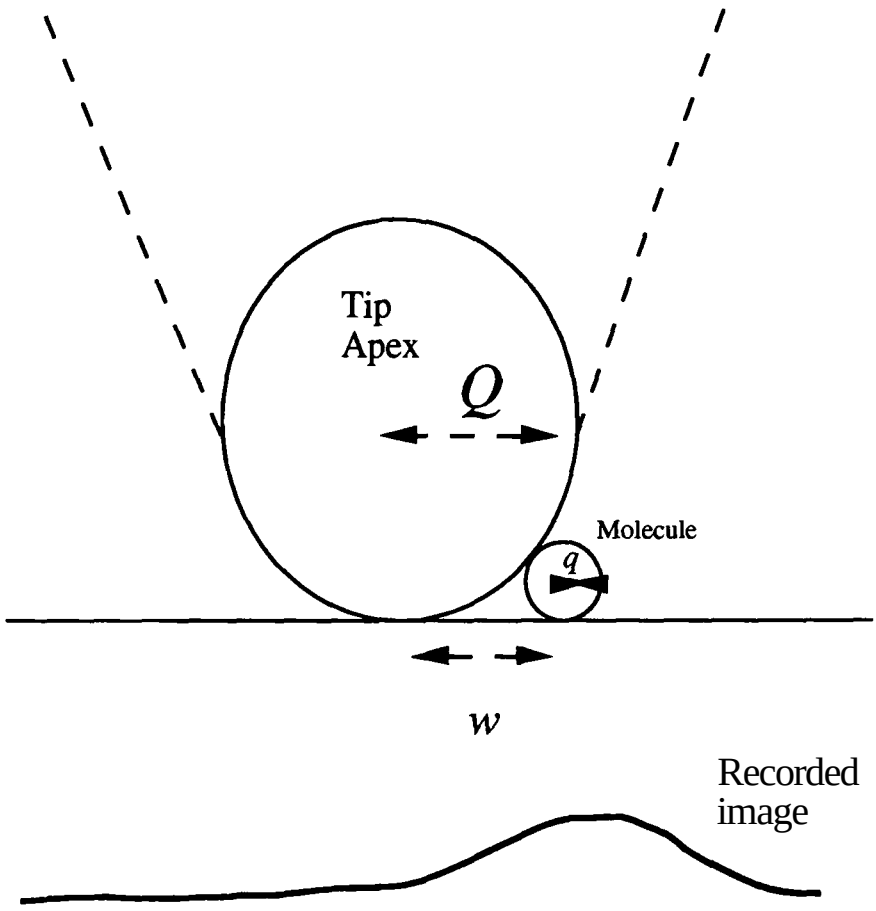


Figure 3.8 Schematic representation of the over-estimation of the dimensions of a molecules due to the finite size of the AFM probe. w = broadened width, Q = radius of probe apex, q= radius of molecule.

approximately 1 nm. However, there are a number of limitations in the circular probe model which restrict the confidence of the calculated tiaie feature width. The model assumes an AFM probe with no surface roughness. In reality, the tip apex will have an inherent roughness which could ensure that the molecule contacts with the probe close to the tme apex. In addition, the height of the feature above the substi-ate can be distorted by the compression of the polymer strand by the probe and by changes in frictional forces acting on the probe as the apex moves from mica to polymer.

### 3.3.2.2 Film Formation Temperature

In this experiment PEO films were produced by drop casting 5 mg/ml aqueous solutions onto mica. The effect of temperature was analyzed by performing the complete process of film formation (ie. polymer dissolution, drop casting and sample drying) at 6, 20, 40, 60, 80, and 96°C.

At 20, 40, 60 and 80°C all samples areas analyzed by AFM displayed the semi-crystalline fibrous texture expected for spherulitic morphologies. However, at 6 and 96°C no fibres were observed on the AFM images and all areas of the sample appeared to possess amorphous morphologies. An example of this amorphous morphology from the 6°C is displayed in the AFM topograph in Figure 3.9.

The absence of fibres in the PEO films formed at 6 and 96°C can be explained by the behaviour of PEO molecules in water at varying temperatures. Flexible long chain polymers, such as PEO, adopt a range of different conformations in solution. These conformations wiU be dynamic but on average in a "good" solvent (153) the polymer wiU tend to maximize polymer-solvent interactions by adopting open conformations (see Figure 3.10). In a "poor" solvent the polymer chains will tend to minimize polymer-solvent interactions by coiling up (see Figure 3.10). The degree of coiling can be measured by the displacement length (r) which is the average separation distance between the end groups of the polymer chains. For many polymer-solvent systems the value of r is dependent on the temperature of the solution. For the PEO-water system, r is large at temperatures between 20 and 80°C ie. the polymer adopts an open conformation. However, as the temperature faUs from 20°C or rises above 80°C

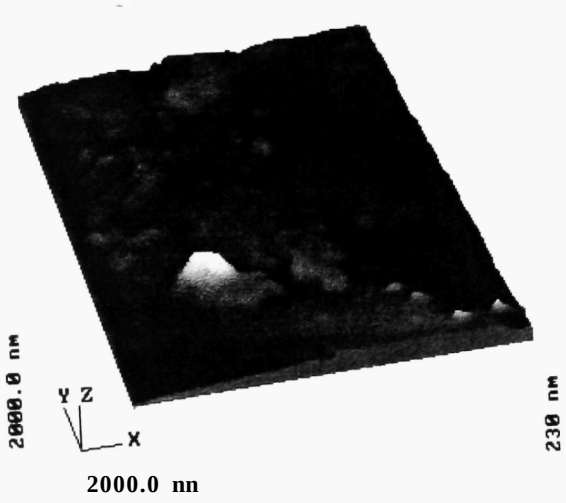


Figure 3.9 2 μm x 2 |im AFM image of a PEO fihn prepared at 6°C. Grey-scale view.

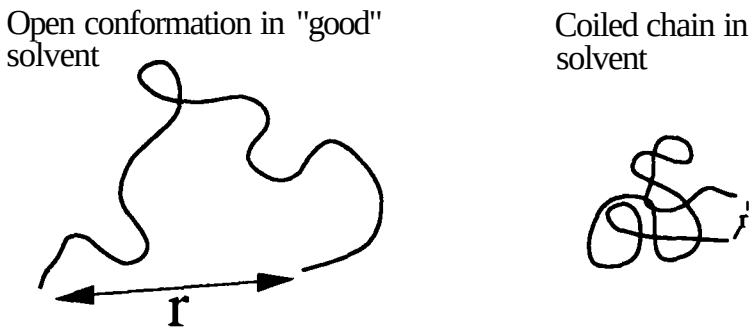


Figure 3.10 Schematic diagram showing the conformation of a polymer chain in a "good" and "poor" solvent r = displacement length.

the affinity of the polymer for water decreases, the PEO chains coil up, and the value of r decreases. This decrease in r continues until the temperature reaches 6°C or 96°C. These values are termed the upper and lower consulate temperatures (153). At these temperatures the degree of polymer coiling is the maximum possible without the polymer becoming insoluble in water.

Relating the behaviour of PEO in water at varying temperatures to the morphology of the PEO surfaces, between 20 and 80°C the open conformation of the PEO molecules simplifies the chain folding process and so sphemlites form. At 6 and 96°C, the polymer chains are unable to chain fold from their coiled conformations within the time limit imposed by the rate of solvent evaporation and so amorphous material is formed as water is lost from the system.

### 3.3.2.3 Spray Deposition of Polymer Solution

The utilization of spray deposition of 5 mg/ml aqueous solutions of PEO inhibited the formation of sphemlites and generated a variety of polymer morphologies in which polymer coverage of the mica substrate was incomplete and isolated polymer structures were generated.

One isolated morphology commonly seen on spray deposited samples was dendrites. The AFM images in Figure 3.11 show an example of a dendritic PEO morphology. Dendritic growth pattems have been extensively researched in the field of metal alloy crystaUization and are often associated with diffusion limited growth (154).

Two interesting features of the dendrite shown in the AFM images in Figure 3.11 are the height of the dendrites above the mica substrate and the right angle habit of the dendritic arms (see labelled arrows). Cross-sectional measurement of the dendrite heights recorded a value between 10 and 15 nm. This value is within the expected range of PEO single crystal lamellae. Further evidence of the single crystal origin of this morphology is the right-angle habit of the dendrites. This right angle habit was previously imaged in the AFM analysis of PEO single crystals (see Figure 3.4). Therefore, it appears that the water is removed from the drying polymer film, perfect lamellae growth is

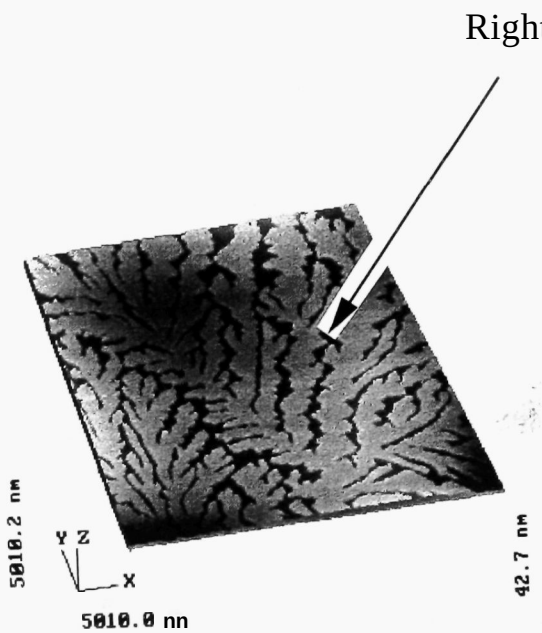


Figure 3.11 5 μm x 5 μm AFM image of a spray deposited PEO sample showing a dendritic morphology. Grey-scale view, nominal force 1.268 nN.

impossible and two-dimensional extension of the morphology becomes diffusion Umited.

Extensive analysis of spray deposition samples revealed a high degree of variation in the observed morphology of the PEO. For most areas of imaging no polymer structures were observed because spraying of the polymer solution will only deposit polymer on areas of the substrate hit by droplets of the solution. In addition to the dendritic morphologies a number of analyzed areas showed a fibrillar morphology of the PEO. An example of this fibrillar morphology is shown in tiie AFM image in Figure 3.12. The fibrils have widths between 30 and 40 nm. a notable morphological feature of these fibrils is the presence of nodes at intervals along tiieir stmcture. PEO fibrillar morphologies have been described previously (155). The underiying polymer organization of fibrils has been described as a "shish-kebab" stmcture (155). In this model the polymer chains are extended to form the long fibril. In the node areas the polymer molecules fold into chain-fold structures.

### 3.3.3 Adverse Interactions Between the AFM Probe and PEO Samples

The examples of AFM imaging of PEO morphologies have demonstrated the considerable potential of the technique in visualizing the organization of the polymer on the nanometre scale. However, it should be noted that the close interaction between the AFM probe and the polymer sample surface can produce adverse interactions. Previously, a number of groups have described how the scanning motion of an AFM or STM probe across a sample surface can lead to the movement or destmction of features (112-114).

Two examples of feature destmction are shown in the AFM images in Figure 3.13. The image in Figure 3.13a shows an area of a spray deposition sample on which a fibrous stmcture has been broken by the action of the probe during the acquisition of the previous scan. In general, it was found that isolated fibres could be destroyed during the acquisition of a small number of images. In contrast, fibres which were part of a complete film were stmcturaUy supported sufficientiy to aUow repeated imaging. The image in Figure 3.14b, shows the only example recorded of the destmction of a sphemlitic

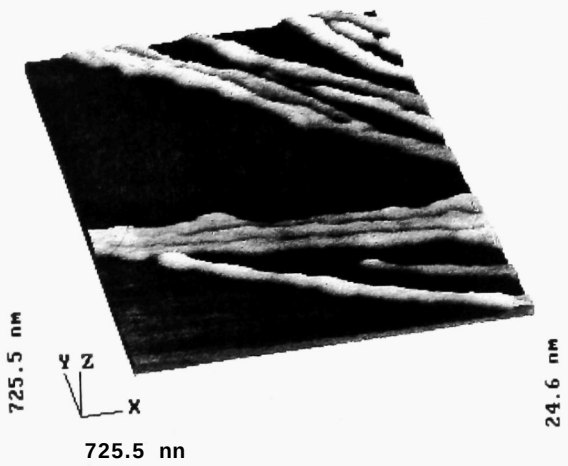


Figure 3.12 725.5 nm x 725.5 nm AFM image of a spray deposited PEO sample showing a fibrillar morphology. Grey-scale view, nominal force 1.268 nN.

(a)

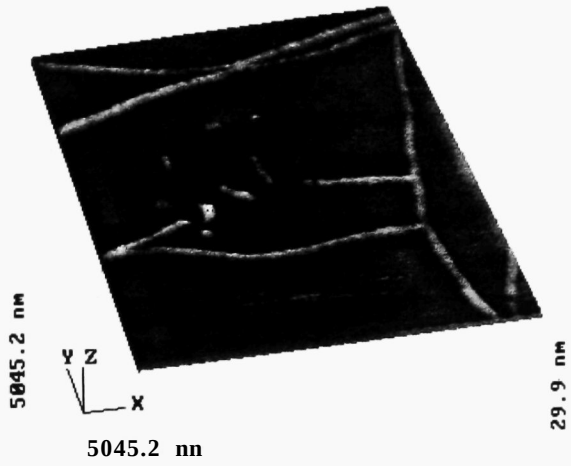


(b)

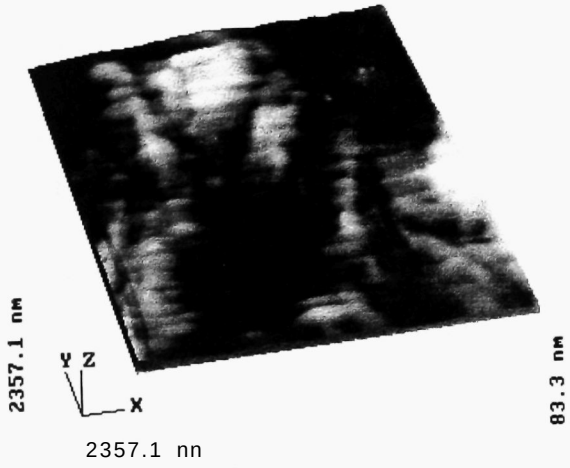


Figure 3.13 (a) Destmction of a PEO fibre due to AFM imaging. 5045.2 x 5045.2 nm AFM image, grey-scale view, nominal force 0.07 nN.

(b) Damaging a spherulitic morphology by repeated imaging at high force. 2357.1 nm x 2357.1 nm AFM image, grey-scale view, loop gain 0.595, nominal force 10 nN, scan frequency 3 hZ.

morphology. The destmction appears as a series of lines running in the direction of scanning of the AFM probe. These lines were observed only when the imaging force was increased to 10 nN and 30 consecutive images of the area were recorded.

## 3.4 Conclusions

The work described in this Chapter has demonstrated that the AFM has a promising role in the characterization of polymeric biomaterials. The first study demonsti-ated that the AFM could characterize the organization of PEO within sphemlites at many different length scales ranging for lamellae organization at the nanometric scale to the distribution of complete sphemlites on the micron scale.

In comparison with SEM studies the AFM allowed the samples to be analyzed without exposure to a vacuum or surface coating prior to imaging. The resolution achieved matched the highest achievable by SEM and the vertical contrast generated by the AFM on the lameUae ribbons aUowed these stmctures to be resolved without the use of surface etching to remove amorphous material.

The high resolution and vertical contrast of the AFM data was then harnessed to study the effect of varying sample preparation parameters on the PEO surface morphology. These studies demonstrated that the polymer morphology could be controlled by changing the PEO solution concentration, the temperature of film formation and the method of depositing the polymer solution on the substrate.

Finally, two adverse interactions between the AFM probe and PEO samples were reported. These interactions both resulted from the pressure of the probe changing the topography of the underlying polymer. It is important to be aware of these interactions and they become increasingly important in the next Chapter where dynamic processes are visuaUzed with the AFM and the chance of probe induced damage is increased.

The results in this Chapter indicate that the AFM should be considered as a complement to conventional SEM and light microscopy rather than a replacement. The instmment is ideal for analysing samples with very low

surface roughness because high vertical resolution generates contrast from features such as single molecules and lameUae ribbons which are not resolved by SEM or light microscopy. However, the depth of field of the AFM is very limited in comparison with the SEM. This limitation is imposed by the maximum degree of movement of the piezoceramic in the z direction. This movement is approximately 12 |im for the 150 μm scanner and 1 μm for the tube scanners.

The major benefits of utiUzing AFM analysis in the study of polymeric biomaterials lie in the abiUty to image surfaces within aqueous environments. This allows the surface morphology to be visualized in conditions similar to those experienced within a living systems. The next Chapter, describes the application of AFM imaging within a liquid environment. The work relies on the imaging techniques developed in the present Chapter and describe how the AFM can record dynamic changes in surface morphology resulting from polymer/water interface events.

# Chapter 4

# Imaging Polymer Surface Degradation by *In Situ* Atomic Force Microscopy

## 4.1 Introduction

In 1989, Hansma *et al* (45) demonstrated that the AFM could be used to visuaUze changes occurring to surfaces within liquid environments (see section 1.4.2). This demonstration represented a major advantage in the microscopy of biological and biomedical materials because it became possible to image complex interfacial processes within aqueous environments. Therefore, for the first time, biological processes, such as the transcription of DNA (156) and the adsorption of proteins to surfaces (157), could be visualized.

The work described in this Chapter has aimed to exploit the abiUty of the AFM to image interfacial processes with a view to advancing the study of polymeric biomaterials. This work became possible with the arrival of the Topometrix Explorer AFM (see section 2.1.1), which was the first AFM in the Laboratory to aUow the imaging of samples within a liquid environment

The application of *in situ* AFM could advance many areas biomaterial characterization because it would allow dynamic changes occurring at complex solid-liquid interfaces to be visualized. The present work has concentrated on one such area, the use of surface eroding biodegradable polymers in controlled dmg delivery systems (see next section). This area has been chosen to demonstrate *in situ* AFM because of the importance of surface morphology to the kinetics of polymer erosion and, in tum, the kinetics of dmg release.

### 4.1.1 Controlled Drug Delivery Using Biodegradable Polymers

For a dmg to achieve its therapeutic aim it much reach target receptors at a sufficient concentration to change some aspect of physiological activity. Most dmgs act at receptors within the body and the most convenient method of delivery is to use the patients blood system to distribute the drug to these receptors. Therefore, the role of dmg delivery devices for these dmgs has concentrated on getting the dmg into the blood system either through absorption (eg. tablets/capsules) or directiy via an injection.

There are a number of disadvantages of using these "traditional" delivery devices . Examples of these disadvantages are given in Table 4.1 and references 14, 158 and 159. For many dmgs the problems of side-effects, first pass metabolism and poor distribution are negligible and the traditional delivery devices offer an efficient and cost-effective method of administration. However, there are other dmgs that could be clinically useful, if delivered to their target receptors, but which cannot be delivered via traditional devices due to side-effect profiles, rapid metabolism or one of the another of the disadvantages in Table 4.1. For these dmgs controlled dmg delivery offers the potential to provide valuable therapies for currentiy incurable disease states.

The field of controlled dmg delivery research has diversified to provide many new strategies with which to deliver dmgs (14). Examples of the many strategies of this area are given in Table 4.2 along with some of the advantages of each strategy.

The surface-eroding biodegradable polymer devices have proven successful in the delivery of anti-tumour dmgs (169), contraceptive steroids (171) and protein/peptide based dmgs (170). The schematic diagram in Figure 4.1 demonstrates the mechanism of action of these delivery systems. The dmg is dispersed within a matrix of the biodegradable polymer and tiiis matrix is then introduced into the patient Within the aqueous environment of the body, the pure dmg would normally be able to dissolve and hence become available for therapeutic action, however, this dissolution is prevented by the

| Disadvantages of Traditional Drug Delivery Devices |
| --- |
| Interaction with non-target sites generates side-effects |
| Rapidly metabolised dmgs (eg proteins) require frequent dosing |
| First pass metabolism of dmgs deUvered oraUy |
| Poor distribution to areas of body with limited blood supply or dense capUlary walls |
| Stress and cost of repeated injections |
| Unpredicatble dmg absorption due to influence of food in gastro-intestinal ti-act |

Table 4.1 Examples of the disadvantages of "traditional" deUvery sytems.

| Controlled Drug Delivery Stragety | Clinical Advantage | Refer-ence |
|---|---|---|
| Tablet coating | Sustained release in GIT<br>Specific deUvery to tiie colon | 160<br>161 |
| Hydrogel | Sustained release | 162 |
| Vesicles (microparticles and liposomes) | Targeting to specific sites | 163 |
| Transdermal Patches | Avoidance of first pass metabolism<br>Pulsatile delivery of proteins from ultrasonic devices | 164<br>165 |
| ChemicaUy attached targetting group | LocaUzed effect of anti-tumour and other dmgs with hazordous side-effect profiles dmgs | 166 |
| Pro-dmg | Enhanced GIT absorption | 167 |
| Osmotic devices | Sustained/pulsatile release | 168 |
| Surface eroding biodegradable polymers | Sustained release<br>Protection of rapidly metaboUsed dmgs | 169<br>170 |

Table 4.2 Examples of controUed dmg delivery strategies.

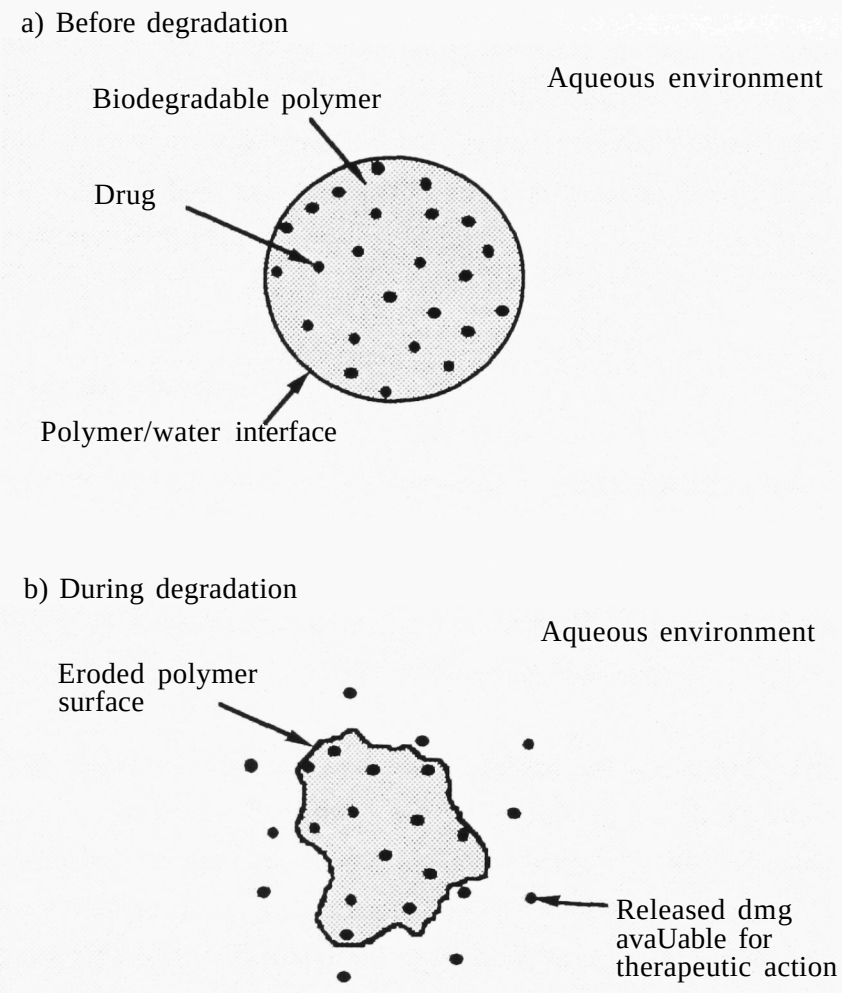


Figure 4.1 Schematic diagram of the mechanism of action of surface eroding biodegradable polymer devices.

hydrophobic polymeric material. The release of dmg from these devices can occur only as a result of the hydrolysis of the polymer at the interface with the biological system. Therefore, the release of the drug, and hence its therapeutic activity, is directiy linked to the surface erosion of the polymer. Clearly, the most important parameter in the kinetics of dmg release from these systems is the degradation of the polymer at the polymer/water interface (135) and the development of a technique to directiy visuaUze this degradation would advance the characterization of such biodegradable systems. Examples of polymers used in such devices include polyesters (172-174), poly(ortho esters) (171) and polyanhydrides (175, 176).

### 4.1.2 Polyanhydrides

The polyanhydrides are a class of biodegradable polymers designed specificaUy for biomedical applications which are receiving considerable attention due to their predictable erosion (176). The general stmcture of a polyanhydride is shown in Figure 4.2 with some commonly employed backbone stmctures. The mode of hydrolysis of polyanhydrides is shown in Figure 4.3 .

The hydrolytic reactivity of the anhydride linkage is high, allowing biodegradation to be achieved with a wide variety of backbone structures. Surface erosion occurs due to the hydrophobicity of the polyanhydride backbone which results in water penetration into the bulk being rate-limiting. The factors affecting polyanhydride hydrolysis have been discussed in the literature (177).

The success of backbone chemical modifications has yielded polymeric devices which release dmg molecules *in vivo* over periods ranging from days to months. However, recentiy there has been an increased awareness that in designing novel biodegradable systems it is important to understand not only the effect of chemical composition on degradation kinetics, but also the morphology and molecular organization of the polymeric material (129 and 135).

**General Structure**

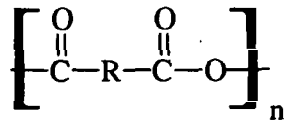

**Backbone Structures (R)**

$(CH_2)_3$

Poly(sebacic anhydride) (PSA)

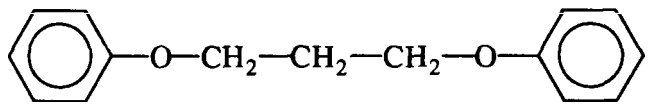

Poly( 1,3-bis(*p*-carboxyphenoxy)propane)(CPP)

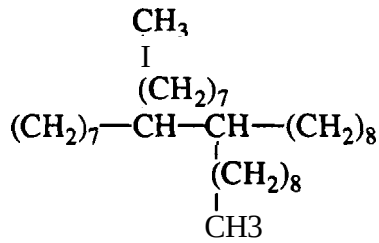


Poly(Fatty Acid Dimer) (p(FAD))

Figure 4.2 The general structure of polyanhydrides with some commonly employed backbone structures.

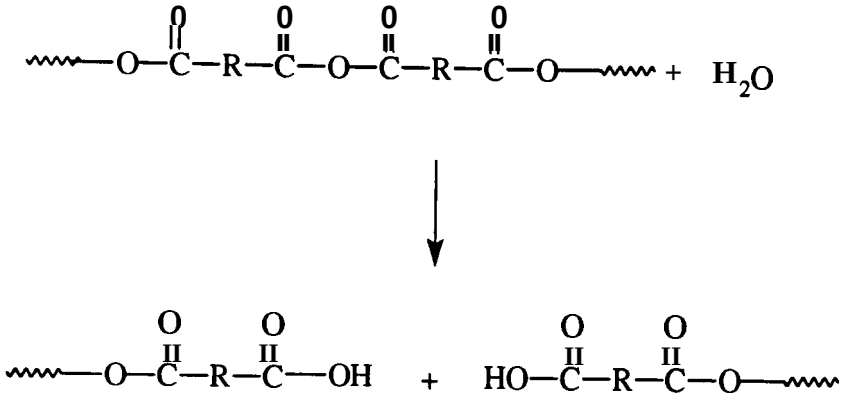

**Figure 4.3** **Mode of hydrolysis of polyanhydrides.**

The influence of polymer morphology and molecular organization on the biodegradation of polyanhydride devices has been studied by a number of techniques including X-ray powder diffraction (135), differential scanning calorimetry (DSC) (135), SEM and optical microscopy (129,135). For poly(sebacic anhydride) (PSA) devices, these studies have revealed the semi-crystalline nature of the material. X-ray powder diffraction has recorded the crystallite dimensions and DSC has provided quantitative data on the proportions of crystaUine and amorphous regions within semi-crystalline morphologies produced by both solvent and melt casting methods.

SEM and optical microscopy have provided visual data on the semi-crystalUne morphologies of PSA (129 and 135). With cross-polarized light microscopy the presence of Maltese cross pattems in thin films of PSA confirms the presence of sphemUtes and the radiating fibrous stmcture of these sphemlites has been observed using SEM. Upon degradation of these devices there is a loss of amorphous material between the fibres of the sphemlites which is manifested in the electron micrographs by the observation of the dendritic skeleton. The preferential loss of amorphous material in the initial stages of PSA hydrolysis is attributed to the higher permeability of amorphous material over crystalline material.

The first aim of the *in situ* AFM characterization of polymer degradation has been to visualize this preferential loss of amorphous material from PSA sphemlites. The reproduction of a pattem of degradation from an extensively characterized system, such as a PSA sphemlite, has been chosen as the first example because this allows direct comparison with the established SEM technique of recording surface morphology changes during degradation. The work is described in the Results and Discussion section 4.2.1.1.

Having demonstrated that the *in situ* AFM technique can visualize preferential etching of PSA in drop cast fdms with clearly defined sphemUtes, the work described in section 4.2.1.2 explores how the methods can be extended to study the erosion of fundamentally more complex PSA morphologies produced by melt casting. The pH dependency of the degradation of the PSA surface is also demonstrated. This provides the first example of the use of *in situ* AFM to investigate the kinetics of surface erosion, a subject which is further explored in Chapters 5 and 6. FinaUy, in this Chapter the abiUty of the

AFM to record dynamic changes to biodegradable fdms is utiUzed to investigate tiie influence of phase morphology on the erosion of a number of blends of polymers. The use of biodegradable blends in controlled dmg deUvery is briefly reviewed below.

### 4.1.3 Biodegradable Polymer Blends Incorporating Polyanhydrides

In the design of new polymeric materials it is an attractive strategy to combine two or more existing polymers to form a blend (178). IdeaUy, the blend will possess the desirable properties of each of the constituents. This strategy has been particularly successful in the production of toughened polymers in which a brittie polymer (eg. high impact polystyrene) is mixed with a ductile polymer (eg. poly(2,6-dimethyl-l,4-phenylene oxide)) to give a blend which combines the high modulus of the brittie polymer with the shear yielding ability of the ductile polymer (179).

Considerable success has been achieved with surface eroding delivery systems using matrices containing a single component polymer as described in the previous section. However, these single component systems can generate an inflexible delivery system, because there are only a limited number of strategies with which to change the kinetics of dmg release. These strategies include changing the shape of the delivery system and hence the polymer surface area, or synthesising a new polymer with a different backbone stmcture (13). A much more flexible drug delivery device can be designed if two biodegradable polymers, with very different degradation rates, form the matrix. It may then be possible to vary the kinetics of surface degradation by changing the relative amounts of each polymer in the blend (180).

The concept of controUing degradation rates by varying polymer blend composition is complicated by the immiscibility of most pairs of polymers (178). This immiscibiUty arises from the low entropy increase resulting from mixing long polymer chains with each other. As a consequence of this, the Gibbs free energy change of mixing is generally positive favouring polymer phase separation. When phase separation occurs, the degradation kinetics of the matiix wiU be highly influenced by the morphology of the two phase system.

Therefore, there is a requirement when designing polymer blend matrices to characterize the phase morphology in order to understand the degradation profile of the resulting devices.

This phase morphology characterization has been performed by a number of different microscopy techniques (181,182). SEM has been employed to study fracture (183) and thin film (184) surfaces of polymer blends. These studies require the fracture surface to be coated with a thin metalUc fihn and it is generally difficult to identify the different phases. One approach to achieve differentiation is to remove one of the phases by solvent extraction (183). This has been applied to study, for example, the mixing of hydroxyl-functionalized polystyrene and poly(ethyl acetate) (183). Transmission electron microscopy (TEM) has proved valuable in the study of thin sections of blends (181). Again, there is a problem in differentiating the polymer phases. This can be overcome, for some polymers, by preferentially staining one of the polymer phases using an electron dense dye (185). There have also been promising studies performed using laser confocal fluorescence microscopy on poly(methyl methacrylate) (PMMA) and PS blends (186). The PMMA component of the blend was labelled with a fluorescent dye which enabled the phase morphology to be visuaUzed at the surface and to depths of 6 μm.

In section 4.2.3, work is described which provides a new method of characterization polymer phase morphology using the *in situ* AFM developed with the PSA system. The visualization of the erosion of blends of PSA and poly(DL-lactic acid) (PLA, see Figure 4.4) has been performed. This work provides an unique insight into the influence of blend composition on both the initial surface morphology of the blend film and on the change in film stmcture during erosion in alkaline conditions.

## 4.2 Experimental Methods

### 4.2.1 Polymer Materials

PSA, $M_w$ 25k, was synthesised by polycondensation by the group led by Dr Avi Domb at tiie School of Pharmacy, The Hebrew University, Jemsalem, Israel. The experimental method of the polymerization and the methods of

purification are described in the literature (187). PLA in the DL fonn, $M_w$ 50k, was used as purchased (Polysciences, Inc., Warrington, U.K.).

### 4.2.2 Sample Preparation

Drop cast films of PSA were prepared by spin casting a 10 µl aliquot of 1 mg/ml PSA in chloroform onto 1 cm x 1 cm freshly cleaved mica substrates. Samples were dried in air for 1 hour prior to analysis.

Melt crystalUzed fdms were prepared by melting the polymer at 86 °C and then cooUng slowly over a predetermined time period. The cooling time is noted at the relevant part of the Results and Discussion section.

Polymer blend films were prepared as for the pure PSA drop cast samples but using chloroform solutions containing PSA and PLA. The total polymer concentration in the chloroform was 1 mg/ml, witii individual polymer proportions varied as required.

### 4.2.3 Atomic Force Microscopy

The basic procedure for acquiring AFM images was identical to that described in Chapter 2 for the Topometrix Explorer. However, imaging had to be performed within an aqueous liquid environment which required the use of the Explorer liquid cell. This consists of metalUc holder with raised edges. The sample was positioned within the boundary of the edges and then liquid was dropped into the holder until the sample was completely immersed. The AFM head was then brought down onto the sample as normal. InitiaUy, all samples were imaged within a pH 7 water environment to allow characterization of the morphology before degradation. Then, the AFM head was raised to allow the water to be removed and a buffer solution, at a predetermined pH, was dropped into the holder to immerse the sample. The time at which the buffer came into contact with the sample was taken as t = 0 min.

For all the degradation studies on poly(sebacic anhydride) described in this thesis an alkaline buffer was employed. Under alkaUne conditions the hydrolysis of the anhydride bond is accelerated aUowing experiments to be performed within a short period of time (ranging from minutes to hours). These

accelerated degradation times enabled the experimental procedures to optimized and repeated. The composition of the buffer used is noted in the relevant parts of the Results and Discussion section.

All the AFM data in this Chapter is displayed as two-dimensional representations in shaded view. The use of two-dimensional representations allows all the images from one degradation experiment to be displayed on one page assisting the comparision of consecutive images. On a number of images ti-ansient resonances in the piezoscanner at the start of each line have created noise which is detected as a series of lines mnning perpendicular to the scan direction. This noise was eUminated in later studies by employing a new scanner. The noise does not affect the areas of the images highlighted for discussion.

## 4.3 Results and Discussion

### 4.3.1 Poly(sebacic anhydride) Films

#### 4.3.1.1 Drop Cast Films

The semi-crystalline nature of PSA generated tiie expected two-dimensionally constrained sphemlites when samples were produced by drop casting a 10 mg/ml solution onto a mica substrate. The AFM image in Figure 4.5 shows an example of a PSA sphemlite and the characteristic nucleating centre and radiating fibres can be identified.

The aim of using the AFM *in situ* during the degradation of the PSA sample was to visualize changes in the surface stmcture resulting from the degradation process. Given the potential for the AFM image acquisition procedure to generate changes in the surface morphology of samples due to the scanning motion of the AFM probe (see section 3.3.3), it was clearly important to ensure that an area of the sample could be repeatedly imaged without the induction of surface damage. This was demonstrated by a 5 day experiment in which a PSA surface was imaged in a pH 7 aqueous environment During this period AFM images were recorded initially every 30 minutes and then at 6 hourly intervals. At pH 7, the degradation rate of these densely packed surfaces

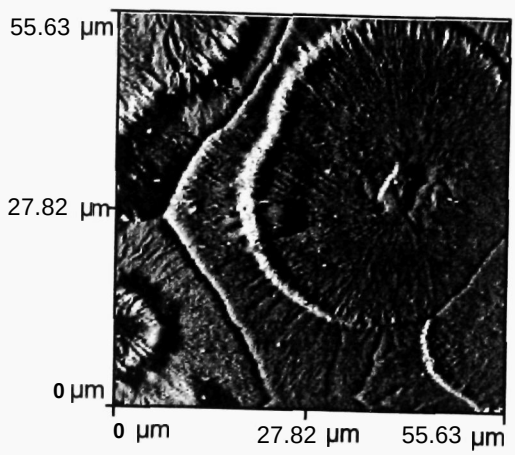


Figure 4.5 55.63 µm x 55.63 µm AFM image showing a sphemlite at the surface of a drop cast PSA film. P = 0.6, I = 0.2, D = 0.1. Scan frequency 6 Hz.

Having shown tiiat repeated scanning of PSA did not change the surface topography, degradation of the polymer was initiated by displacing the pH 7 water in the imaging chamber with 0.05M pH 9 tris(hydroxymethyl) aminoraethane buffer. Figure 4.6 displays a series of AFM images showing the surface erosion of a section of sphemlite on a PSA film. In general, the series of images in Figure 4.6 show the initial stages of exposure of the fibrous components of the sphemlites at the surface. This effect can be clearly seen if we consider the exposure of the forked fibre (marked A) which can be observed in its entirety in Figure 4.6d after 11 minutes in contact with buffer. On the 5 minute image, this area contained three short and independent fibres. There was then an apparent lengthening of the fibres at the surface as the amorphous material between these fibres was preferentially degraded. Considering the right hand fibril of the fork, the length revealed at the surface increased from approximately 3.0 μm at 5 minutes, to 5.5 μm at 6 minutes and to 8.2 μm at 7 minute at which point the continuity of the fork could be observed. Furthermore, there was an increase of the height of the fibre at the surface from about 350 nm at 5 minutes to 700 nm at 11 minutes.

The erosion of PSA surfaces over longer periods unveiled sub-surface morphology from within the bulk polymer. An example is shown in Figure 4.7 of the surface degradation of a PSA fihn over a period of 19 hours in the 0.05M pH 9 tris(hydroxymethyl) aminomethane buffer. Figure 4.7a reveals two banded sphemlites near the centre of the scan. In the surrounding areas, there are no distinct sphemUtic stmctures at the surface. FoUowing exposure to the pH 9 tris(hydroxymethyl) aminomethane buffer for 19 hours, there was a clear surface morphological change. In Figure 4.7b the original banded sphemlites can still be observed but there is clear evidence that the degradation process caused an etching of the polymer surface. For example, the sphemlitic nucleating centre was exposed at position B. This nucleating centre appears as an indentation in the surface in the original scan, but after 19 hours of degradation it lies approximately 200 nm above the average height of the sphemlite. Another morphological change observed after 19 hours was the appearance of the banded sphemlite at position C. This spherulite was previously covered by amorphous material which had been preferentially degraded.

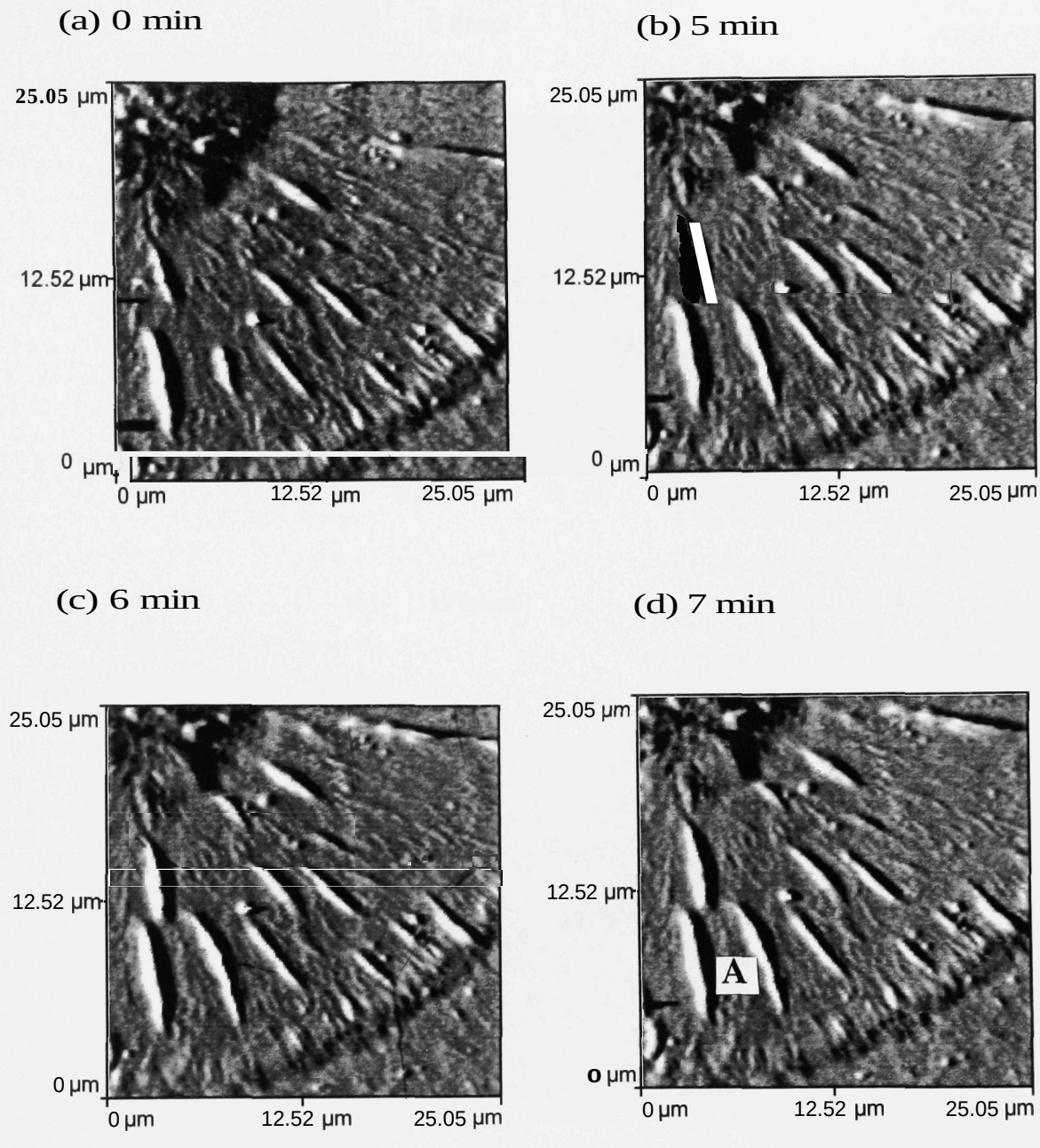


Figure 4.6 The initial erosion of a PSA sphemlite after exposure to a 0.05M pH 9 tiis(hydroxymethyl) aminomethane buffer visuaUzed on 20 µm x 20 |im AFM images. P = 0.6, I = 0.2, D = 0.1. Scan frequency 20 Hz.

(a) 0 hours

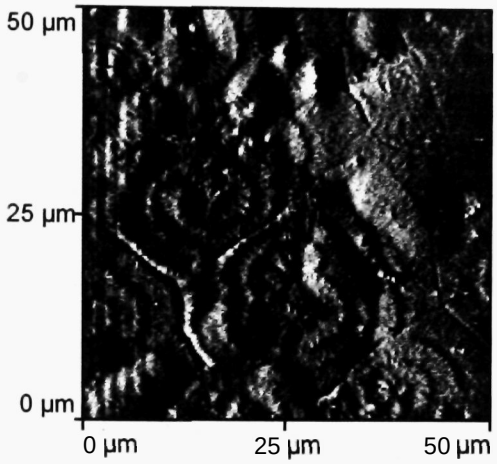


(b) 19 hours

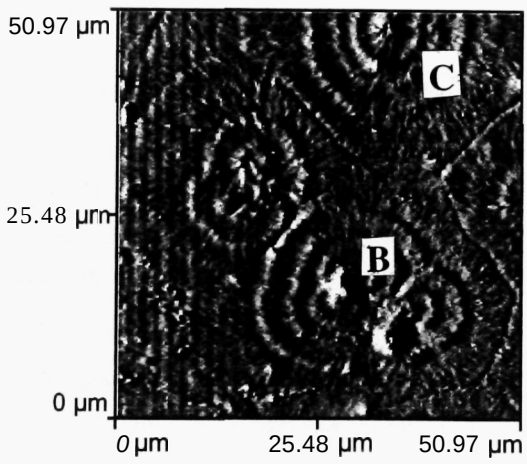


Figure 4.7 Long-term changes in the surface morphology of a drop cast PSA film on exposure to 0.05M pH 9 tris(hydroxymethyl) aminomethane buffer. 50 µm x 50 µm AFM images. P = 0.45, I = 0.1, D = 0.1. Scan frequency 10 Hz.

#### 4.3.1.2 Melt Crystallized Samples

Surface characterization of the melt crystaUized PSA revealed a fibrous morphology typical of a semi-crystalline polymer. The 75 μm x 75 μm AFM image in Figure 4.8 is an example of an area of a melt crystalUzed sample on which a sphemUte could be observed. In general, the surface morphology of these samples was less organized than that of the drop cast films. Most areas imaged did not contain sphemlites but rather were composed of interwoven network of PSA fibres. On some areas the surface had a smooth texture indicative of amorphous polymeric material.

An important sample preparation factor in determining the morphology was the cooling rate during soUdification. If during the cooUng of the PSA melt the oven temperature was held at 70 °C (10 °C above the glass transition temperature Tg) for 10 minutes, the proportion of fibres at the surface increased and often sphemUtic stmctures could be observed. By increasing the rate of cooling during solidification it was possible to inhibit the formation of spheruUtes in the PSA samples. The surface morphology for these samples consisted of a granular texture.

Four 20 μm x 20 μm AFM images are shown in Figure 4.9, which demonstrate the change in PSA surface morphology occurring due to degradation following the exposure of a surface to the pH 12.5 KCl/NaOH buffer solution. This sample was prepared with a 10 minute delay period at 70 °C. The data clearly demonstrates an etching of the surface due to the preferential loss of the amorphous PSA material. This resulted in the exposure of fibrous, crystalline material. After 20 minutes of exposure to tiie alkaUne solution a number of elongated indentations could be observed on the surface due to the loss of amorphous material between fibres. These indentations became wider and deeper as the exposure time increased.

The pH dependence of the hydrolysis of the polyanhydride has been demonstrated by other techniques (129,135) and was an important goal in the analysis using *in situ* atomic force microscopy. The series of 50 μm x 50 μm AFM images shown in Figure 4.10 were recorded during a degradation experiment performed in a pH 11.5 KCl/NaOH buffer, using a sample prepared in a similar manner to that imaged in Figure 4.9. A similar pattern of

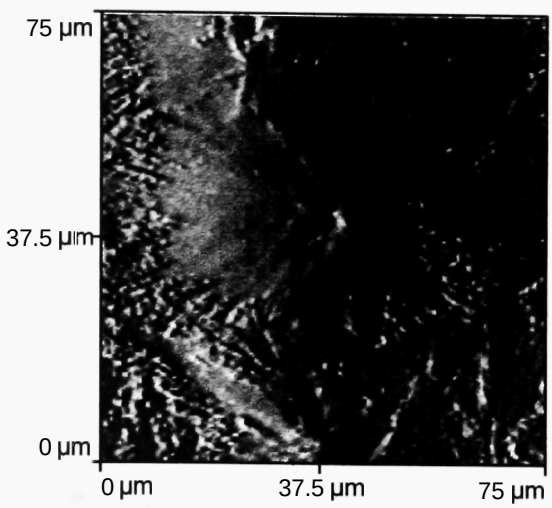


Figure 4.8 75 µm x 75 µm AFM image showing a sphemUte at the surface of a meU crystalUzed PSA sample. P = 0.15, 1 = 0.05, D = 0.05. Scan frequency 5 Hz.

(a) 0 min

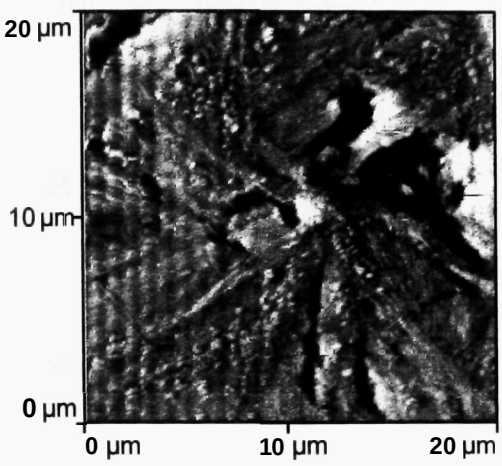


(b) 20 min

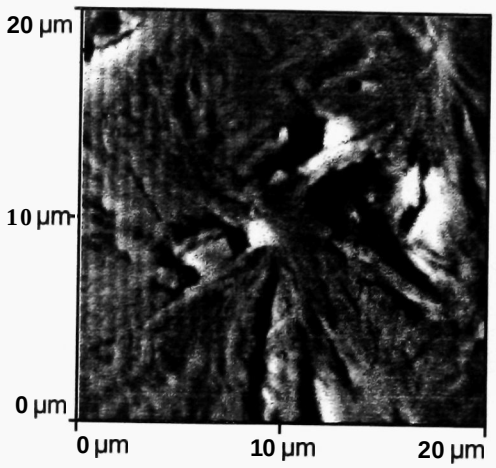


(c) 40 min

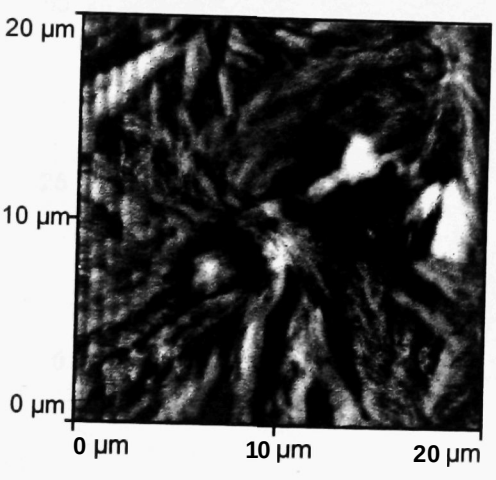


(d) 60 min

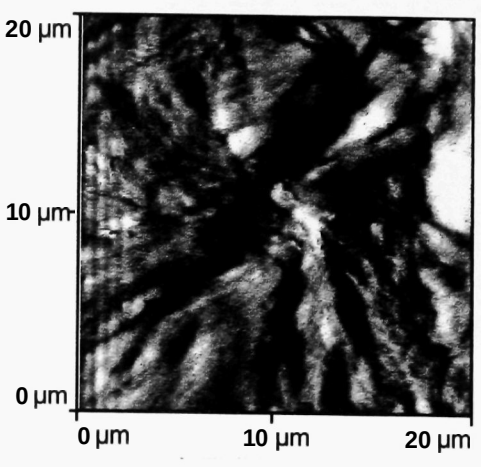


Figure 4.9 Four 20 µm x 20 µm AFM images visualizing the change in surface morphology on exposure to a pH 12.5 buffer solution. P = 0.05, I = 0.05, D = 0.05.

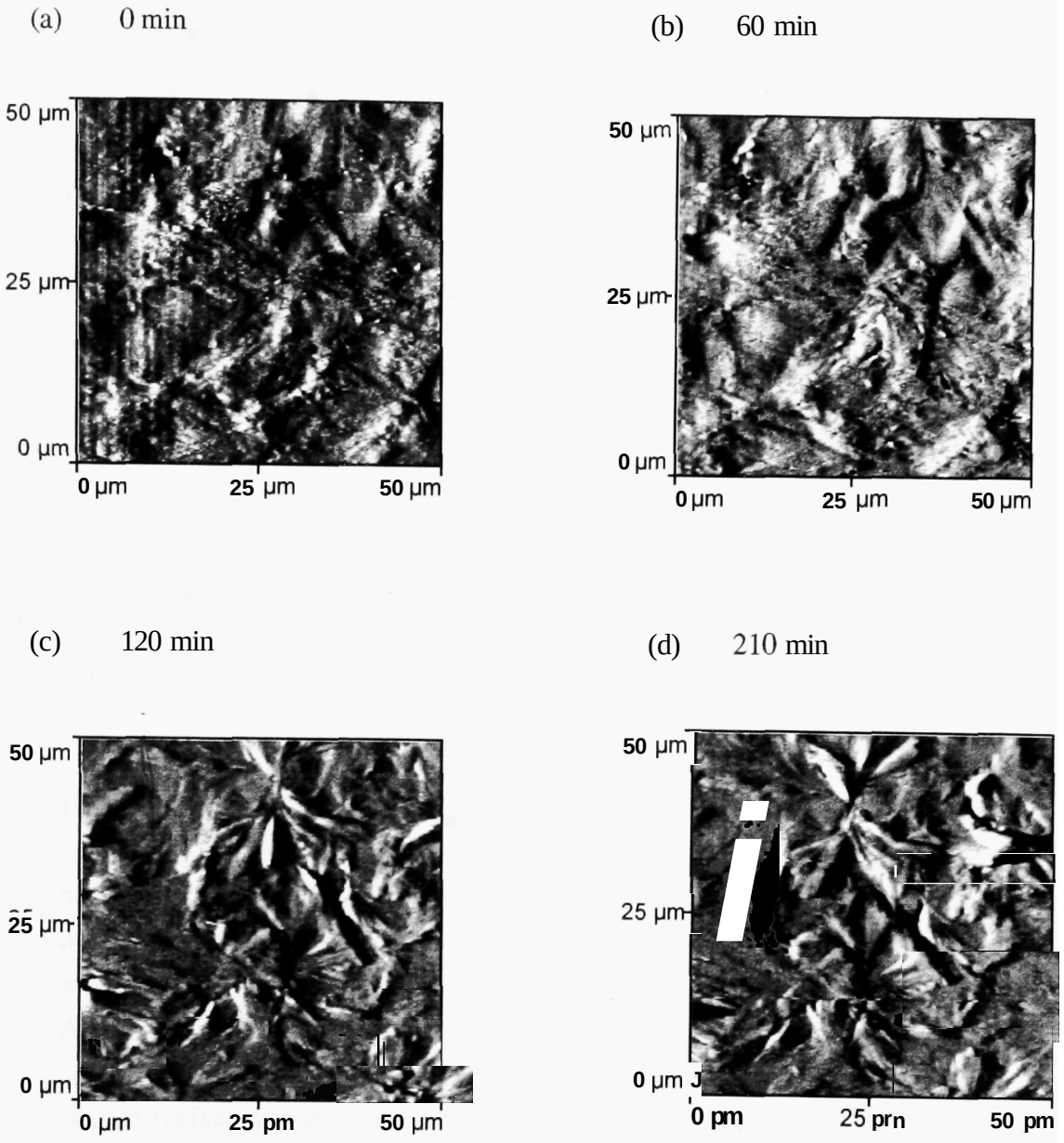


Figure 4.10 Degradation of a melt-crystallized PSA film in a pH 11.5 buffer shown on four 50 µm x 50 µm AFM images. P = 0.15, 1 = 0.05, D = 0.05.

degradation was observed in this data as seen at pH 12.5. However, the kinetics of the degradation are, as expected, considerably slowed. Hence, the clear appearance of fibrous material at the surface due to preferential loss of amorphous PSA was noticeable over a period of 2 to 3.5 hours at the lower pH.

These experiments have also shown that sample preparation and its influence on surface crystallinity have an effect on surface degradation. The AFM images in Figure 4.11 show a degradation experiment performed at pH 12.5 on a sample cooled rapidly during solidification. Initially, the surface displayed no sphemlitic or fibrous morphology. However, the AFM images recorded after 20 min and 90 min contact with the alkaline solution demonstrate the exposure of subsurface crystaUine material. It appears, therefore, that the surfaces of these PSA melt crystallized samples possessed more amorphous material at the surface. The rapid soUdification of the sample prevented the formation of sphemlites at the surface.

In the development of new appUcations of scanning probe microscopes, data validation is essential due to the close relationship between the sample surface and the scanning probe when the AFM is operated in contact mode. As stated above, before performing degradation it was ensured the imaging process did not dismpt the PSA surface by imaging for 5 days in a pH 7 environment. However, during the degradation experiments, the hydrolytic process could change the mechanical properties of the PSA surface and, dierefore, it was necessary to develop a method of self-validation which could be performed during the experiment. For this purpose, during all degradation experiments a protocol was adopted by which following the acquisition of a 20 μm x 20 μm AFM image, a 50 μm x 50 μm AFM image was recorded. This large scan contained the smaller scan area. Now, if the action of probe scanning the sample surface accelerated the degradation process, the central 20 μm x 20 μm area of the 50 μm x 50 μm image would display a larger morphological change than the surrounding area, due to the larger extent of interaction with the AFM probe during previous scans. Similarly if the probe inhibited degradation, the central region would display less morphological change. The series of 50 μm x 50 μm AFM images in Figure 4.12 were taken after the data shown in Figure 4.9 during a degradation at pH 12.5. From this data it can be observed that the central 20 μm x 20 μm area of these images had undergone similar degrees of morphological changes to tiieir corresponding surrounding regions.

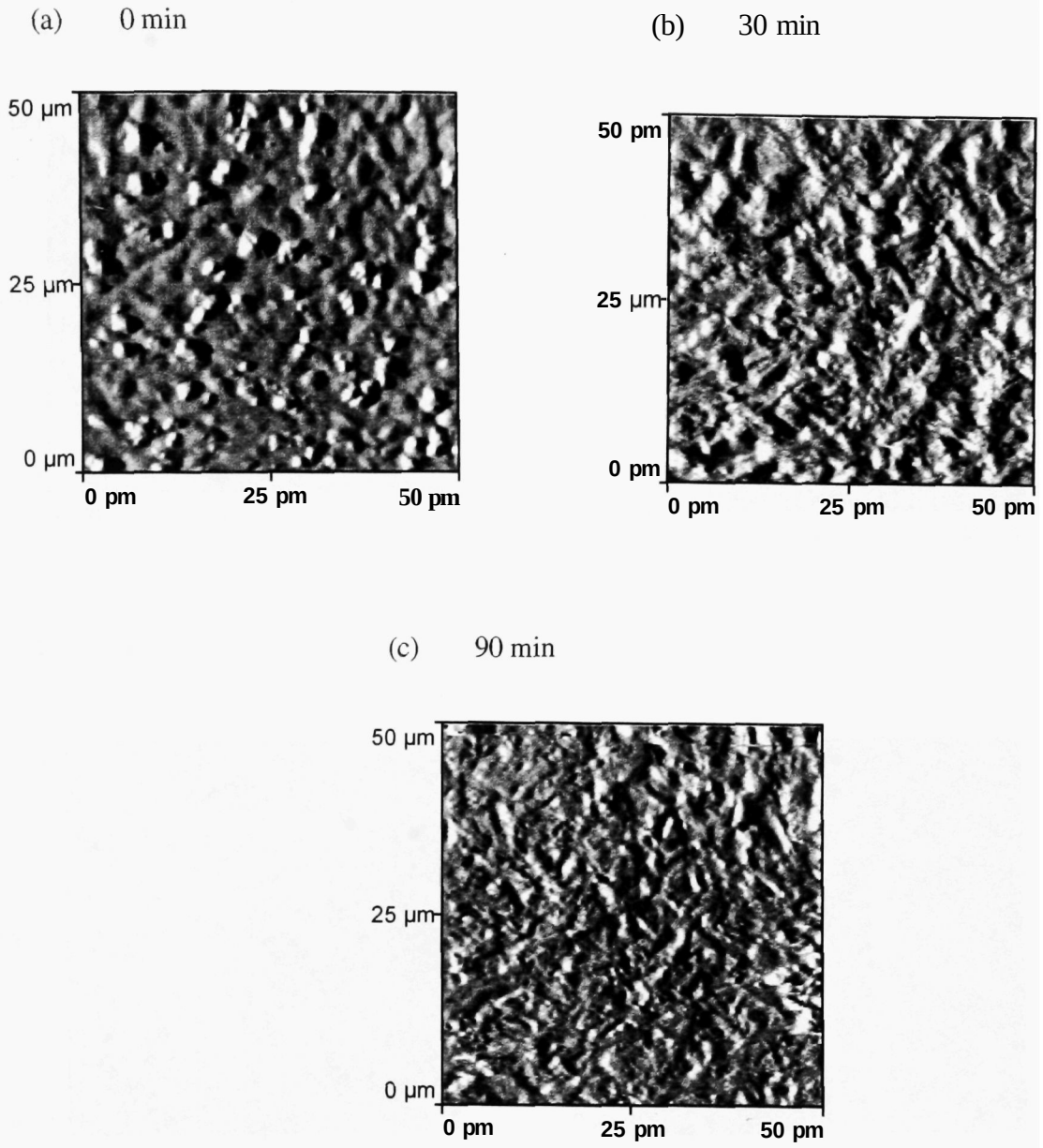


Figure 4.11 50 µm x 50 µm AFM images of the degradation at pH 12.5 of a PSA melt crystallized film prepared with a rapid cooling procedure. P = 0.45, I = 0.1, D = 0.1.

(a) 0 min

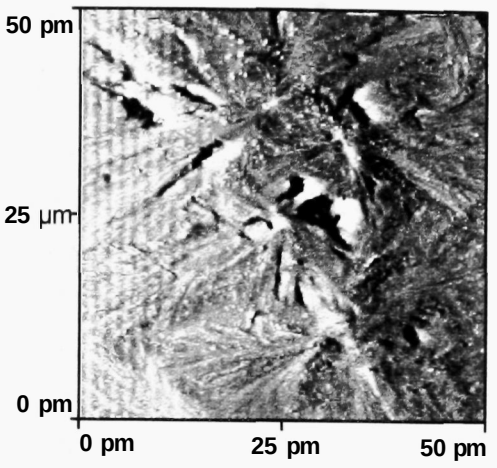


(b) 21 min

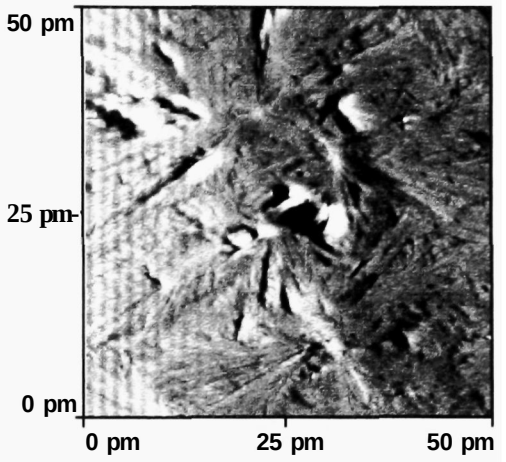


**(c)** 41 min

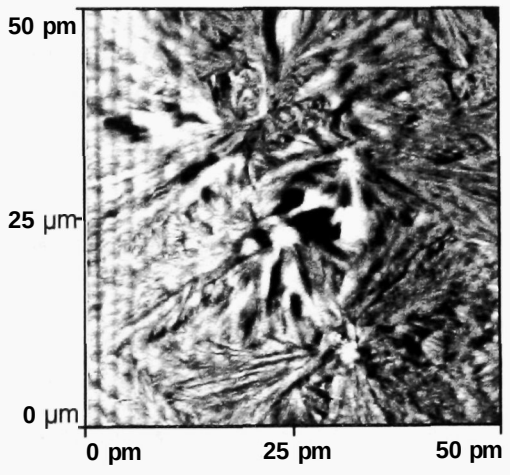


(d) 61 min

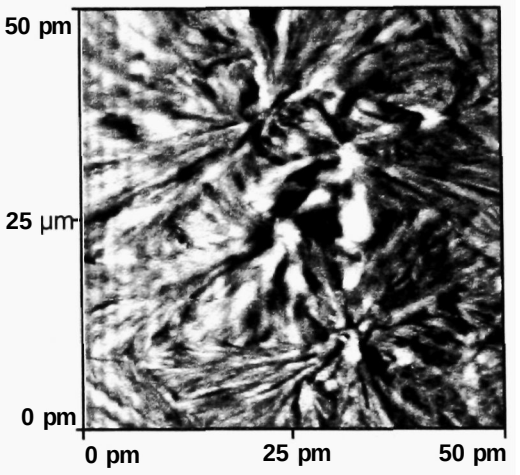


Figure 4.12 50 µm x 50 µm vaUdation AFM images recorded immediatiey after the 20 µm x 20 µm AFM images in Figure 4.9. P = 0.05, I = 0.05, D = 0.05.

Therefore, it is concluded tiiat over the time-scale of these experiments the AFM probe did not influence the surface morphology at the micron-scale level.

The visuaUzation of diese PSA samples provide the first examples of the use of the AFM to study the surface erosion of a biodegradable polymer. To consider the potential benefit of the technique to controlled release research it is worth comparing the type of data obtained witii tiie data recorded with an SEM by Mathiowitz *et al* on similar PSA samples (129). In the SEM studies, the loss of amorphous polymer from around the crystalUne fibres was observed by comparing different sample areas before and after exposure to the aqueous environment. The results demonstrated a very clear exposure of the sphemlitic fibres, however, tiie samples had to be dried and exposed to the vacuum widiin the gold coater prior to imaging. The advantage of the *in situ* AFM method Ues in the ability to repeatedly record changes occuring to just one area of the sample surface during erosion. For weU-defined surface morphologies such as PSA sphemUtes, the SEM is well suited but we believe the AFM technique is preferable for complex systems where the interpretation of surface morphology changes is assisted by observing the evolution of surface changes.

In the next section, a complex biodegradable blend system is characterized during erosion to demonstrate the suitability of the *in situ* AFM methods over SEM for certain sample types.

### 4.3.2 Biodegradable Polymer Blends

The thin fihns of PSA and PLA and the blends containing differing proportions of these two polymers displayed distinct surface morphologies when analyzed with the AFM. As recorded in section 4.3.1.1 the film produced from the PSA solution possessed sphemlites at the surface the fibres. The surface topography of the single component PLA films was found to be relatively smooth and lacking in the sphemUtic stmctures. In Figure 4.13, the surface topography of a 10 μm X 10 μm area of a PLA film is shown. This image showed a smooth film stmcture dismpted only by occasional aggregates. This type of surface morphology is typical of a low crystallinity polymer sample prepared by spin casting.

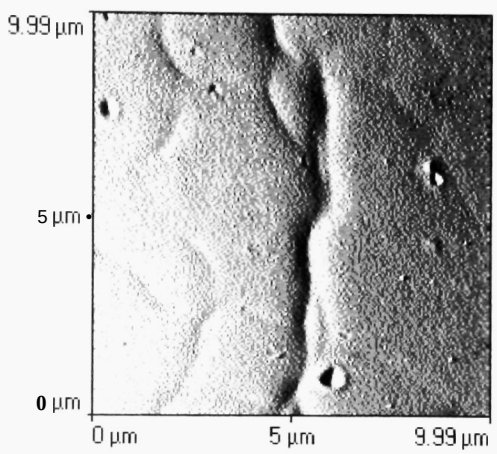


Figure 4.13 10 µm x 10 µm AFM image of the surface of a PLA sample. P = 0.05, I = 0.03, D = 0.05.

For the polymer blend containing 70% PSA: 30% PLA, the surface was observed to consist of a granular morphology (Figure 4.14a). The granules had diameters ranging from 200 nm to 1 μm and protmded from the other surface material by 10 to 50 nm. Between the granules, the polymer fdm appeared to be continuous. When the polymer blend composition was changed to 50% PSA: 50% PLA, the AFM recorded topography changed to show a gentiy pitted surface. This surface morphology can be observed in the AFM topograph in Figure 4.14b . The pits had a broad and shaUow structure with typical diameters ranging from 400 nm to 2 μm and depths of 20 to 60 nm.

A pitted surface morphology was also observed for the film of the 30% PSA:70% PLA blend (Figure 4.14c). However, the AFM images showed the pits to be smaller in diameter than tiie 50% PSA:50% PLA blend film. The diameter of tiiese pits was found to be between 200 and 800 nm with depths of between 20 to 50 nm.

For all the polymer blends studied it was evident that the presence of PLA had inhibited the formation of identifiable fibrous stmctures by the PSA component. Even at a high relative PSA composition of 70%, the crystalUzation process appears to have been significantiy impaired.

The two polymers in these blends are known to erode at very different rates in aqueous environments (180). In physiological conditions, the PSA has an eUmination time of between 2 to 4 weeks, whUst the PLA has an elùnination time of 12 to 16 weeks. Therefore, initial changes in surface morphology should be caused by the loss of the PSA material in the films and the morphology of the PLA material should be exposed.

For 70% PSA:30% PLA films the initial granular continuous film structure observed in the original film rapidly changed during degradation in the pH 12.5 KCl/NaOH buffer solution. The four 10 μm x 10 μm AFM images in Figure 4.15 show data recorded at degradation times of 0, 2, 5 and 10 minutes. These images show that the granular features remained relatively constant in the first stages of erosion, whilst the polymer material between the granules was lost at a more rapid rate. In the image taken following 5 minutes of degradation, the granules are more distinct from the rest of the film. This process continued until after 10 minutes of degradation the granules remained as isolated islands

(a) 70% PSA: 30% PLA

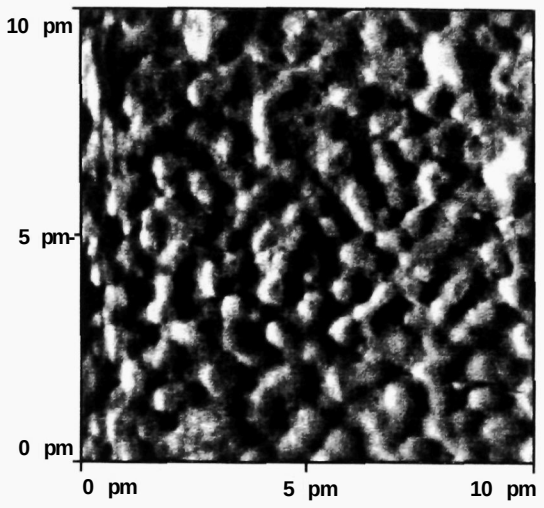


b) 50: PSA : 50% PLA

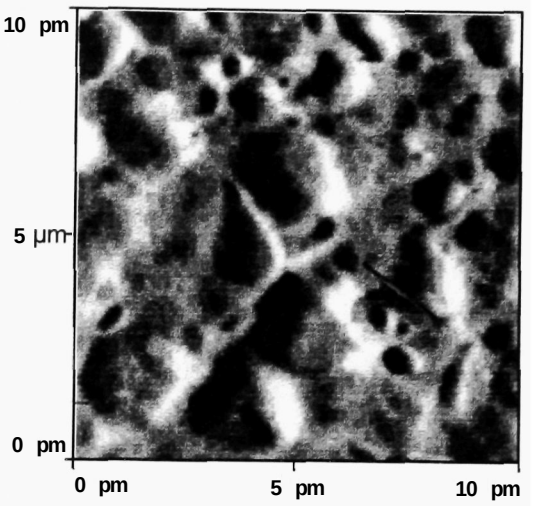


c) 30% PSA:70% PLA

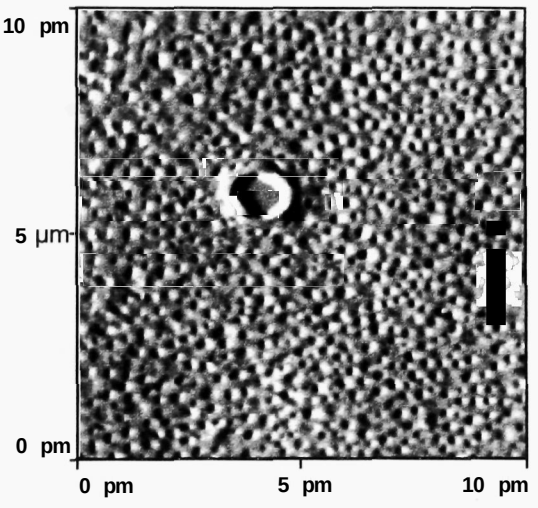


Figure 4.14 10 µm x 10 µm AFM images of the surface morphology of PSA/PLA blends. P = 1.2, I = 0.05, D = 0.05.

(a) 0 min

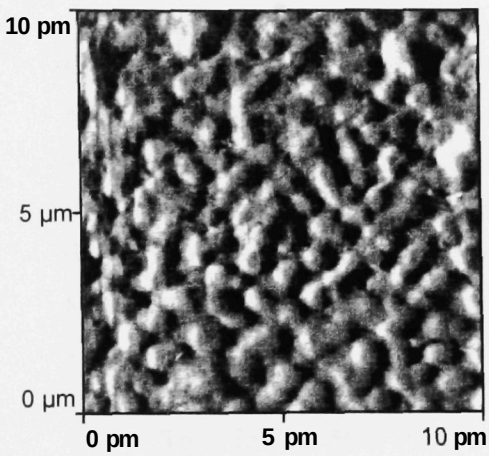


(b) 2 min

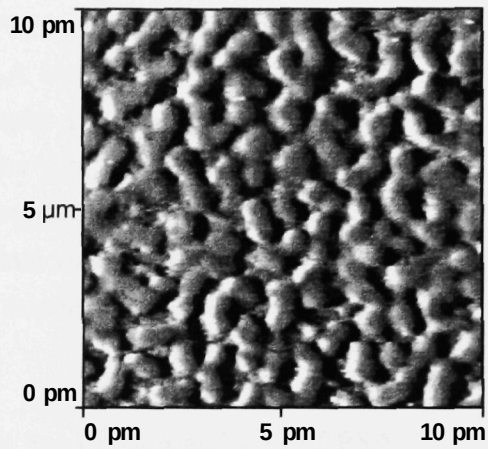


(c) 7 min

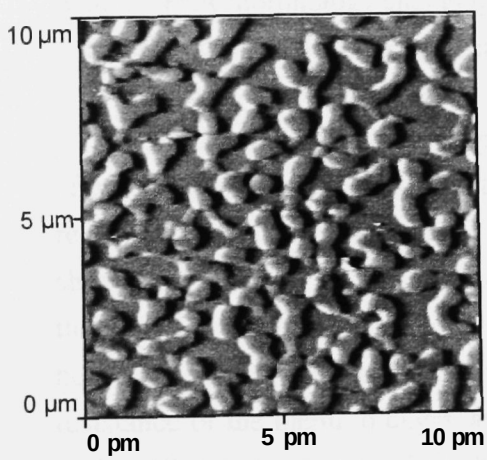


(d) 10 min

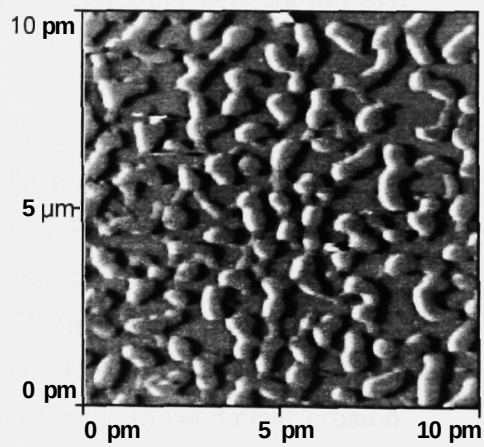


Figure 4.15 10 µm x 10 µm AFM images of the degradation of a 70% PSA:30% PLA film at pH 12.5. P = 0.25, I = 0.05, D = 0.05.

on the substrate surface. This data indicates tiiat tiie PLA material was present as granules in the initial film. PSA material was present between the PLA granules prior to the erosion to give the continuous film observed in the initial surface morphology studies.

In Figure 4.16, four 10 μm x 10 μm AFM images are displayed which show the erosion of the 50% PSA:50 % PLA blend film in tiie pH 12.5 KCl/NaOH buffer solution. Surface topographs prior to the degradation showed a continuous fihn with broad, shallow pits in the surface. As the degradation proceeded these pits could be observed to broaden and deepen. As this erosion process continued, a network stmcture was exposed. This network stmcture remained on the surface for over 40 minutes of exposure to the pH 12.5 buffer solution.

Thus for the 50% PSA: 50% PLA fdm, the erosion and loss of PSA material resulted in the exposure of a network of PLA. Here, the degradation experiment has revealed a fundamental difference in film morphology between the 70% PSA: 30%PLA fdm and the 50% PSA: 50% PLA fihn. As the amount of PLA in the blend increased, an inversion in the phase morphology occurred with the PLA morphology changing from isolated granules in a network of PSA to a network of PLA separating areas of PSA.

Further increasing the proportion of PLA in the blend had a dramatic effect on the degradation characteristics of the thin films. The AFM data recorded during the erosion of the 30% PSA: 70 % PLA sample at pH 12.5 is shown in Figure 4.17. The most noticeable feature of this series of images is the timescale over which they were recorded. The final image was recorded 3 hours after the first exposure of the blend to the pH 12.5, demonstrating the resistance of the blend to degradation, the other blends showed clear erosion within 10 minutes and the fUms became unstable with 40 minutes. The only evidence of degradation occurring to the 30% PSA: 70 % PLA film is a slight increase in the depth of the pits during the first 30 minutes of the experiment

Clearly, this blend displayed a very different pattem of degradation to the blends with lower PLA concentrations. This pattem may be explained by SIMS and XPS studies performed within the Laboratory by Dr Alex Shard (188). These surface chemistry results indicated that there was a significant

(a) 0 min

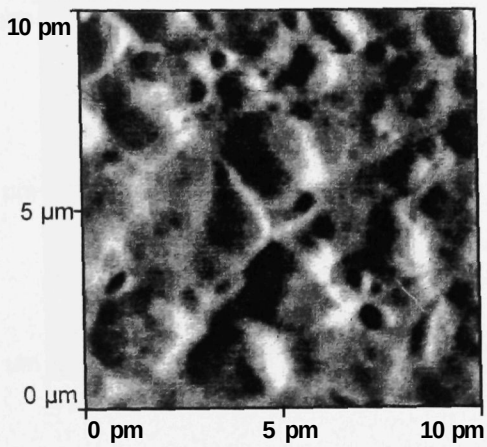


(b) 5 min

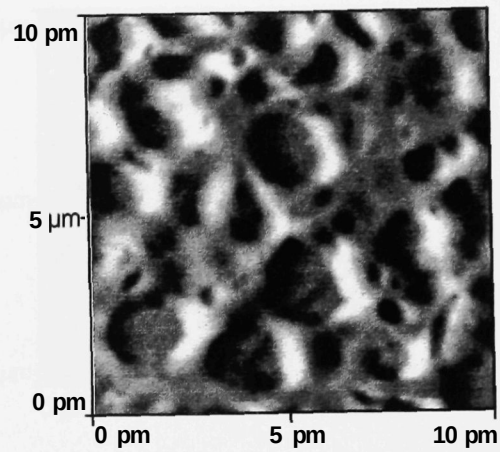


(c) 10 min

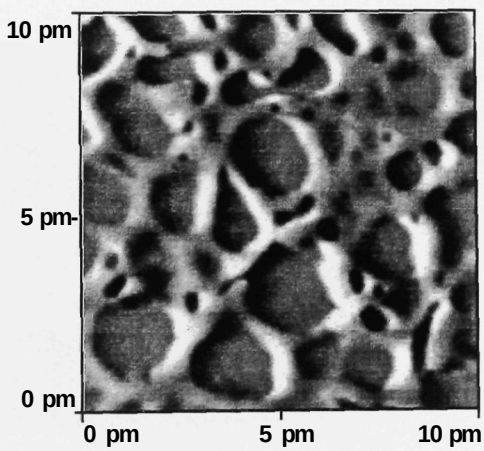


(d) 20 min

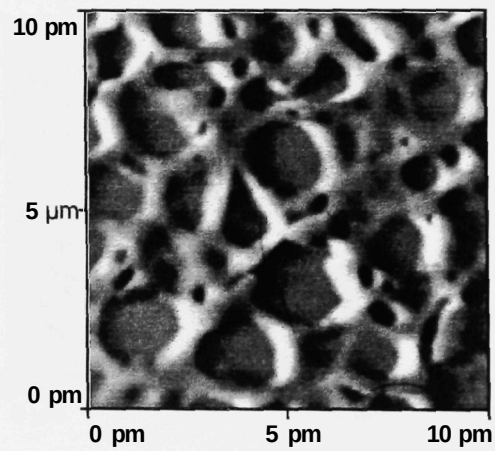


Figure 4.16 10 µm x 10 µm AFM images of the degradation of a 50% PSA: 50% PLA film at pH 12.5. P = 0.15, I = 0.05, D = 0.05.

(a) 0 min

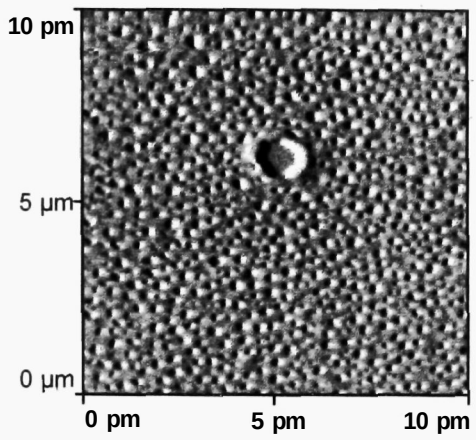


(b) 30 min

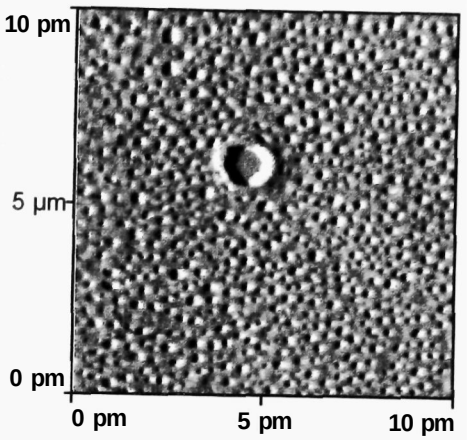


(c) 60 min

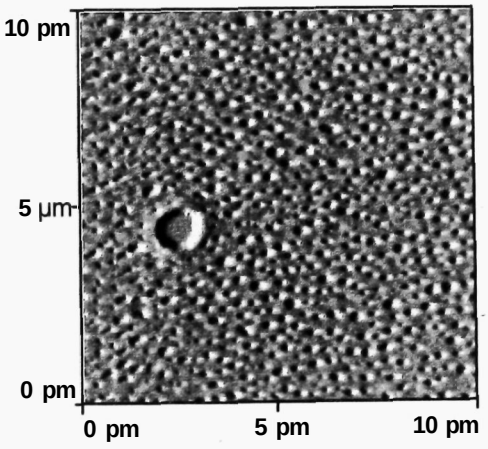


(d) 180 min

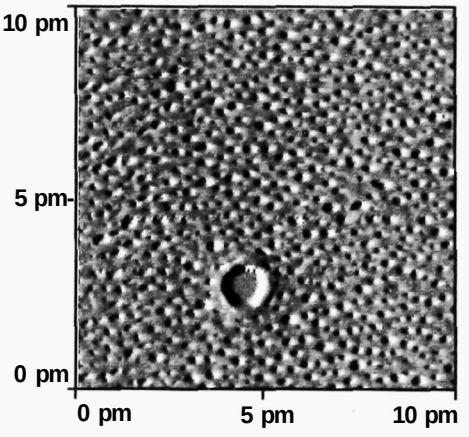


Figure 4.17 10 µm x 10 µm AFM images of the degradation of a 30% PSA:70% PLA film at pH 12.5. P = 1.2, I = 0.05, D = 0.05.

surface enrichment of PLA over PSA. This enrichment may have produced a barrier between the PSA and the pH 12.5 solution. Hence, the kinetics of degradation were determined by the slowly degrading PLA only. For the lower PLA content blend fihns, there appeared to be insufficient surface PLA material to prevent permeation of the hydrolysing solution to the PSA material and hence the film becomes unstable to the high pH environment within minutes of exposure.

## 4.4 Conclusions

The work described in this Chapter represents the first example of the use of *in situ* AFM to study dynamic changes occurring at the soUd/aqueous interface of a polymeric biomaterial. It has been demonsti-ated that the technique can observed the preferential loss of amorphous material over crystalUne fibres on PSA samples. This result confirms previously published findings using SEM, however, the AFM technique has the advantage of recording the change in surface morphology from one area of a sample without the exposure of the polymer to non-aqueous conditions. This allows the evolution of surface morphology changes to be foUowed.

The potential of the technique to enhance the characterization of potential dmg delivery systems has been demonstrated on PSA/PLA biodegradable blends. The ability to determine the influence of polymer phase morphology on surface erosion has generated novel information on the importance of surface enrichment to the overaU degradation kinetics. The abUity of the AFM to follow changes in the surface morphology on one area of the blends during significantly simplifies the interpretation of the dynamic surface changes.

# Chapter 5

# Visualizing the Release of Protein from a Poly(ortho ester) Film

## 5.1 Introduction

The availability of genetically engineered peptide and protein dmgs has provided new clinical opportunities in the ti-eatment of many important disease states (189). For example, protein dmgs are now being employed to overcome hormonal deficiencies (eg. human growth hormone (190) and luteinizing hormone releasing hormone (LHRH) (191)) and to increase the efficacy of the immune system (eg. interferon and interieukin (192)).

The delivery of proteins has been highlighted as a major obstacle to these dmgs achieving their fuU clinical potential (193). Protein dmgs cannot be deUvered by conventional oral methods because they are metabolized rapidly by enzymes in the stomach and their absorption across other mucosal tissue is limited by tiieir large molecular size and low solubiUty in Upid (194). Therefore, parenteral delivery is the dominate form of protein dmg delivery. However, parenteral delivery is not ideal due to the cost and inconvenience of injections. These problems are further exaggerated by the fragility of protein dmgs within the body which demands that injections have to be given frequently.

A number of approaches are been researched as altematives to the conventional parenteral delivery of protein dmgs. Many of these methods rely on increasing the movement of the dmg across a mucosal membrane. Techniques for increasing this movement include the oral deUvery of proteins encapsulated in polymeric microspheres (195), iontophoretic acceleration of protein movement from transdermal patches (194), chemical penetration enhancers (196), and the recent description of the use of ultrasound to increase skin permeabiUty (165). An alternative to enhancing mucosal absorption is the use of the biodegradable polymer

dmg delivery systems introduced in Chapter 4. Heller has extensively detailed the current research in the use of such devices (170). The use of surface eroding biodegradable polymer systems offers the combined advantages of controlled kinetics of release into the body and protection of the protein dmg from metabolism prior to release. Such systems still require parenteral adminstiration or implantation, but the frequency of adminstration is significantiy reduced. Delivery systems with release times of hours to years can be developed depending on the desired kinetics for each dmg.

In this Chapter, the *in situ* AFM techniques developed in Chapter 4 to visualize polymer degradation, are extended to consider the relationship between polymer degradation and the release kinetics of a model protein dmg. In addition, a new method of analyzing the three-dimensional AFM images is described which aUows changes in the volume of protein particles during release to be measured. To perform this development work, a poly(ortho ester) polymer has been chosen due to the published use of these polymers in the delivery of proteins (see section 5.1.1) and due to the simplicity of surface morphology caused by the low crystallinity of the polymer.

### 5.1.1 Poly(ortho esters)

The poly(ortho esters) were developed to overcome the poor predictability of dmg release kinetics that had been reported from implanted polyester based matrices. This poor predictability was caused by the extensive and rapid diffusion of water into the polyesters causing dmg release to be controlled not by the rate of polymer surface erosion, but by the diffusion rate of the dmg out of the hydrated polymer matrix.

The polymer used in the studies described in this Chapter was developed by Heller and co-workers (197,198). The basic stmcture is formed by the addition of 3,9-di(ethyUdene 2,4,8,10 - tetraoxaspiro [5,5] undecane) (DETOSU) monomer to a diol monomer to give the chemical stmcture shown in Figure 5.1. The DETOSU based poly(ortho esters) contain acid labile ortho ester linkages in their backbone stmcture. Within aqueous environments, the ortho ester groups are hydrolysed and

pentaerythritol dipropionate and the diol monomer are generated as breakdown products as shown in Figure 5.2. As indicated in Figure 5.2 the pentaerythritol dipropionate is further hydrolyzed to pentaerythritol and acetic acid.

Although the rate of water permeation into these poly(ortho esters) is slower than the rate for polylactide and polyglycoUde polyesters, the poly(ortho esters) stiU display swelling witiiin a period of one week (199). To overcome this upper limit of useful time of a poly(ortho ester) device, attempts have been made to conti-ol the rate of permeation and hydrolysis using excipients (200). Basic salts have been used to stabilize the core of poly(ortho ester) matrices. These salts inhibit the erosion of polymer within the bulk of the polymer and therefore a surface eroding device is formed. There is also evidence that the addition of acidic anhydrides excipients which are highly soluble in the poly (ortho ester) but poorly soluble in water can generate surface eroding devices with useful lifetimes of upto 1 month (201).

The use of a poly(ortho ester) to achieve the controUed release of an LH-RH analogue protein dmg has been reported in the literature (202). The polymer used was based on the DETOSU stmcture and it was shown that such a system could achieve near-first order release kinetics for a period of 30 days.

## 5.2 Experimental Methods

### 5.2.1 Polymer Material

The poly(ortho ester) used in the current studies was prepared by the addition of a 1,5-pentanediol monomer unit to the DETOSU monomer to form DETOSU 1,5-pentanediol. This polymer was prepared and purified by the group led by Jorge HeUer (APS Research Institute, Redwood City, U.S.A.) using methods described in the literature (203).

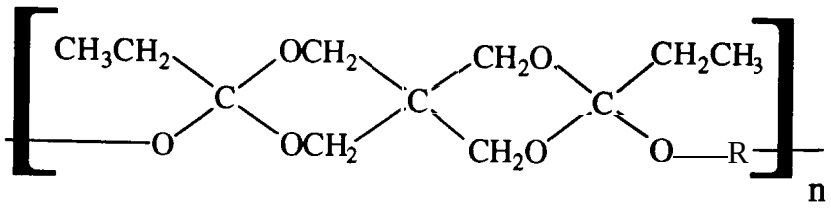


Figure 5.1 Chemical structure of a DETOSU poly(ortho ester).

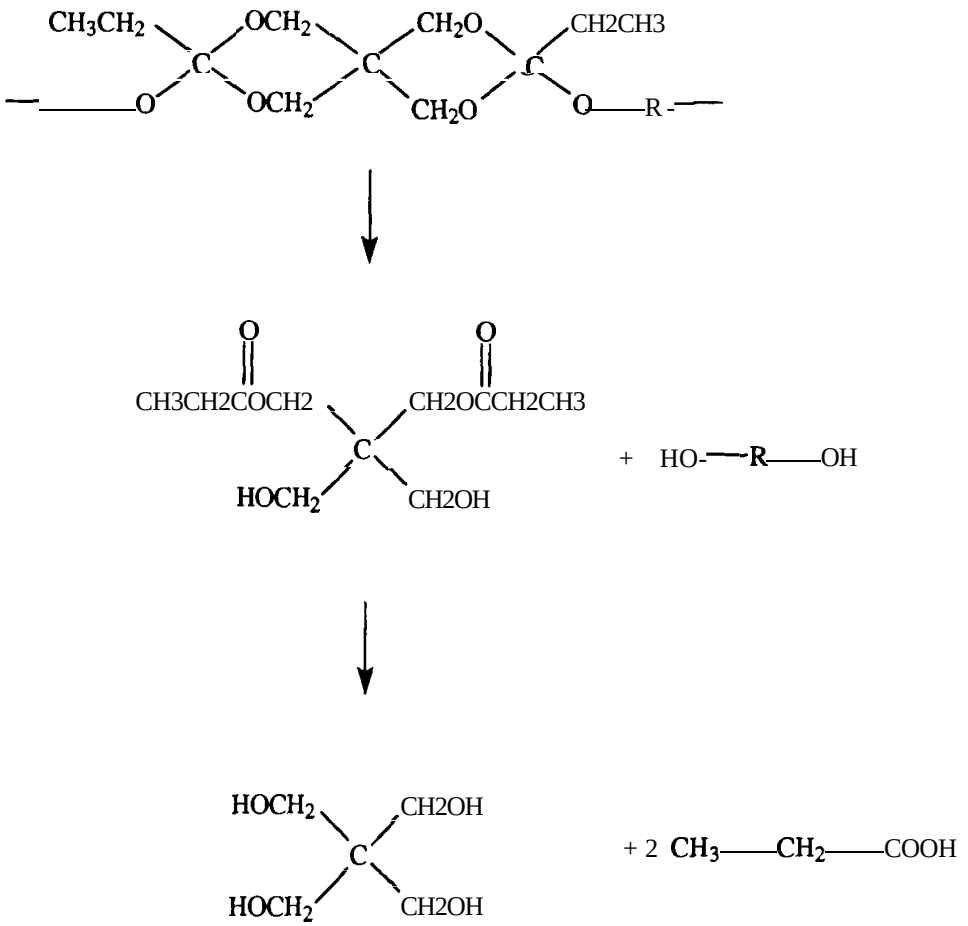


Figure 5.2 The hydrolysis of a DETOSU poly(ortho ester).

### 5.2.2 Sample preparation

Control samples that consisted of the DETOSU 1,5-pentanediol without protein were prepared by spin casting 20 µl aliquots of a 100 mg/ml solution of the polymer in chloroform onto a 1 cm x 1 cm square of freshly cleaved mica. The samples were allowed to dry under ambient conditions for one hour prior to analysis.

The method employed to produce protein containing films was to suspend particles of the protein in the chloroform solution of polymer and spin cast. Such a method has been employed for other biodegradable systems where the polymer and dmg are not soluble or stable in any one solvent (176). The protein, bovine semm albumin (BSA) (Sigma, Poole, U.K.), was gentiy ground to remove large particles before suspension. Then 10 mg of the ground powder was dropped into 1 ml of the 100 mg/ml polymer solution. The suspension was gentiy agitated and then a 20 µl aUquot was spun cast onto a 1 cm x 1 cm square of freshly cleaved mica. Samples were dried under the same conditions as the conti-ol samples.

### 5.2.3 AFM analysis

Visualization of the degradation of the poly(ortho ester) control samples and the protein containing films was performed using the general methods described in Chapter 4 (section 4.2). Initial surface characterization was performed in water at pH 7. Then the water was replaced with a dilute solution of HCl at pH 6 in which the acid-labile poly(ortho ester) degraded.

### 5.2.4 Computational Analysis of Volume Changes

Cross-sectional and volume analysis of the AFM data acquired during polymer degradation was performed on the Genesis II Graphics System (123, 204). The general methods employed to perform the analysis of changes in volume of protein particles during the experiments are described in the relevant Results and Discussion section (5.3.3). Detailed descriptions of the Genesis system are documented in reference 204.

## 5.3 Results and Discussion

### 5.3.1 Characterization of Control Poly(ortho ester) Films

AFM imaging of the surface morphology of the DETOSU 1,5-pentanediol films in air showed a continuous film with granular features evenly distributed across the surface. The 20.1 μm x 20.1 μm AFM unage in Figure 5.3a is representative of the topographies recorded. The granules had diameters between 100 and 1000 nm and heights between 10 and 50 nm.

When the surface of the DETOSU film was exposed to the pH 6 HCl solution, the degradation of the polymer was initiated and led to an increase in the surface roughness of the film and the increased prominence of the granular surface morphology. The AFM images in Figure 5.3 show three of the scans recorded before and during the erosion process. These images record an increase in the prominence of the granules. In order to quantify this interfacial change, analysis of the root mean square surface roughness ($r_{RMS}$) of the images in Figure 5.3 was performed. The $r_{RMS}$ value increased from 11 nm to 25 nm and finaUy to 40 nm for the degradation times of 0, 40 and 70 minutes respectively.

### 5.3.1 Protein Containing Films

The presence of BSA particles in the polymer film resulted in a rougher surface morphology, as demonstrated by the $r_{RMS}$ value of 96 nm for the AFM image of a typical BSA containing polymer film shown in Fig 5.4a (t=0 min). BSA particles, with diameters between 5 and 15 μm and maximal heights above the polymer film of 1 μm, could be identified. The particles were embedded in the polymer film so that only the upper portion contributed to the surface topography. Between the particles, the polymer film had a similar granular morphology to the control film shown in Figure 5.3a.

The morphological changes on erosion of the protein containing film are displayed in the series of eight 60.5 μm x 60.5 μm AFM images shown in Figure

(a) 0 min

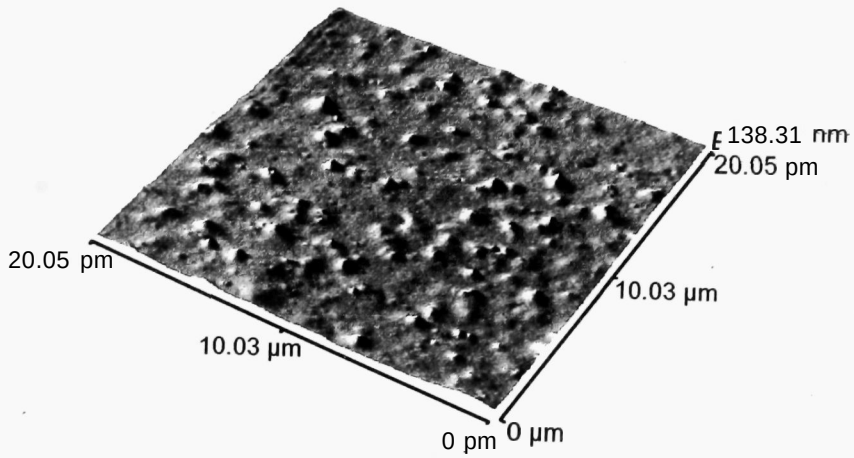


(b) 20 min

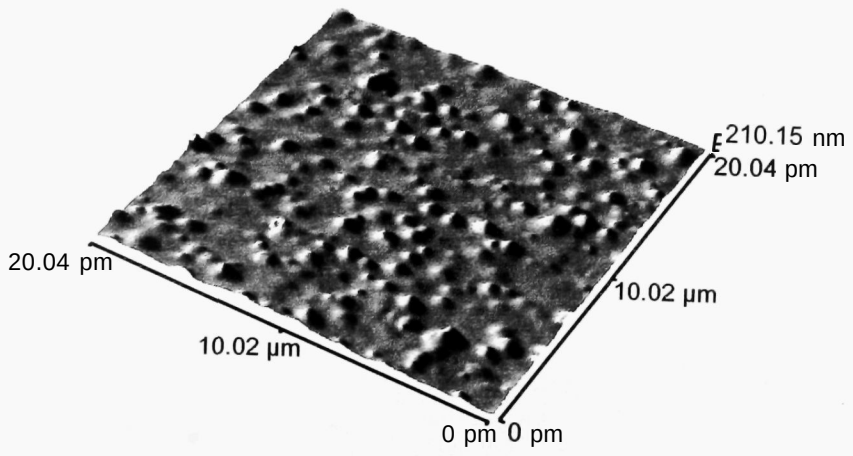


(c) 70 min

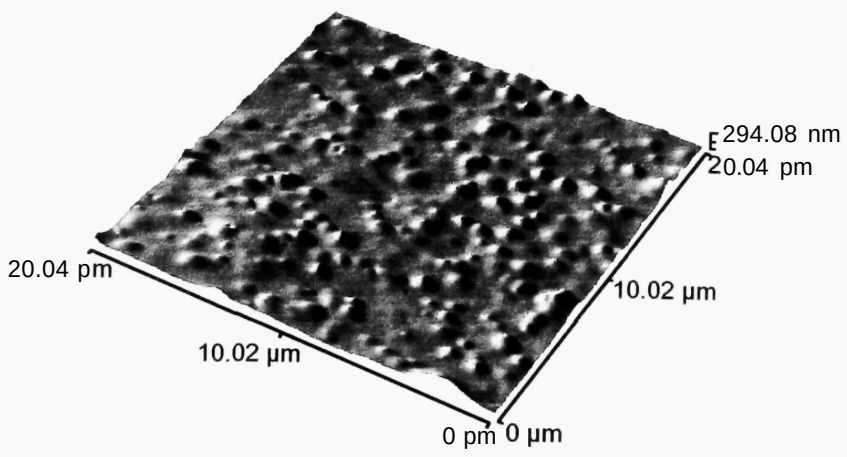


Figure 5.3 AFM visualization of the degradation of a control DETOSU 1,5 pentanediol film in a pH 6 HCl solution. P = 0.25, D = 0.05, I = 0.15. Scan frequency 7 Hz.

(a) 0 min

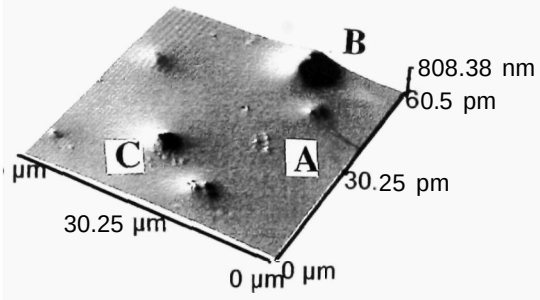


(b) 2 min

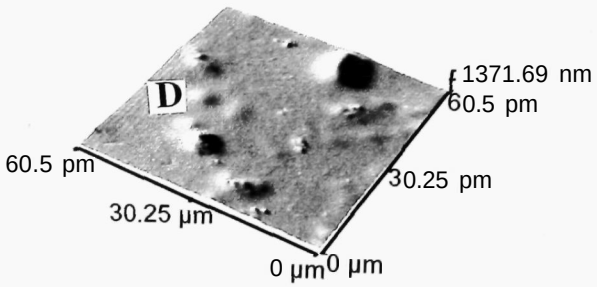


(c) 6 min

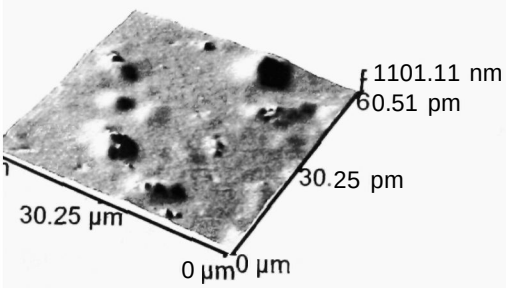


(d) 12 min

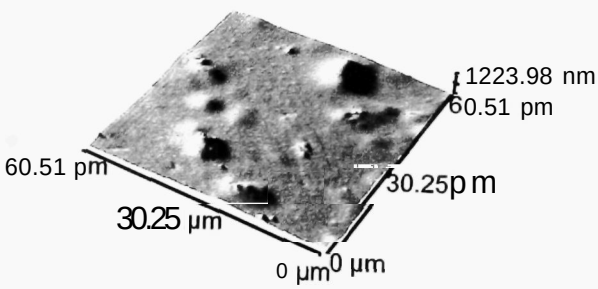


Figure 5.4 AFM visualization of the erosion of a DETOSU 1,5 pentanediol film containing BSA and the subsequent dissolution of the protein particles. Three-dimensional shaded view. P = 0.25, D = 0.05, I = 0.15. Scan frequency 7 Hz.

(e) 27 min

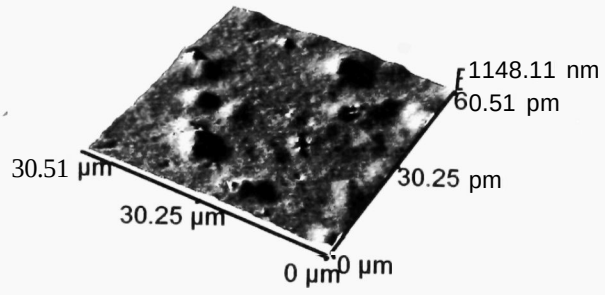


(f) 45 min

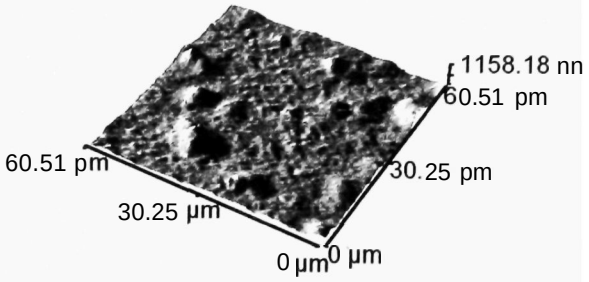


(g) 60 min

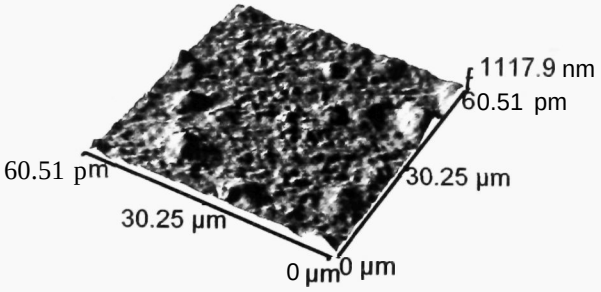


(d) 90 min

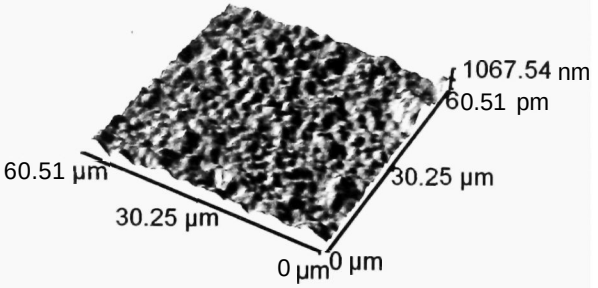


Figure 5.4 Continuation of visuaUzation of protein release in three-dimensional shaded view.

5.4 in three-dimensional representations. To assist comparison of consecutive images, the data is also displayed as two-dimensional representations in Figure 5.5. Analysis of the AFM images showed that the mechanism of erosion was more complex than for the control DETOSU 1,5 pentanediol films. Considering first the areas of the images in Figure 5.4 tiiat appeared to be free of protein (for example, the area marked A in Figure 5.4a (0 min)), it can be seen that the degradation process resulted in the development of a granular morphology and an increase in the surface roughness. The pattem foUowed in the erosion of these areas is similar to that observed for the control films (Figure 5.3).

To appreciate the changes that occurred in those areas of the film that contained protein, this discussion will concentrate on two of the protein particles. These have been labelled B and C in Figure 5.4a (0 min). Protein particle B initially had a maximal height above the polymer fihn of approximately 1.2 μm. This height is shown in the cross-section in Figure 5.6a. After 12 minutes of exposure to the aqueous acidic environment the maximal height value decreased to 800 nm (see cross-section in Figure 5.6a). This indicates that protein dissolution occurred within minutes of the addition of the pH 6 aqueous environment The loss of protein from the film continued throughout the 90 minutes of the experiment as can be observed in both the three-dimensional AFM images and their corresponding cross-sections. In the AFM images the particle can be observed shrinking in size in all three-dimensions, until in Figure 5.4h (t=90 min) the image contrast and the corresponding cross section was dominated by the granular structure of the eroding polymer film and the protein feature had dissolved away.

The dissolution of protein particle C initiaUy occurred at a much slower rate than particle B, as shown in the cross-sectional data in Figure 5.6b. Characterization in water showed the maximal height of the particle above the polymer film to be approximately 600 nm in the original film. This value was maintained in the images corresponding to erosion times of 12, 45 and 60 minutes. Then, there was a relatively rapid loss of the protein material as displayed by the decrease in height of the particle after 90 minutes of erosion. The retarded kinetics of the loss of protein from particle C may indicate that this particle had a thicker coverage of polymer than particle B due to a differential extent of embedding of the

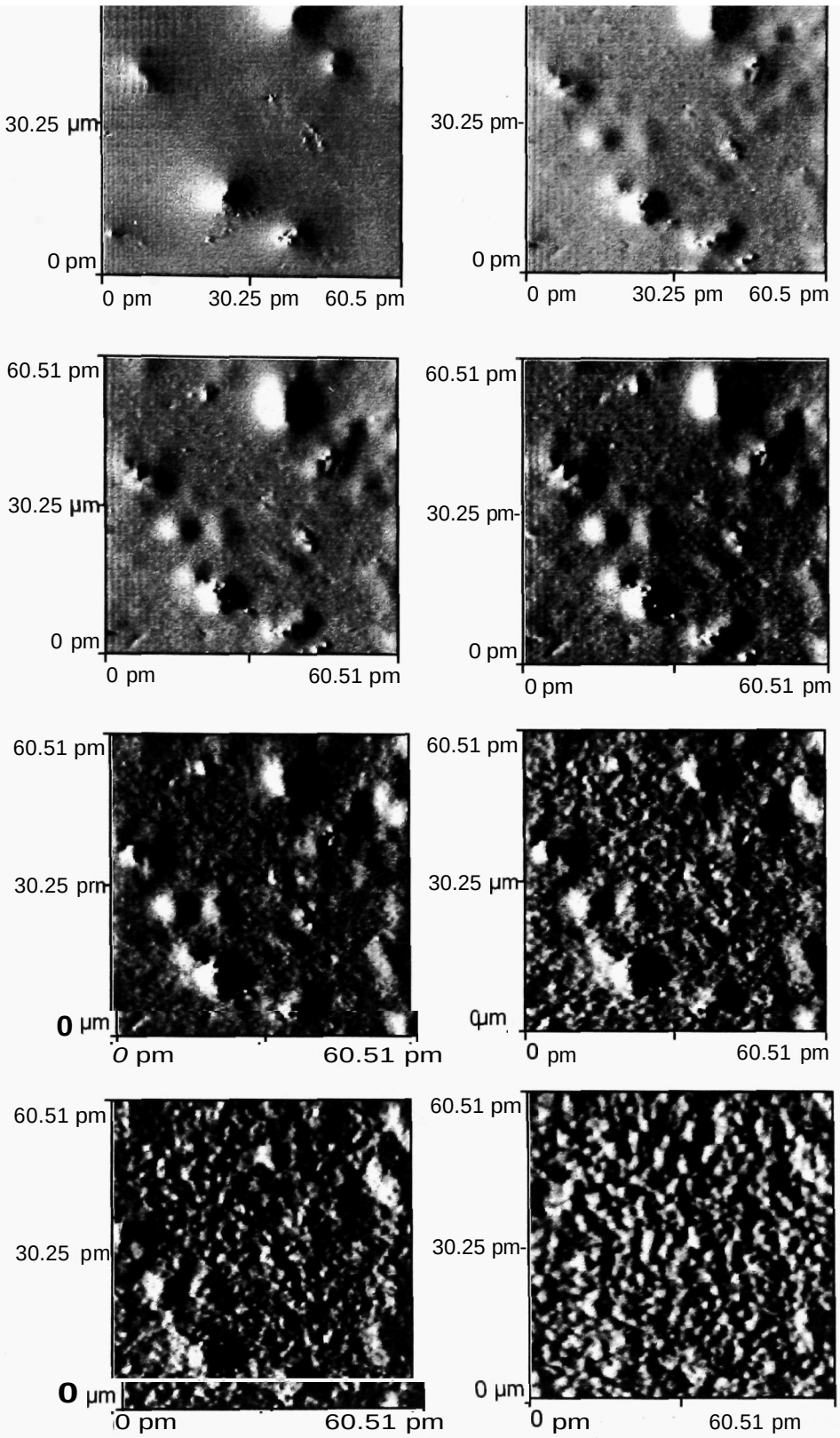


Figure 5.5 Summary view of the data in Figure 5.4 in a two-dimensional representation. .

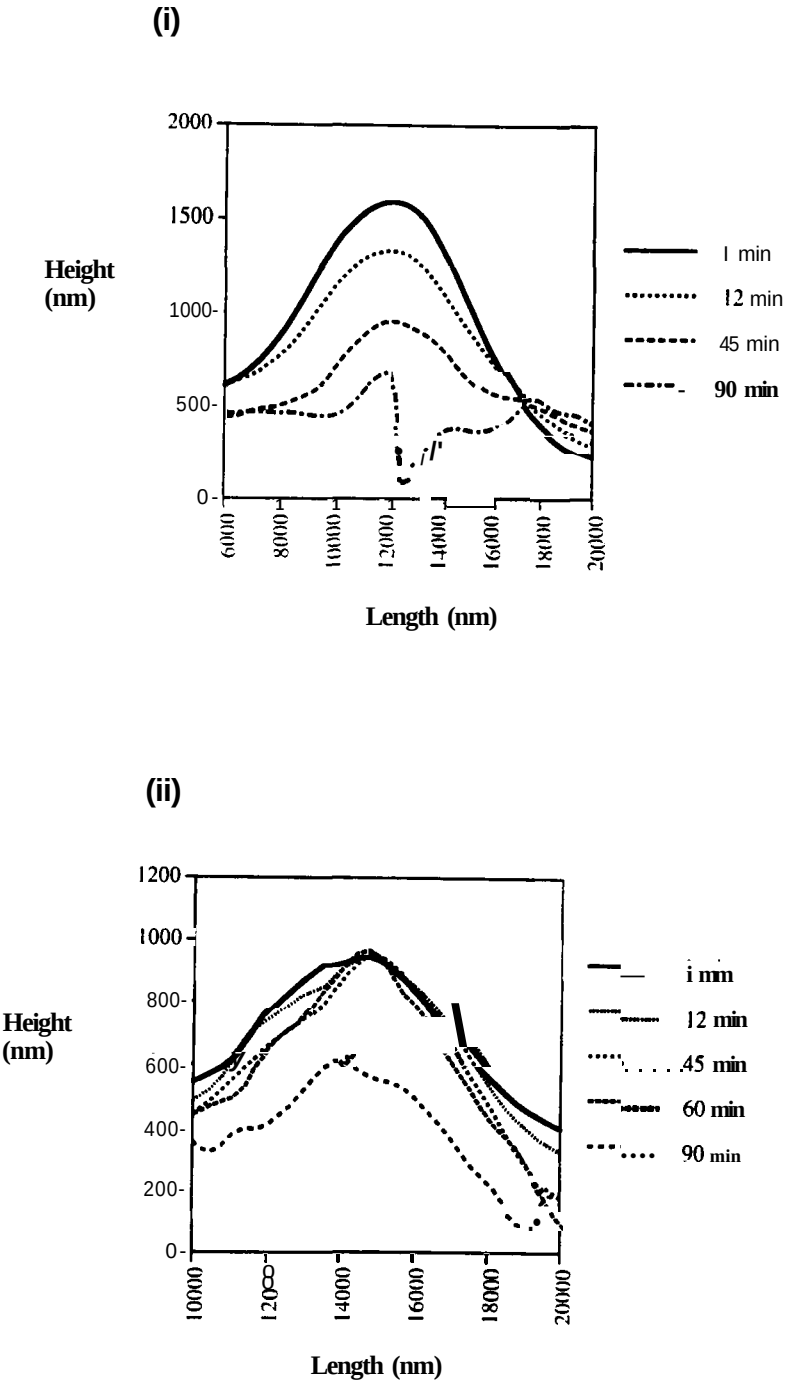


Figure 5.6 Cross-sectional analysis of the dimensions of protein particle B (i) and C (ii).

protein particles. Hence, there could be a lag period in which the height of the particle above the polymer fihn was constant. The lag period may have ended as the erosion of the polymer exposed the protem to the aqueous conditions m the imaging chamber.

A final aspect of the release of protein revealed by the AFM images in Figure 5.4 was the uncovering of protein particles tiiat were initially below the surface and hence, did not contribute to the surface topography. For example, the particle labelled B in Figure 5.4b (t=2 min) could not be identified in Figure 5.4a (t=0 min). The behaviour of this particle during polymer erosion is further discussed in the next section as part of the volume analysis.

### 5.3.3 Quantification of Volume Changes During Protein Release

To enhance the analysis of the three-dimensional changes occurring during the surface erosion and protein dissolution of these systems, computer algorithms have been developed with PhilUp WilUams of the Laboratory of Biophysics and Surface Analysis which aUow the quantification of volume changes occurring to the protein particles during the experiment.

In essence, the procedure for volume analysis involves selecting from the AFM data an area of the polymer film which contained a protein particle and calculating the volume contained between the image surface and the instmmental zero point Changes in volume could then be determined by comparing the volumes of successive AFM images taken as the degradation progressed. However, the procedure is complicated by drifting of the scan region in all three-dimensions between the capture of each image. This drifting means that the absolute z-height of the AFM images and the x,y plane position of the protein particles in the topograph varie in an unknown manner from one scan to the next

To overcome the problems caused by instrumental drift and permit accurate volume analysis, the exact centre of the protein particle being analyzed has to be identified. To determine this x,y position, a threshold image was generated of the

original AFM topograph (205). This binary image is a lateral section taken through the AFM data. Any pixels with a height above the section are given a value of 1, aU others are set to zero. The threshold image of a 14.2 μm x 14.2 μm area around protein particle B is shown in Figure 5.7. The threshold value for this image was set at half way between the maximal z displacement of the topograph. With carefully selected threshold values the white pixels in the binary image identify the cross-section of the protein particle, the centre of which may be found by skeletonization (205). In skeletonization, boundary pixels with 2 or more white pixel neighbours are removed recursively until no change in the image occurs. The centre of the protein is identified by the intersection of the two lines generated by this procedure. The skeletonization of the threshold image in Figure 5.7 is displayed in Figure 5.8, the successive images show each step in the procedure, starting with the complete threshold image and finishing with the single pixel width cross.

Having identified the centre of a protein particle, a square area of known dimensions whose centre lies at the protein particle centre was enlarged from the original AFM topograph. This enlarged area was then used in the calculation of the volume. Hence, for each time point in the experiment the scan area used in the analysis was identical in x and y dimensions and is positioned exactiy on the centre of the protein particle.

The above threshold and skeletonization procedures overcame problems of x,y plane drifting, however, the problem of z-height drift still remained. To elimmate tiiis vertical drift effect the volume change calculated for each image is the relative volume change of the protein particle to the polymer. The schematic diagram in Figure 5.9 shows, in cross-section, the procedure for calculating this relative volume change. The maximum height of the protein particle at the calculated centre was recorded (Zp). Then, the volume of a box (Vp) with the x,y dimensions of the scan and a height value of $Z_p$ (above the instmmental zero) was calculated. The measured volume of the AFM scan area ($V_{AFM}$) was then subtracted from this box volume (Vp). The change in this volume ($V_{DIFF}$) is calculated for each of the AFM images and by subtracting this value at each time point from the value of $V_{DIFF}$ at 0 mins, the change in tiie volume of tiie protein particle relative to the

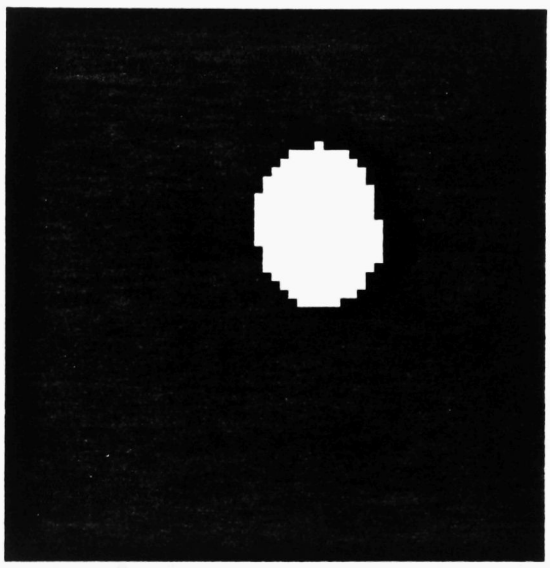

Figure 5.7 A direshold image of protein particle B.

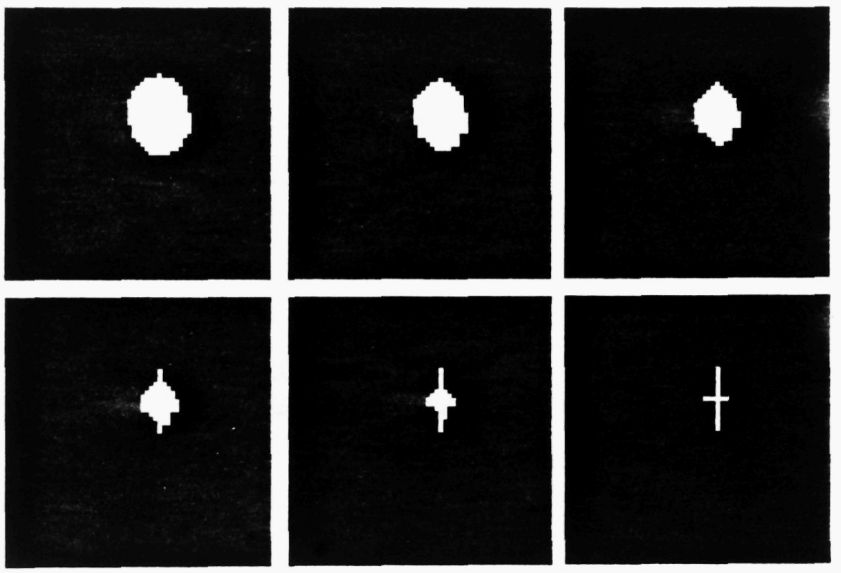

Figure 5.8 Skeletonization of the threshold image in Figure 5.7.

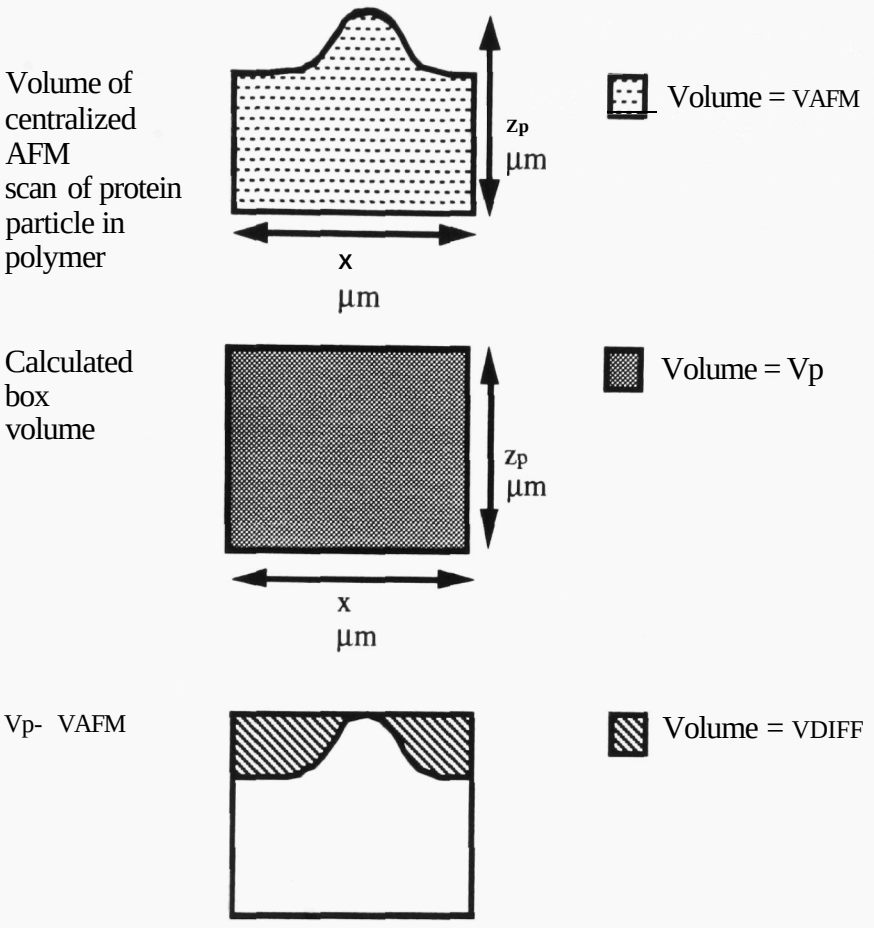


Figure 5.9 Schematic diagram of the calculation of the relative volume of a protein particle in the polymer matrix. The AFM recorded volume of the protein particle in polymer matrix $V_{AFM}$ is subtracted from the box volume $V_p$ (calculated from protein particle height and the scan dimensions) to give the volume $V_{DIFF}$. Subtraction of the values of $V_{DIFF}$ from consecutive images enables the relative change in volume of protein particle, compared to the polymer matrix, to be measured.

polymer surface was determined. It should be noted that the effect of the AFM probe shape on tiie volumes has not be included in the current discussion. Methods of estimating the effect of probe convolution on the AFM images without prior knowledge of the exact probe shape are currentiy being investigated (206).

The above procedure has been used to analyze the relative volume changes occurring to the protein particles labeUed B and D in Figure 5.4a (t=0 min) and 5.4b (t=2 min) respectively. The graph in Figure 5.10 is a plot of the relative change in volume of protein particle compared to polymer matrix against time for both these particles. For protein particle B, the volume analysis confirms the continual loss of protein from the surface over the 90 minutes experiment. The negative gradient of the plot demonstrated that the volume of the protein particle is continually decreasing compared to the polymer matiix. The total volume change was calculated as 103 $\mu m^3$.

The analysis of particle D revealed a different pattem of volume change. Here, the initial slope of the volume change plot was positive. This indicates that the relative volume of the protein particle was increasing as compared to the polymer matrix. This uncovering of the particle continues for the first 60 minutes of the experiment Then, in the last 30 minutes of the experiment, the protein particle was removed by dissolution. The uncovering of this subsurface particle indicates that the polymeric material which is associated with the protein is being eroded at a slower rate than the surrounding polymeric material. However, the underlying mechanism of this process is not yet understood.

## 5.4 Conclusions

The work described in this Chapter represents an extension of the use of *in situ* AFM to visualize the dynamic surface events which underUe the mode of action of surface eroding polymeric controlled release devices. The technique has been employed to image the simultaneous erosion of a biodegradable poly(ortho ester) and the dissolution of embedded protein particles.

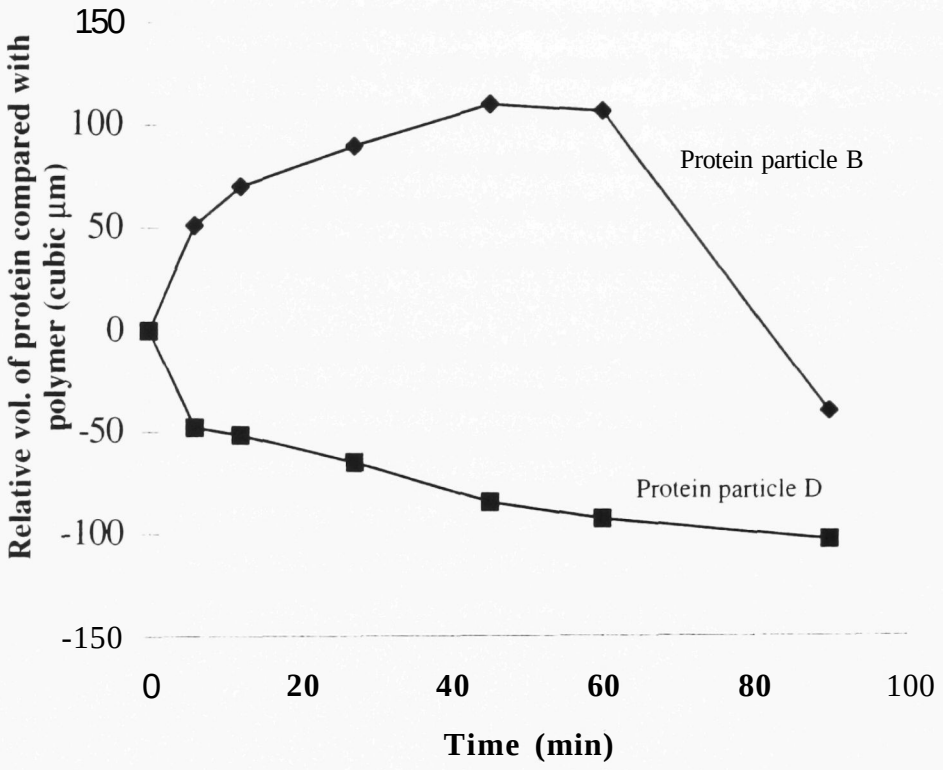


Figure 5.10 Graph of the relative change in volume of a protein particle compared to the polymer matrix against time for particle B and D (see Figure 5.4). A negative gradient indicates that the volume of protein particle has decreased more rapidly than the volume of the surrounding polymer matiix.

The work indicates that there are three species of protein particles within the polymer film. Some particles which are prominent in the initial surface morphology, such as particle A, begin dissolution within minutes of contact between the poly(ortho ester) film and the acidic aqueous medium. Another group of particles, such as particle B, are present in the initial surface morphology but do not begin to dissolve until polymer degradation has progressed for a period of time. FinaUy, some particles are initiaUy completely covered by polymer but during polymer erosion they become uncovered before they are removed by dissolution. An example of this final type of particle is particle D. The mechanism by which these particles are uncovered is unknown but it must involve the surrounding polymer being eroded at a faster rate than the protein material is dissolved.

The computer methods developed to measure the changes in volume of protein particles during the experiments have successfully confirmed the different rates of dissolution. Problems with drifting of the AFM instmment during image acquisition restrict the calculations to a measurement of the relative volume of protein above the polymer matrix, but this technique still provides useful information for comparing the kinetics of protein particle dissolution.

# Chapter 6

# Simultaneous AFM/SPR Analysis of Polymer Degradation.

## 6.1 Introduction

The first three experimental Chapters of this diesis have described a progression in the type of information obtained from polymeric biomaterial surfaces with the AFM. In Chapter 3, the AFM was used to image the static surface morphology of a polymeric biomaterial. Then, in Chapter 4 advances in the use of *in situ* AFM within aqueous environments were harnessed to visualize dynamic changes occurring during the erosion of a number of biodegradable systems. This *in situ* application provided data about the influence of polymer morphology on the mechanism of degradation from a semi-crystalline homopolymer and a polymer blend, however, the data provided no information conceming the kinetics of the erosion. The computational methods described in Chapter 5 have attempted to add a kinetic component to the data through analysis of volume changes. In this final experimental Chapter, the concept of combining kinetic data with the morphological data from an AFM is extended with the introduction of the combined AFM/surface plasmon resonance instmment. The biomedical potential of the surface plasmon resonance instmment (SPR) is discussed in the next section. The experimental work described is part of a larger project to design, constmct and implement the combined AFM/SPR. The design and constmction was performed by a number of members of the Laboratory of Biophysics and Surface Analysis (see reference 128 and Acknowledgements).

### 6.1.2 Surface Plasmon Resonance Analysis in Biomedical Science

The design of a Kretschmann SPR instmment and the mechanism of data acquisition have been described in Chapter 2 (section 2.2.1). In brief, the SPR instrument monitors changes in the optical properties of tiiin layers of insulating

materials above the silver surface of the SPR sensor slide. These optical properties can be related to the real-time changes in the concentration or thickness of material present at a surface (124-127).

With reference to biomedical research, SPR analysis offers a sensitive real-time technique to monitor changes occurring at soUd/aqueous interfaces. The principle area of application has been in the study of Ugand-receptor binding (207). Here, the SPR can be used to measure binding kinetics, as demonstrated by studies on the binding of monoclonal antibodies to tobacco mosaic vims peptide (208) and the interaction between repressor proteins and DNA (209). A number of groups have also demonstrated that SPR analysis can be utilized in epitope mapping (210, 211). In these studies, antigen binding sites are identified by the SPR-detected binding of specific monoclonal antibodies to target macromolecules which are covalently coupled to a hydrogel support (212).

In addition to studies of ligand-receptor binding phenomena, SPR analysis is currentiy being employed to study non-specific interaction between biomolecules and synthetic surfaces. For example, Davies *et al* have detected a significant change in the functionality of ferritin antibodies depending on the method of immobilization of the antibodies to polystyrene surfaces (213). SPR analysis is also being used as method to quantify the adsorption of proteins to synthetic polymer surfaces (214). These studies offer a method of elucidating the underlying processes involved in determining the biocompatibility of polymers.

The work described in this Chapter describes a new application of the SPR instrument for analyzing polymeric biomaterials. The SPR is used to measure changes in the thickness of thin films of biodegradable polymers during surface erosion. The concept behind these experiments is that as a polymer film erodes and degradation products are removed by dissolution the SPR detects a decrease in the amount of material above the sensor surface through a decrease in the SPR angle (see Chapter 2). This work is based on a number of published SPR studies in which the SPR has been used to monitor changes in the thickness of thin films of polymeric and non-polymeric materials. The eariy work in this field was performed at the IBM research laboratory, San Jose (215, 216). These studies concentrated on layers of the

fatty acid salt, cadmium arachidate deposited on stiver surfaces. Other pubUshed studies in this field include the analysis of the influence spin casting speed on the thickness of overiayers (217), the thickness of Langmuir-Blodgett films (218), and the adsorption of layers of alkanes onto gold from the gaseous phase (219).

## 6.2 Experimental Methods

### Polymer preparation

All the polymers used in these experiments have been introduced in previous Chapters. PSA and PLA synthesis and stmcture has been described in section 4.2.1. The DETOSU 1,5 pentanediol poly(ortho ester) was described in section 5.2.1.

### Sample preparation

Thin films of the homopolymers and polymer blends were prepared by spin casting as described in section 2.2.3.

## 6.3 Results and Discussion

For clarity, this section has been divided into three parts. In the first part the degradation of a DETOSU 1,5 pentanediol sample is analyzed by SPR alone to familiarize the reader with the results obtained by this instmment In the next two parts, results are presented from the combined AFM/SPR for DETOSU 1,5 pentanediol and for a number of PSA/PLA immiscible blends.

### 6.3.1 SPR Analysis of a DETOSU 1,5 pentanediol Film

The effect of spin coating a thin film of the poly(ortho ester) onto the silver surface of the SPR sensor was to increase $\theta_{SPR}$ (the SPR angle) from a value of 64° to 71.4°. This increase is shown in Figure 6.1 and is expected due to the increased quantity of the polymer above the sensor and within the detection range of the SPR. In addition, to the increase in the absolute value of $\theta_{SPR}$ there

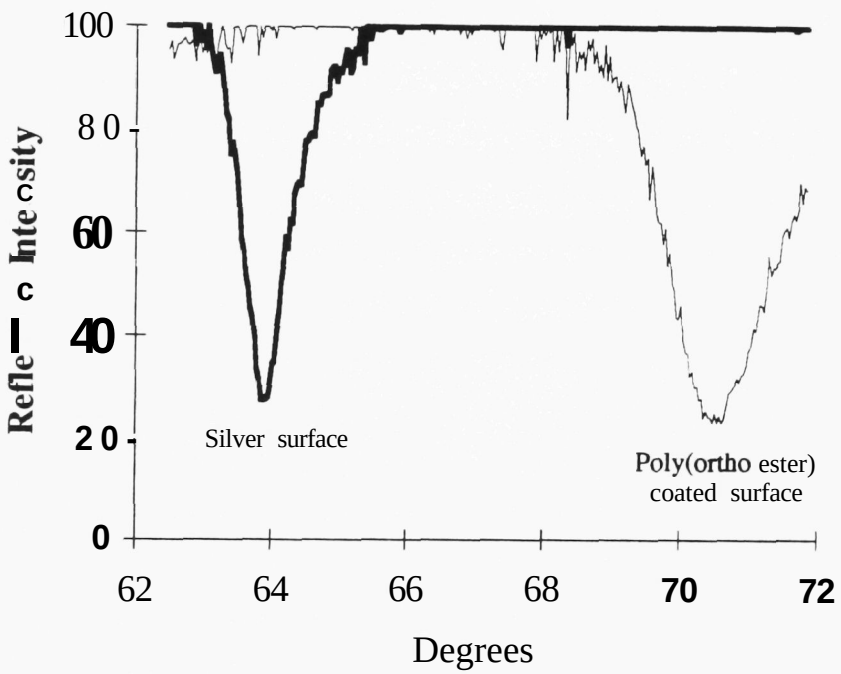


Figure 6.1 The increase in $\theta_{SPR}$ due to spin casting a thin poly(ortho ester) film onto the silver surface of an SPR sensor slide.

was also an increase in the half-width of the SPR trough from 0.70° to 1.84° as a result of the presence of the polymer layer. This effect of thin fdms increasing the SPR half-width has been documented in the literature previously for non-absorbing films of LiF and other materials (125).

Initially, the fluid pumped into tiie liquid ceU of the SPR instrument was de-ionized water at pH 7. Having measured $\theta_{SPR}$ for the polymer-coated SPR sensor, the fluid in the syringe supplying the liquid cell was changed to a pH 3.5 HCl (aq) solution and the syringe driver was programmed to pump fluid into the ceU at a rate of 1 $\mu l sec^{-1}$. The time at which pumping of the acidic solution commenced was taken as t = 0 min. The SPR data displayed in Figure 6.2 shows the change in $\theta_{SPR}$ witii time as the poly(ortho ester) film degraded within the acidic environment. For the first 5 mins, $\theta_{SPR}$ maintained a value of 71.4°. This lag period can be attiibuted to the time taken for the HCl solution to travel through the tubing connecting the syringe to the liquid cell. At t = 5 min, the effect of polymer degradation on $\theta_{SPR}$ became evident as the value fell at a rate of $0.260° min^{-1}$ for 4 minutes.

At this stage of the experiment (t = 9 min), the HCl solution in the syringe was exhausted and the pumping of fluid by the syringe driver was stopped. As a result of the solution within the liquid cell being stationary, the rate of decrease of OSPR slowed over the next 12 minutes untU at t = 20 min the value of 6SPR became static. This effect may be attributed to a stagnant layer of liquid above the degrading polymer surface which from t = 9 min to 21 min would contain an increasing concentration of the degradation products. As the concentration increased it is possible that the HCl solution became saturated and, hence, the removal of further poly(ortho ester) from the fdm was inhibited.

At t = 50 min, the syringe was re-filled with the pH 3.5 HCl solution and pumping recommenced. Immediately, the value of $\theta_{SPR}$ began to fall and the rate of decrease reached a value of $0.168° min^{-1}$. In the final stages of this experiment, as 9SPR approached a value expected for an uncoated stiver surface,

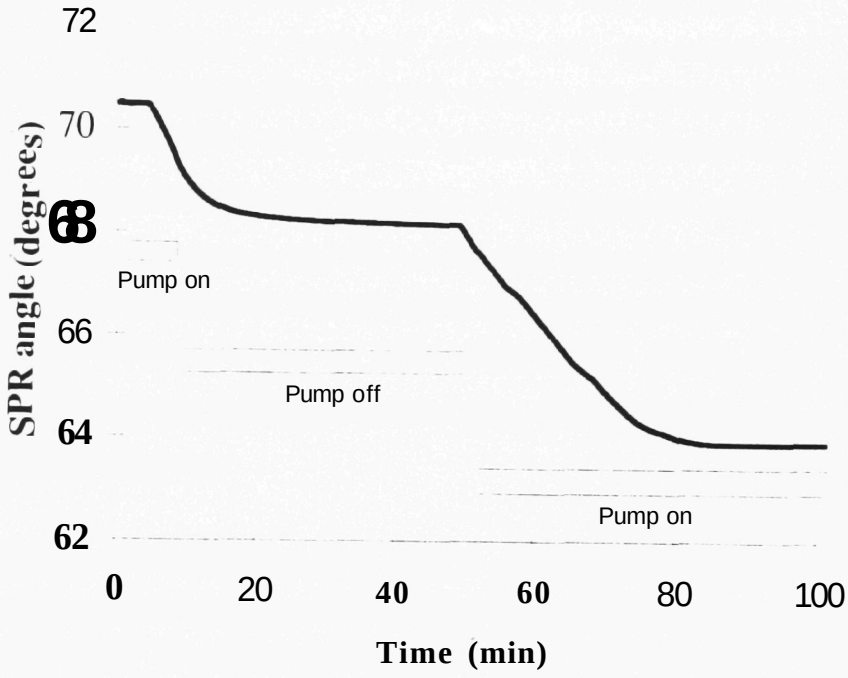


Figure 6.2 SPR data recorded during the degradation of a DETOSU 1,5 pentanediol sample in a pH 3.5 HCl solution.

the rate of fall of 0SPR again slowed significantly and at t = 82 min became static. This deceleration of degradation was caused by exhaustion of the polymer film.

This first example of the application of SPR to monitor polymer degradation introduces the concept of relating 6SPR to the extent of degradation. Currently, it is not possible to convert the change in $\theta_{SPR}$ to a precise measurement of the change in thickness of the polymer film because the sensitivity of the SPR response is dependent on the overlayer thickness. Therefore, if two separate polymer films, one 100 nm thick and the other 200 nm thick, were analysed by SPR during surface erosion, a I nm decrease in film thickness for the 100 nm film would produce a slightly larger fall in 8SPR than the same decrease in thickness for the 200 nm film. The rate of decay of the SPR response with increasing distance from the silver surface is currently being modelled within our Laboratory and by other groups (207). When this modelling is available it may be possible to convert $\theta_{SPR}$ changes directiy into absolute changes in film thickness.

The sensitivity of the SPR data to changes in the kinetics of polymer degradation have been demonstrated by studying the pH dependence of the rate of erosion of a DETOSU 1,5 pentanediol film. For these studies, buffered solutions of potassium hydrogen phthalate with sodium hydroxide or hydrochloric acid were used to change the pH within the liquid cell between 5.5 and 3.5. Initially, 1 ml of pH 7 water was pumped into the AFM/SPR compartment to check that a constant SPR angle was obtained. Then, a further 1 ml of a pH 5.5 buffer solution was pumped into the cell and the change in SPR angle was monitored. This procedure was then repeated using 1 ml of a pH 5.0 buffer solution to replace the higher pH buffer. The experiment continued in this manner. After each buffer was pumped in, a lower pH buffer was used to replace it and the SPR angle change was recorded.

The SPR results from this experiment are displayed in Figure 6.3. Each arrow indicates the time at which the pH of the pumped solution was lowered, starting with pH 5.5 at 0 min, then progressing to pH 5.0, 4.5, 4.0 and 3.5. Overall, the SPR angle shift curve showed an increase in the rate of the erosion

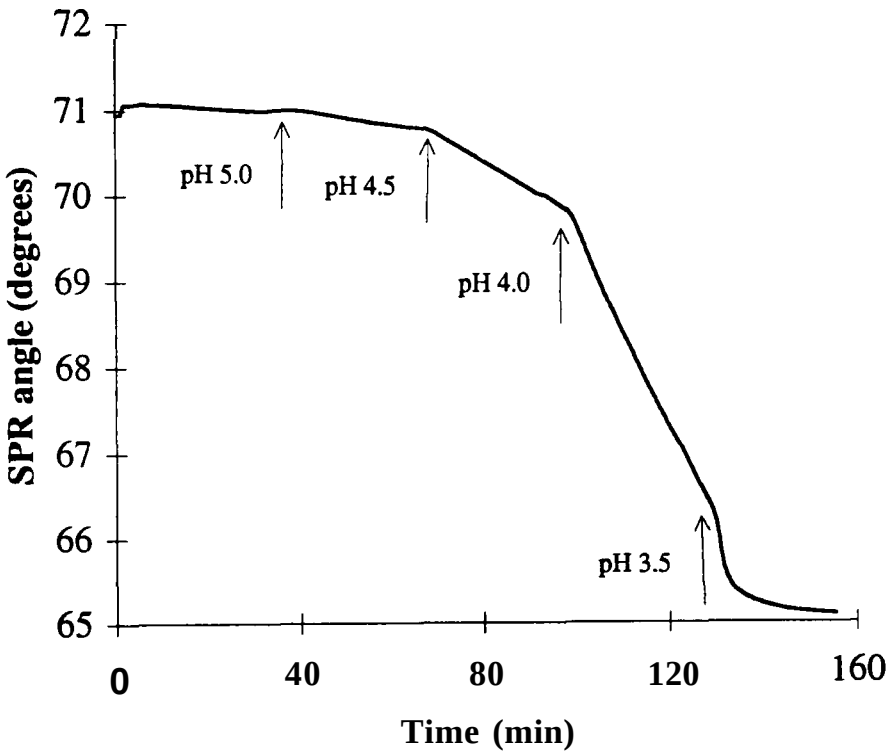


Figure 6.3 SPR analysis of the pH sensitivity of the surface erosion of DETOSU 1,5 pentanediol. The arrows indicate the times at which the pH of then solution in the Uquid œU wás decreased.

as the pH was lowered.The SPR data in Figure 6.3 displayed an acceleration of the rate of shift, with recorded values of -0.007, -0.012, -0.040, -0.125 and-$0.280^{\circ}min^{-1}$ at pH 5.5, 5.0, 4.5, 4.0 and 3.5 respectively. On addition of the pH 3.5 solution, the SPR shift rate decreased to zero after an initial rapid rate of shift. This rate decrease was again caused by the loss of the final polymeric material from the silver surface.

### 6.3.2 Combined AFM/SPR Analysis of Poly(ortho ester) Films

The AFM and SPR data recorded during the erosion of a spin cast DETOSU 1,5 pentanediol fdm are displayed in Figure 6.4 and 6.5 respectively. The AFM component of the combined instmment uses a 3 μm scanner tube (see section 2.3) and therefore the AFM data visualizes the degradation process on a smaller length scale than the previous description for the DETOSU 1,5 pentanediol polymer in Chapter 5. OveraU, the 3 μm x 3 μm images in Figure 6.4 showed a process of pit formation. The initial polymer morphology was composed of a smooth film with a surface roughness of 5.2 nm. The surface of the film possessed a number of shallow pits with depths of between 1 and 6 nm. The SPR data in Figure 6.5 showed that the presence of this film on the SPR sensor generated a value of 67.4 ° for 0SPR.

When a pH 4.0 HCl solution was introduced into the Uquid cell of the combined instmment 6SPR initially increased due to the higher ionic strength of the buffer compared to the displaced water. Within 1 min, at t = 4 min, the erosion of the poly(ortho ester) produced the expected fall in GSPR. From t = 5 to 30 min $\theta_{SPR}$ fell at a rate of $0.084^{\circ}min^{-1}$ . During this period, two AFM images were recorded which demonstrate that the AFM can record the morphological changes generated during the surface erosion. In Figure 6.4b at t = 17 min, the image records the formation of a number of new pits and a general expansion of existing pits. This represents the first demonstration of pit formation as a mechanism of polymer erosion for a poly(ortho ester) system. The process of pit formation and deepening continued as displayed in Figure 6.4c, t = 23 min. At this stage, the topography of material at the base of the pits was granular indicating that stiver surface of the SPR sensor had been exposed.

(a) 0 min

(b) 18 mtn

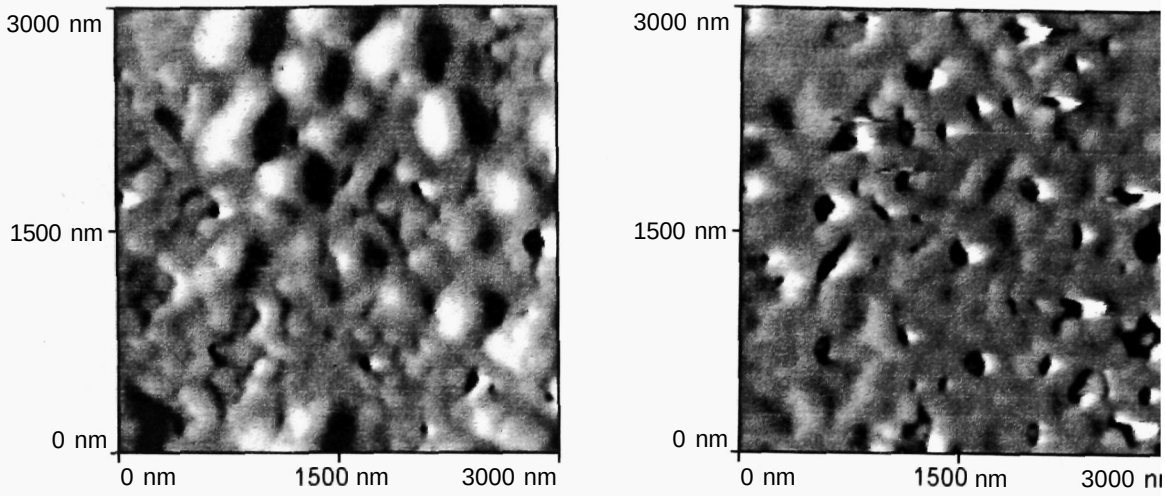


(c) 23 min

(d) 27 min

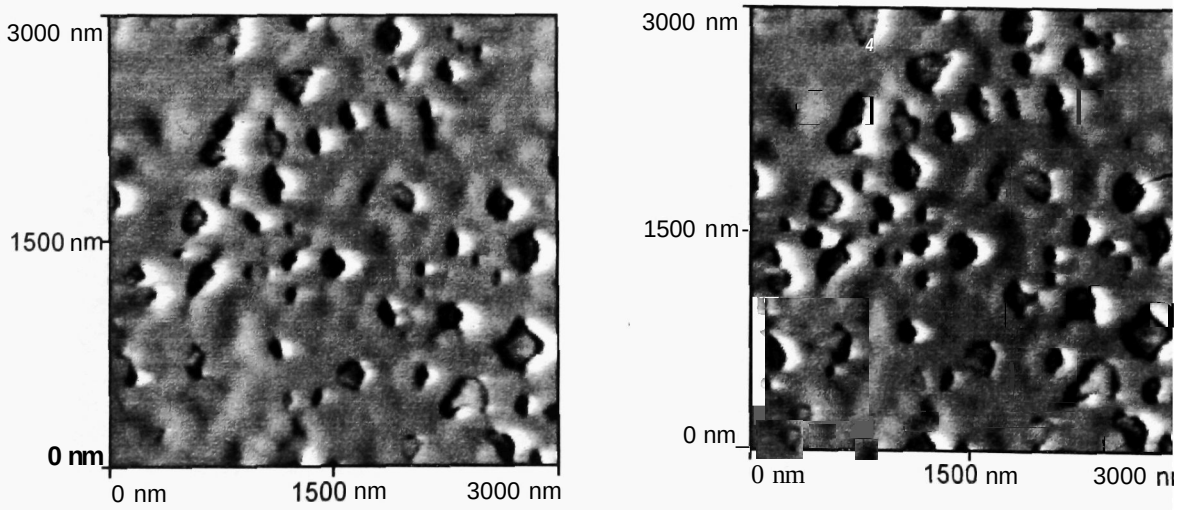


Figure 6.4 AFM images recorded during the degradation of a DETOSU 1,5 pentanediol film. P = 6, I = 1, D = 1.

(e) 36 min

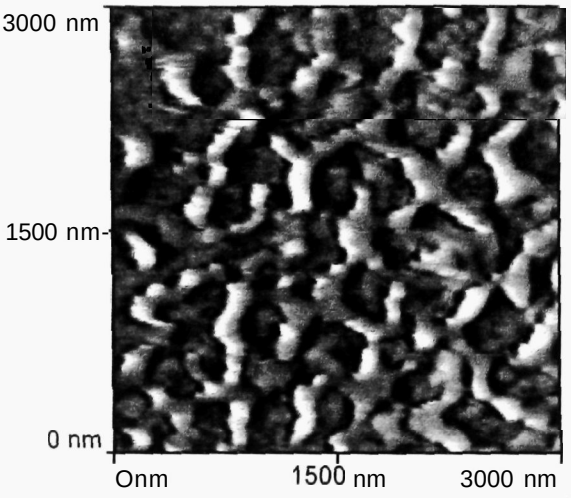


(f) 41 min

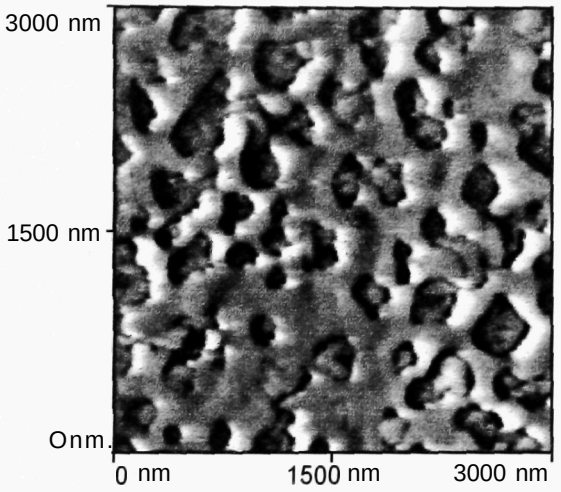


(g) 53 min

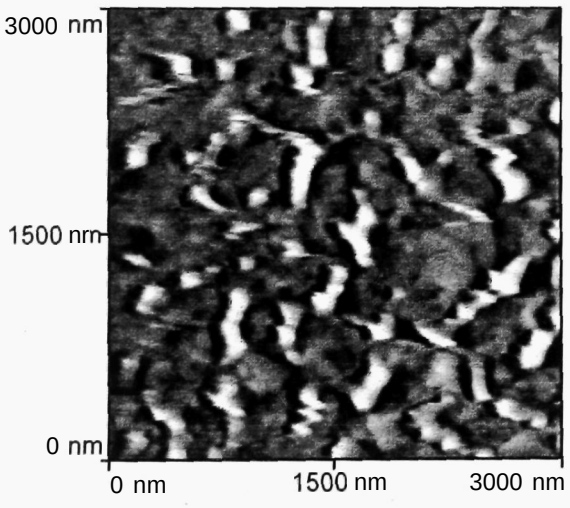


(f) 67 min

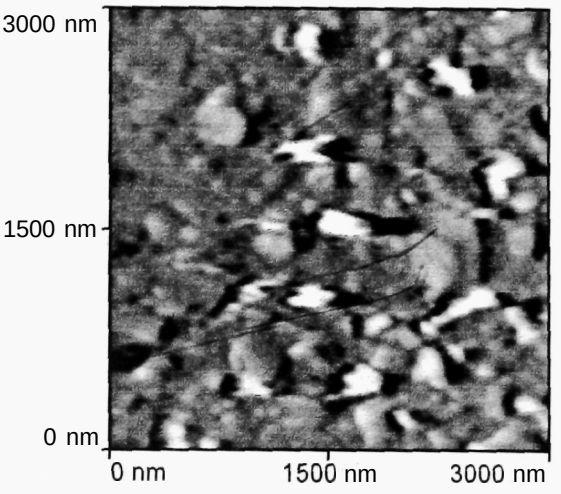


Figure 6.4 (continued)

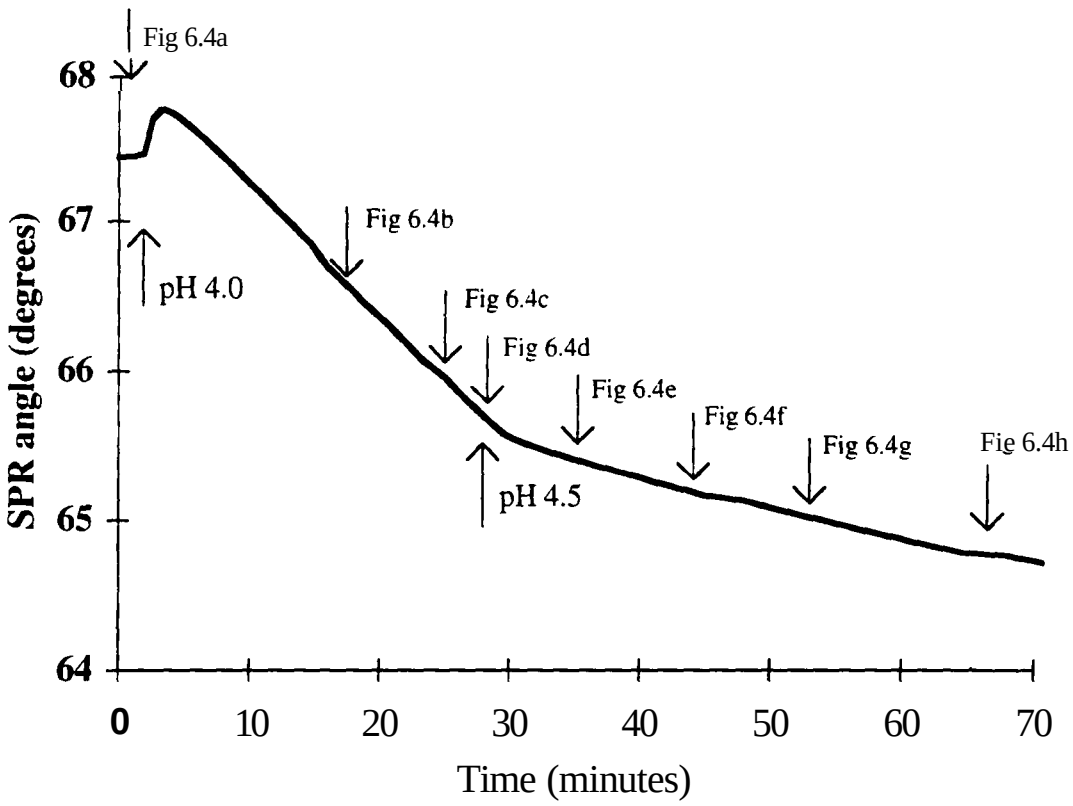


Figure 6.5 SPR data showing the change in $\theta_{SPR}$ against time. The arrows indicate the time at which the simultaneously acquired AFM images (shown in Figure 6.4) were recorded.

At t = 30 min, the pH of the HCl solution was decreased from 4.0 to 4.5. The SPR data clearly demonstrated the slowing in the rate of polymer erosion as a result of the pH change with the rate of decrease of $\theta_{SPR}$ measured at $0.021^{\circ}min^{-1}$. The AFM data recorded over this period showed the exhaustion of the polymer as the pits in the film continued to expand.

One problem that has to be addressed when analyzing simultaneously acquired AFM/SPR data is the differences in the time at which the complete loss of the polymer film was recorded. In the example shown in Figure 6.4 and 6.5, the AFM data appeared to show complete film removal after approximately 57 min, whilst the SPR angle continued to fall after this period. The explanation of this lies in the difference in the sample areas analyzed by the two techniques. The AFM analyses a surface area of the sample of 9 $\mu m^2$ compared to an estimated area of 5000 $\mu m^2$ analyzed by SPR (127). Therefore, the SPR data will tend to average out any heterogeneity in the rate of film removal across the sample surface. This explanation is supported by repeats of this degradation experiment in which the surface changes recorded by AFM have been found to occur at both quicker and slower rates than the changes recorded by SPR.

This example of analyzing the erosion of a DETOSU 1,5 pentanediol film represents the first example of the implementation of the combined AFM/SPR to investigate a dynamic solid-liquid interfacial change. The information obtained shows that on a simple homopolymer system, the combined instmment can determine the effect of pH on the kinetics of polymer degradation and it can visualize the mechanism by which polymer material is removed from the surface. In the next section, the combined instrument is applied to the PSA/PLA immiscible blends which were first introduced in Chapter 4. The aim of these studies was to investigate if the morphological changes visualized during erosion by the AFM could be related to the kinetics of film degradation recorded by the SPR.

### 6.3.3 Analysis of PSA/PLA Blends

#### 6.3.3.1 Analysis of single component films

The two polymers used to form the immiscible blends are known to display very different hydrolytic susceptibilities within alkaline conditions (180). As a first stage of the combined AFM/SPR analysis the effect of these susceptibilities on degradation of single component polymer films was investigated.

The AFM and SPR data recorded during the degradation of a PSA film exposed to a pH 11 KCl/NaOH buffer is displayed in Figures 6.6 and 6.7 respectively. The four AFM images show the topographical changes occurring to a 3 μm X 3 μm area of the sample. On the simultaneously acquired SPR data, the time at which each AFM image was recorded is again indicated by a labelled arrow.

Initially, the PSA film was characterized before degradation with the liquid cell filled with pH 7 water. The AFM image displayed in Figure 6.6a shows the expected fibrous morphology of the PSA film at t = 0 min with fibres possessing diameters of between 50 and 300 nm. The presence of the PSA film on the SPR sensor caused $\theta_{SPR}$ to shift from 64.9° for the uncoated silver to a value of 68.4°.

The degradation experiment was started by initiating the pumping of the pH 11 buffer into the Uquid cell. For a period of approximately 10 min after the start of pumping $\theta_{SPR}$ was unchanged due to the lag time corresponding to the time required for the buffer to travel from the syringe to the liquid cell and displace the water. As the buffer displaced the water, there was a slight increase in GSPR from 68.4° to 68.7°, due to the detection of an increase in the ionic concentration of the fluid in the liquid ceU. At t = 11 min, the effect of polymer degradation became dominant and GSPR decreased rapidly at a rate of $0.163°min^{-1}$ for a period of 10 minutes. During this 10 min period, the AFM image in Figure 6.6b was recorded. This image displayed the start of the erosion of the film and in particular, the breakdown of the fibrous surface stmcture.

(a) 0 min

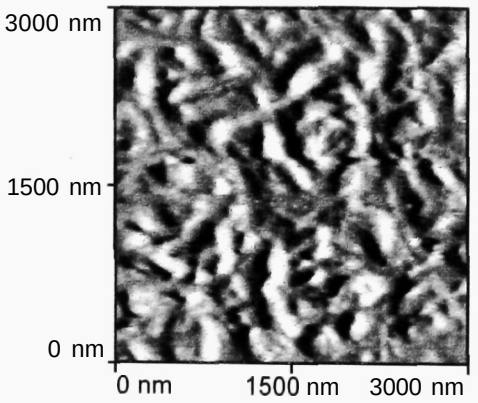


(b) 21 min

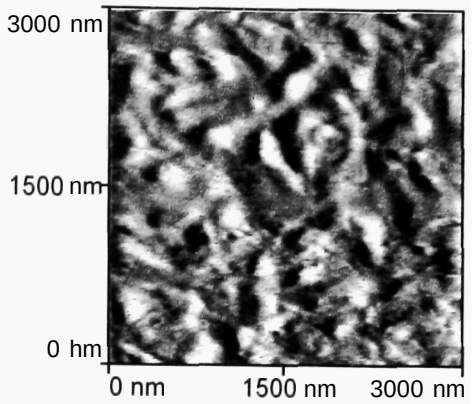


(c) 30 min

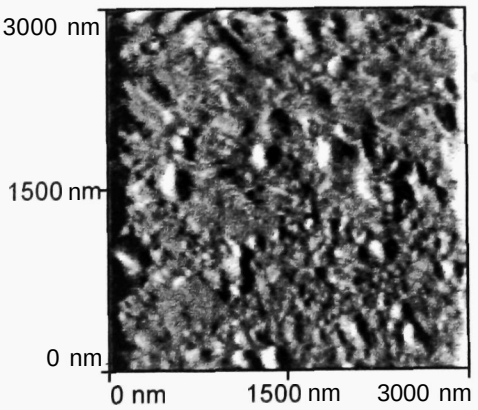


(d) 40 min

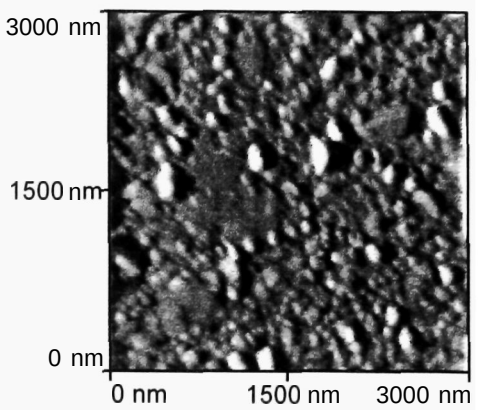


Figure 6.6 AFM analysis of the degradation of a PSA film in a pH 11 buffer. P = 6, I = 1,D=1.

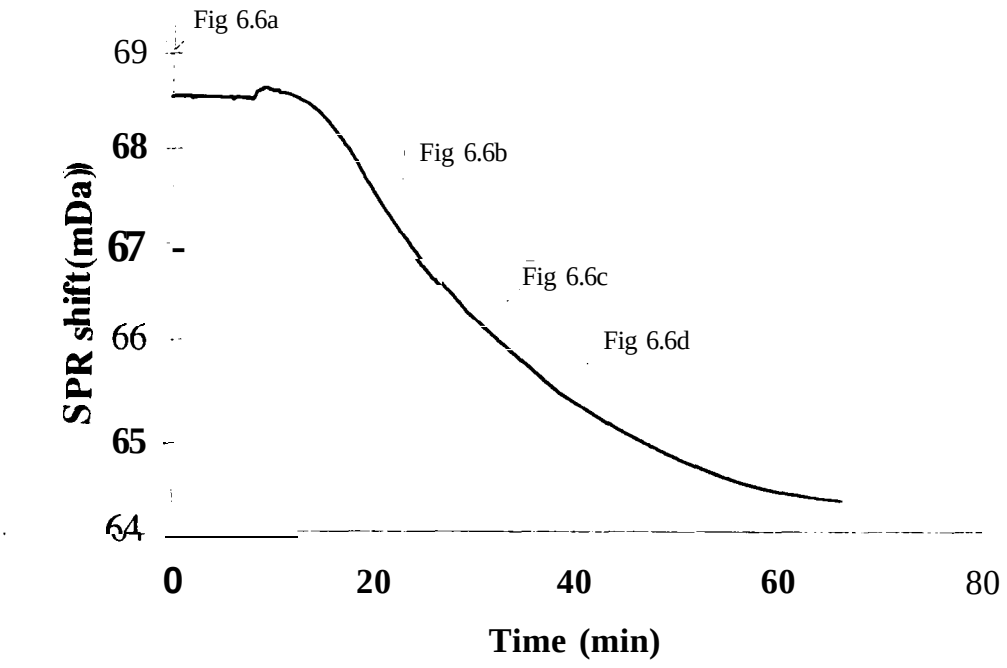


Figure 6.7 SPR data acquired simultaneously with the AFM data in Figure 6.6 during the degradation of a PSA film in a pH 11 buffer. The arrows indicate the times at which the AFM data was recorded.

The next stage in the SPR data showed a reduction in the rate of decrease of $\theta_{SPR}$ until, after 65 minutes of the experiment, $\theta_{SPR}$ maintained a constant value of 64.2°, a value which would be expected for the silver film of an uncoated SPR sensor. AFM images recorded during this period (Figures 6.6c and d) show the loss of the PSA film from the SPR sensor. The exposure of the silver surface with the characteristic particulate stmcture can be seen in these images.

Therefore, in the analysis of the degradation of the PSA film, the AFM/SPR instrument recorded the rapid loss of the film as a result of hydrolysis. The initial rapid rate of decrease of $\theta_{SPR}$ occurred when the polymer film completely covered the SPR sensor surface. Then, as this complete coverage was lost, the rate of erosion slowed due to the decrease in the polymer surface area, and hence, the reduction of the number of sites available for hydrolytic attack.

The analysis of the degradation of the single component PLA film emphasised the differences in the rates of hydrolysis of PSA and PLA. The AFM and SPR data for PLA is displayed in Figures 6.8 and 6.9 respectively. The AFM recorded surface morphology of the PLA film displayed the smooth nature of the surface at this scale that is typical of a spun cast film of a low crystallinity polymer. The value of $\theta_{SPR}$ recorded for this film was 70.1°. The contrast between the rates of degradation of the PLA and the PSA is apparent from the SPR data in Figure 6.9. For the PLA degradation the rate of GSPR decrease was found to be $0.001\ °min^{-1}$ and after 160 minutes degradation GSPR was lowered by ordy 0.22° in total. The AFM data recorded simultaneously over this period of time demonstrated no changes in surface morphology.

### 6.3.3.2 Analysis of PSA/PLA Blend

The fu-st step in the characterization of the degradation of these PSA/PLA blends was to consider the effect of the blend composition on the AFM recorded surface morphology. The three AFM images in Figure 6.10 show the surface morphology of the 70%: 30%, 50%: 50% and 30%: 70% PSA:PLA blends

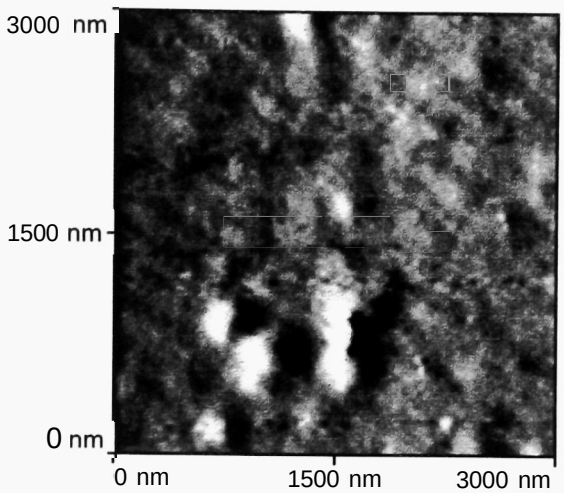


Figure 6.8 AFM analysis of the morphology of a PLA film in a pH 11 buffer. P= 1, I = 0.5, D = 0.1.

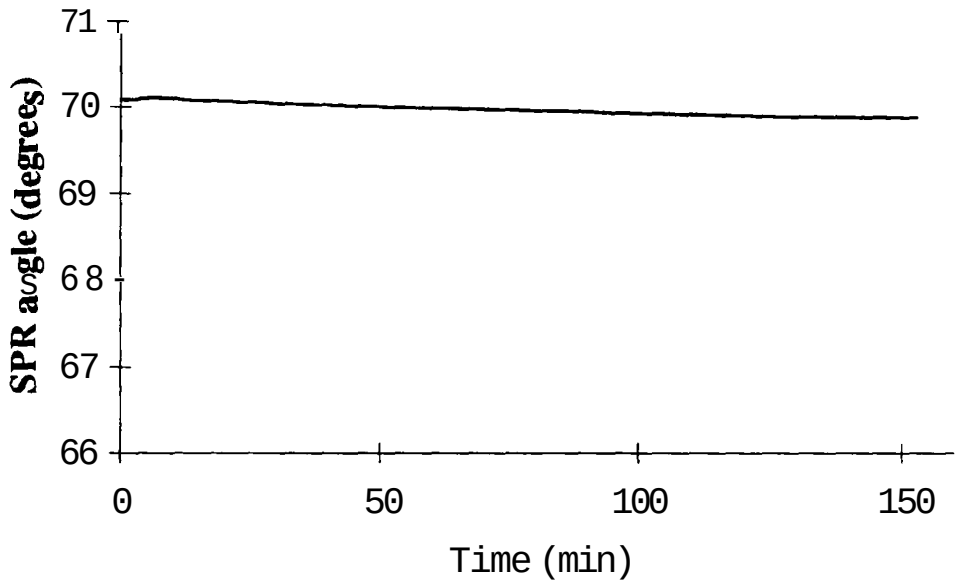


Figure 6.9 SPR data acquired simultaneously witii the AFM data in Figure 6.8 during the degradation of PLA film in a pH 11 buffer. The arrows indicate the times at which tiie AFM data was recorded.

(a) 70% PSA: 30% PLA

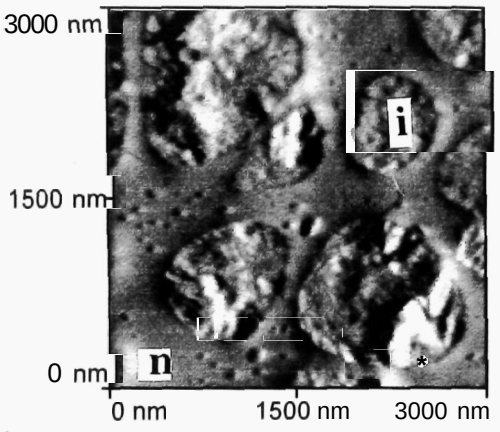


(b) 50% PSA: 50% PLA

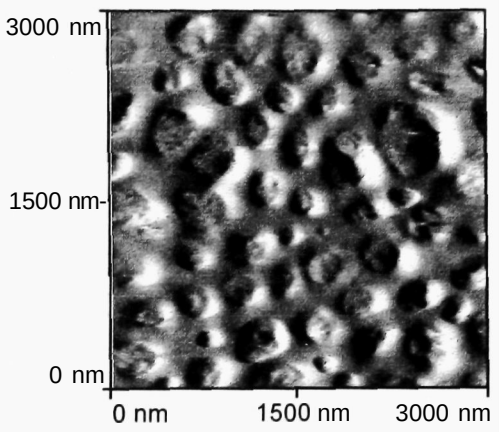


(c) 30% PSA: 70% PLA

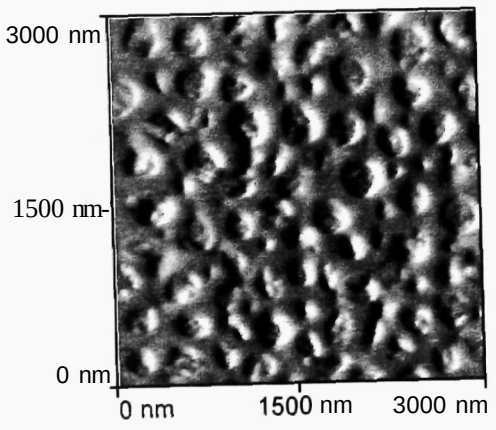


Figure 6.10 3 μm x 3 μm AFM images of the initial surface morphology of PSA/PLA blends with compositions of (a) 70%: 30%, (b) 50%: 50% and (c) 30%: 70%. Areas marked n represent the network stmcmre of the PLA component and areas marked i represent the island structures of the PSA component P = 1, I = 0.5, D = 0.1

prior to degradation. All three images show the phase separated morphologies of these films, with a continuous network of one component (marked n) and isolated islands of the other component (marked i). As the proportion of PSA in the blend decreased, the size of the isolated islands shrank, indicating that the PSA formed the islands in the network of the PLA. These blend samples, which were spun cast onto the silver surface of the SPR sensors, display a slightly different morphology to the blends described in Chapter 4 (section 4.3.2) which were spun cast onto mica substrates. The major difference is that for the SPR sensor samples the PLA is always the continuous network phase whereas, when mica was the substrate, the PLA formed isolated islands for the 70% PSA: 30% PLA sample. This difference may be caused by the change in substrate or the greater volume of polymer solution used to prepare the SPR slide samples (100 μl, see section 2.2.3) compared to the mica substrate samples (10 μl, see section 4.2.2). The greater volume was used because the SPR slides are approximately 2 cm wide and, therefore, more polymer solution is required to generate a complete coverage of the substrate by the polymer blend.

After each sample was imaged to analyse the initial surface morphology, surface erosion was initiated in the pH 11 buffer. Considering first, the combined data for the 70:30 PSA/PLA blend. The dynamic surface topography changes occurring during degradation are displayed in the eight AFM images in Figure 6.11 and the corresponding shift in GSPR with time is plotted in Figure 6.12 with the times of acquisition of the AFM data again indicated with labelled arrows.

After the initial lag phase, there was a period of rapid decrease of GSPR. The decrease reached a maximum rate of $0.170°min^{-1}$ between t = 15 and 37 min and during this period GSPR fell by 3.32°. This rate is very similar to the rate recorded for the single component PSA film. During this period, the AFM images in Figures 6.11b, c and d were recorded. These images recorded the loss of polymeric material from the islands, i.e. the removal of PSA material. This removal resulted in the formation of pits which increased the prominence of the PLA network as highlighted by the cross-sections displayed in Figure 6.13. In the AFM image in Figure 6.11d, the topography of the underlying

(a) 0 min

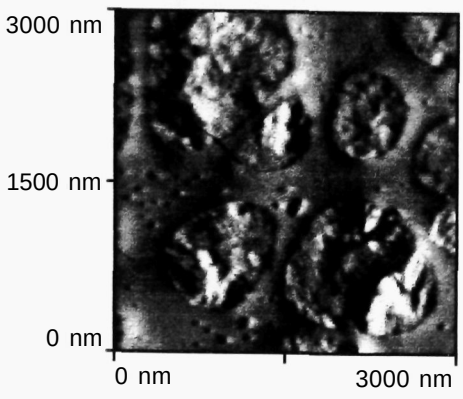


(b) 21 min

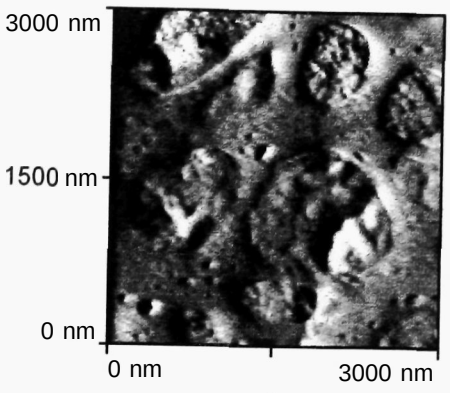


(c) 30 min

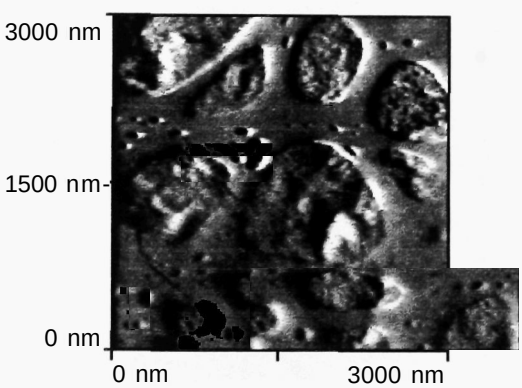


(d) 40 min

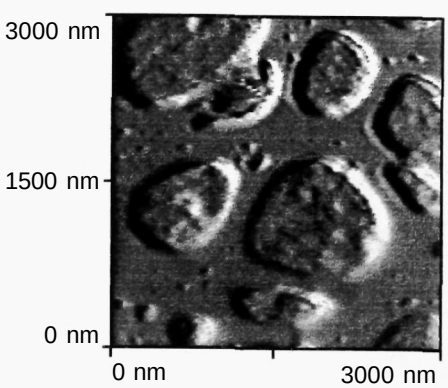


Figure 6.11 Eight AFM images visualizing the effect of degradation on the topography of the 70% PSA: 30 % PLA blend. P = 1, I = 0.5, D = 0.1.

(e) 60 min

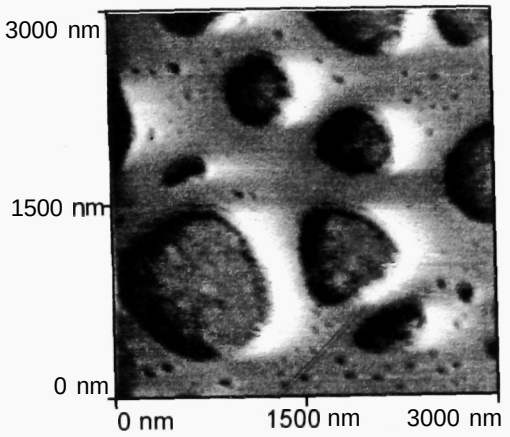


(f) 90 min

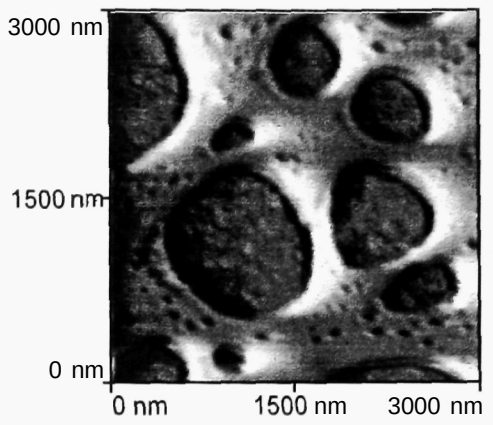


(g) 120 min

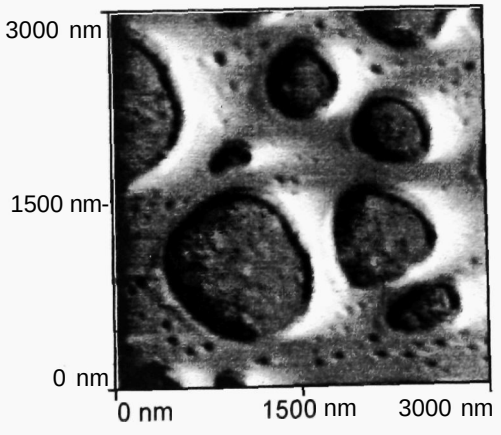


(h) 180 min

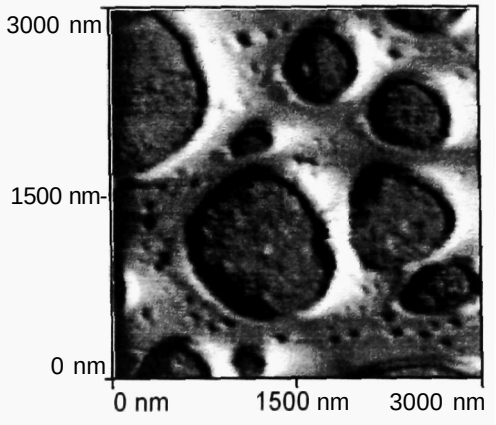


Figure 6.11 (continued)

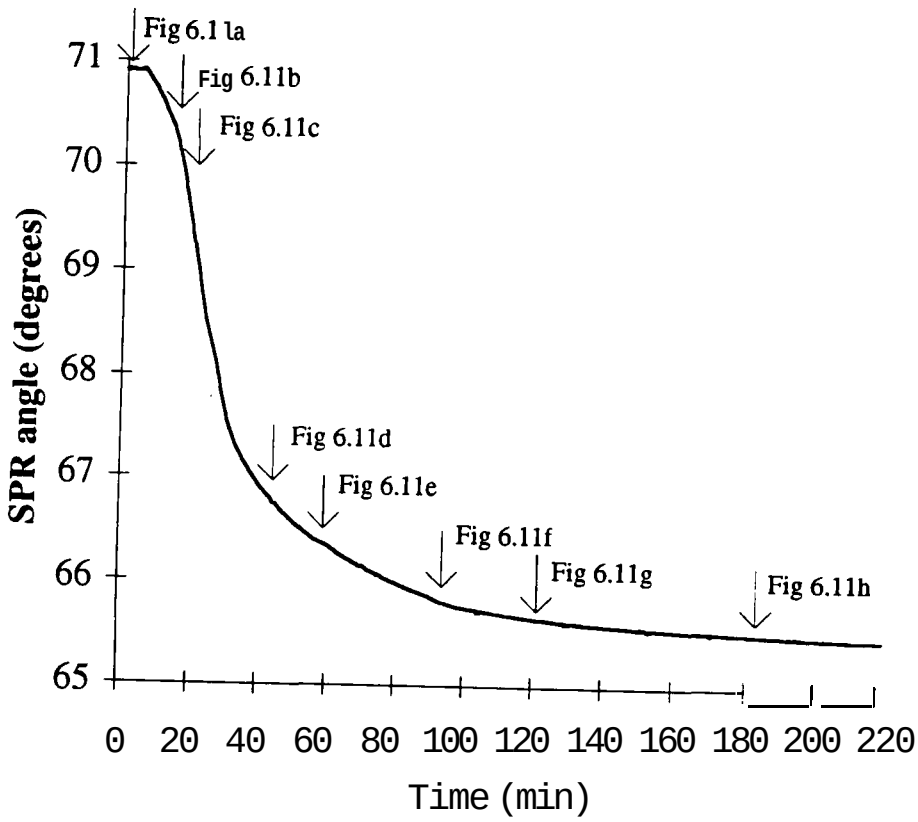


Figure 6.12 SPR data showing the change in $\theta_{SPR}$ on exposure of the 70 % PSA: 30% PLA blend to a pH 11 buffer. The arrows indicate the times at which the images in Figure 6.11 were acquired.

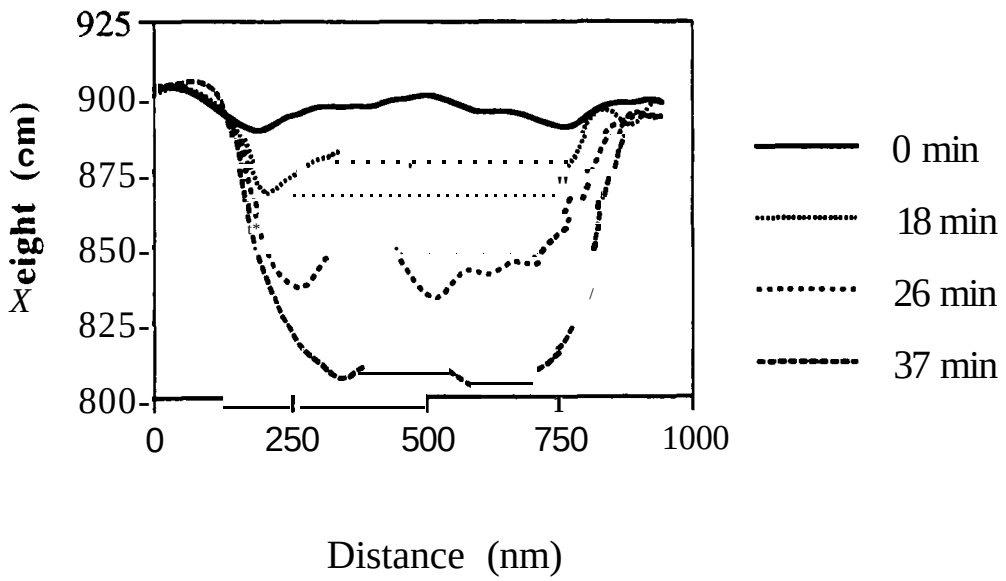


Figure 6.13 Cross-sectional analysis of the preferential erosion of PSA resulting in the exposure of the PLA network.

silver surface of the SPR sensor became apparent on those areas not covered by the PLA network. Clearly, both the AFM and SPR data indicate the removal of PSA material in the first 40 minutes of exposure to the pH 11 environment.

After the initial rapid rate of decrease of GSPR, there was a deceleration period. This deceleration is expected due to the decreased surface area of the PSA available for degradation as the SPR sensor surface was exposed. However, the rate of GSPR decrease does not fall to zero as observed for the single component PSA film (Figure 6.7). Instead, over a period of 140 min, the rate of shift slowly fell from $0.04°min^{-1}$ at t = 40 min to $0.001°.min^{-1}$ at t = 180 min. The AFM images recorded during this period are displayed in Figures 6.11e to h (it should be noted that the image area analyzed in these Figures has moved slightly from the area in the first four images due to a readjustment of the AFM cantilever setup at t=40 min). The topographs show that small changes occurred to the network structure as degradation progressed. The most noticeable stmctural change was a widening of the pits as the polymer network shrank. However, it is clear that the rate of degradation had slowed considerably compared with the early phase of PSA removal. The interesting aspect of this period of film degradation is that the SPR data indicates that the hydrolytic removal of polymeric material occurred at a rate which is intermediate to that recorded for the single component films. It appears, therefore, that the blending of these polymers achieved the objective of generating new materials with characteristics moderated by the two components. The mechanism by which this intermediate rate of degradation was achieved has not been elucidated. However, it is possible that PLA protected the remaining PSA material. This mechanism was previously proposed in Chapter 4 were the tendency for the PLA material to preferentially reside at the surface of these blended films as indicated by SSIMS and XPS studies was introduced (220).

At the end of this degradation experiment, the rate of SPR angle shift was $0.0005°min^{-1}$, which is consistent with the degradation of a pure PLA film given the decrease in surface area of a network compared with a complete film. Therefore, from the AFM/SPR data three stages in the degradation of the

PSA:PLA 70:30 blend films can be identified. Initially, there was a rapid loss of PSA islands. This was followed by a long intermediate stage during which film removal occurred slower than the rate expected for PSA and faster than the rate for PLA. Finally, the degradation profile reflected the loss of pure PLA material.

The next step in the analysis of these blends was to further explore the nature of this intermediate stage by analyzing films containing higher proportions of PLA. The AFM and SPR data recorded during the degradation of a 30% PSA: 70% PLA film are displayed in Figures 6.14 and 6.15 respectively. The AFM images demonstrated a similar general pattern of degradation as observed in the 70% PSA: 30% PLA blend, with an initial erosion of the PSA islands leaving the PLA network structure exposed. The SPR data in Figure 6.15 shows the effect of degradation on $\theta_{SPR}$ over a 250 min period. Initially, once the pH 11 buffer had displaced the water, there was a period of relatively rapid decrease in GSPR as the PSA material was removed. The maximum rate of SPR angle shift was $0.118°.min^{-1}$ which is lower than the maximal values for both the single component PSA film and the high PSA composition blend. This may be expected due to the relatively small area of the PSA islands at the surface of this film. Over the next 220 min of the experiment, the rate of GSPR decrease underwent a slow deceleration. However, the deceleration was considerably slower than that recorded for the 70% PSA: 30% PLA blend and when the experiment was terminated after 250 minutes, the rate of $\theta_{SPR}$ decrease was still $0.004°min^{-1}$.

This study indicates that as the relative proportion of PLA in the blend was increased, the intermediate phase in the degradation of the film was greatly extended. We also performed AFM/SPR analysis on a 50% PSA: 50% PLA blend. The SPR data is displayed in Figure 6.16. Again, the pattern of degradation displayed the three distinct stages. As expected, the time for each phase and the rate of fall in GSPR are midway between the values for the 70% PSA: 30% PLA and the 30% PSA: 70% PLA films.

(a) 0 min

(b) 40 min

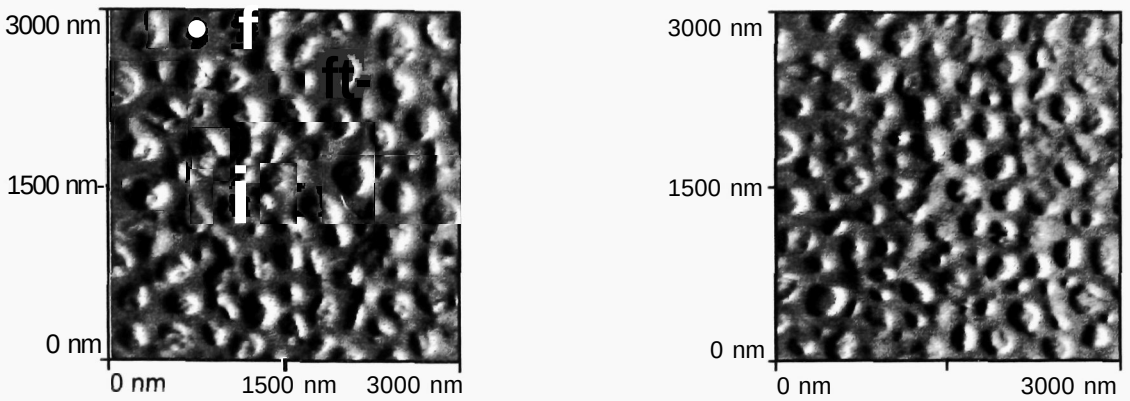


(c) 180 min

(d) 240 min

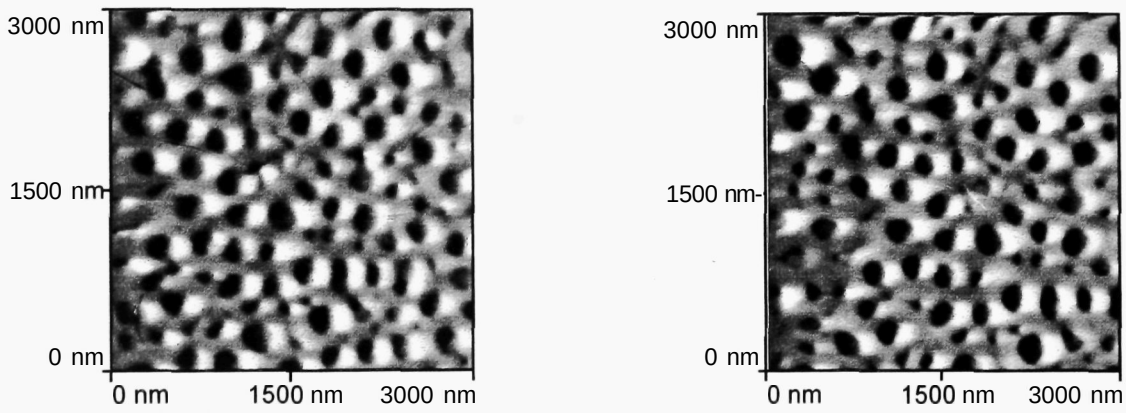


Figure 6.14 AFM data recorded during the surface erosion of the 30% PSA: 70% PLA in a pH 11 buffer.

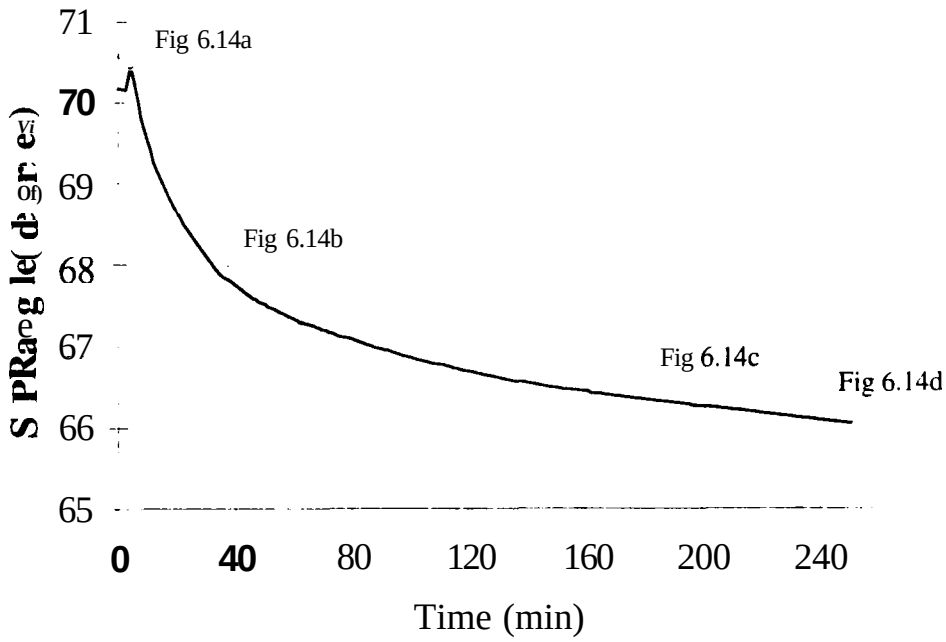


Figure 6.15 SPR data recorded during the surface erosion of the 30% PSA: 70% PLA in a pH 11 buffer.

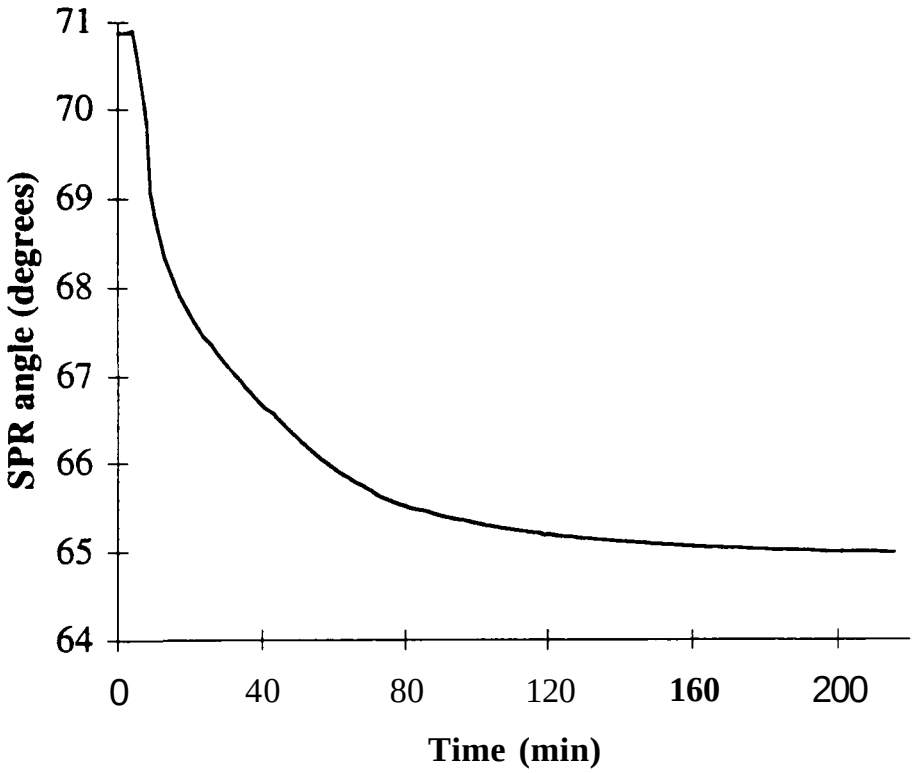


Figure 6.16 SPR analysis of degradation of a 50% PSA:50% PLA blend in a pH 11 buffer.

## 6.4 Conclusions

The experiments described in this Chapter represent the first examples of the implementation of the combined AFM/SPR instrument to analyse a dynamic surface change occurring at a solid/liquid interface. The instmment has been shown to yield new information on the surface erosion of biodegradable polymer systems. In particular, the AFM data provides information on the heterogeneity of surface erosion on the sub-micron length scale, whilst the SPR data can explain the effect of this heterogeniety on the erosion kinetics for the complete polymer film.

The benefits of constructing a combined instrument, capable of generating simultaneous AFM and SPR data from a degradable system, are highlighted by the studies of the PSA/PLA immiscible blends. The AFM images visualize the importance of the phase separation of the two polymers and the resulting rapid loss of the PSA islands. However, considered in isolation, the AFM images did not provide a complete picture of the complexity of the kinetics of surface erosion. This complexity was shown by the three stages evident in the SPR data. It can be argued that the AFM and SPR data is synergistic in nature because the three stages of erosion in the SPR data would be difficult to interpret without the evidence of phase separation and morphological changes shown in the AFM data.

There remain a number of limitations in the application of the combined AFM/SPR which are the subject of ongoing studies within the Laboratory of Biophysics and Surface Analysis. The non-linearity of the change in $\theta_{SPR}$ is a concem if the precise change in thickness of a biodegradable film during erosion is to be measured. This limitation does not prohibit the SPR from measuring major differences in erosion kinetics, as seen when PSA and PLA are mixed, but at present the interpretation of the kinetics of erosion can only be expressed as changes in the value of GSPR.

# Chapter 7 Final Conclusions

Polymeric biomaterials are expected to perform increasingly complex functions within the body. For example, dmg delivery systems for protein and peptide dmgs are required to protect diese labile molecules for extended periods and then release them over a predetermined timescale to produce a dierapeutic effect. Biocompatible implants and cell adhesion templates are required to interact with certain proteins and cell types whilst repelling others to permit residence times with the body to match the desired Ufetime of the biomaterial. To achieve these functions it is necessary to provide methods of analyzing the precise surface characteristics of polymeric biomaterials. This, in tum, will improve the prediction of the interactions occurring at the interface between the biomaterial and the patient.The work presented in this thesis describes one aspect of this surface analysis, the apphcation of atomic force microscopy techniques.

The progression of the type of data acquired from polymeric biomaterials in the four experimental Chapters reflects improvements in the specifications of atomic force microscopes avaUable during the studies. In Chapter 3, the studies explored the high resolution capability of the AFM and the potential to utilize this resolution to augment current microscopy methods for polymers. The experiments performed on poly(ethylene oxide) demonstrated that the lamellar organization of sphemlites, single crystals and dendrites could be visualized without sample preparation techniques to improve the electron conductivity or increase vertical height changes across the polymer samples. The studies also demonstrated the visualization of single molecules of poly(ethylene oxide) deposited on an atomically flat substrate. The potential application of these methods within biomaterial research lies in the ability to characterize the influence of polymer chemical stmcture and device fabrication methods on the molecular organization of surfaces.

In Chapters 4,5 and 6, the ability to image polymer surfaces within aqueous conditions was harnessed to study the dynamic interfacial phenomenon of polymer degradation. Initially, the work in Chapter 4 concentrated on identifying the influence of surface morphology on erosion. Then, the release of a protein dmg from a biodegradable polymer fdm was visualized in Chapter 5. This work provided a new insight into the relationship between polymer erosion

and dmg dissolution. The studies in Chapter 5 also introduced the concept of measuring erosion and release kinetics with the AFM. The computational methods in Chapter 5 allowed relative rates of erosion of protein and polymer areas to be measured and tiiis highlighted the different dissolution behaviour of certain protein particles. The theme of measuring erosion kinetics was extended in Chapter 6 with the introduction of the combined AFM/SPR. This mstmment provided a technique for relating sub-micron changes in film morphology during erosion to the kinetics of polymer degradation.

The methods described for analyzing polymer degradation appear to have considerable potential for the rapid characterization of novel series of biodegradable polymers. The development of the polyanhydrides provides a good example of project that could benefit from *in situ* AFM and simultaneous AFM/SPR studies. In the early design of the polyanhydrides the central method of controlling the kinetics of polymer hydrolysis was to change the number of methylene groups in the polymer backbone and, hence, change the hydrophobicity of the material. The standard mediod of quantifymg the effect of these chemical changes was to measure the change in weight of a polymer matrix over a number of weeks. AFM/SPR analysis could provide a quicker method of determining the effect of chemical changes on degradation and simultaneous identify problems relating to the crystaUinity of homopolymers or the immiscibiUty of blends.

Finally, the three years during which these studies have been performed, have witnessed a number of significant developments in scanning probe microscopy, such as near-field optical microscopy, non-contact AFM imaging modes and spectroscopic techniques. Each of these techniques can generate new information on the surface organization of polymeric biomaterials and, therefore, could offer new methods of characterizing the complex interactions which underUe successful functioning.

## References


(1) New challenges in biomaterials.
Peppas N.A and Langer R., *Science,* **263,** 1715-1720, 1994.

(2) Hydrogel and general properties of biomaterials.
Dumitriu S. and Dumitriu-Medvichi C, in *Polymeric Biomaterials,* ed. Dumitriu S., Marcel Dekker, Inc., New York, 1994, pp.3-98.

(3) BiofunctionaUty and biocompatibiUty.
WUUams D.F., in *Materials Science and Technology 14, Medical and Dental Materials,* ed. Cahn R.W., Haasen P. and Kramer E. J., Volume 1, ed. WiUiams D.F., VCH Germany, 1992, pp. 1-27.

(4) Innovations and deviations in therapeutic vascular devices.
Paris E., King M.W., Guidoin R.G., Delorme J-M., Deng X. and Douville Y., in *Polymeric Biomaterials,* ed. Dumitriu S., Marcel Dekker, Inc., New York, 1994, pp.3-98.

(5) The evolution of artificial heart valves.
Collins Jr. J. J., *The New England Journal of Medicine,* **324,** 624-626, 1991.

(6) Moisture diffusivity of biomer versus biomer-coated polyisobutylene polyurethane urea (PIB-PUU) - a potential blood sac material for the artificial-heart
Yeh J., Gordon B. and Rosenberg G., *Journal of Materials Science Letters,* **13,** 1390-1391, 1994.

(7) New prospects for a prolonged functional Ufe-span of artificial hip joints by using the material combination of polyethylene-aluminium oxide ceramic-metal.
Semlitsch M., Lehman M., Weter H., Dorre E. and Wilier H.G., *Journal of Biomedical Materials Research,* **11, 537-543, 1977.**

(8) Implants in plastic and reconstmctive surgery.
Maisels D.O., in *Implants in Surgery,* ed. WiUiams D.F. and Roaf R., London, 1973, pp.537-588.

(9) Wound tissue can utilize a polymeric template to synthesize a functional extension of skin.
Yannas I.V., Burke J.F., Orgill D.P. and Skrabut E.M., *Science,* **215,** 174-176, 1982.

(10) Review: Tissue engineering in the nervous system.
Bellamkonda R. and Aebischer P., *Biotechnology and Bioengineering,* **43,** 543-554, 1994.

(11) Dialysis in acute-renal failure - which membrane?
Mutais S.K., Ivanovich P. and Vidovich M.I., *Artificial Organs,* 18, 470-472, 1994.

(12) Urinary tract prostheses and tiieir biocompatibiUty.
Holmes S.A.V., Kirby R.S. and Whitfield H.N., *British Journal of*

*Urology,* 71, 378-383, 1993.

(13) New methods of dmg delivery.
Langer R., *Science*, **249**, 1527-1533, 1990.

(14) Transdermal dmg delivery: Problems and possibiUties.
Knepp V.M., Hadgraft J. and Guy R.H., *Critical Reviews in Therapeutic Drug Carrier Systems,* 4, 13-37, 1987.

(15) Polymers for absorbable surgical sutures .1.
Benicewicz B.C. and Hopper P.K., *Journal of Bioactive and Compatibile Polymers,* 5, 453-472, 1990.

(16) Intraocular lenses: Evolution, designs, complications and pathology.
Apple D.J., Mamalis N., Olson R.J. and Kincaid M.C, WUUams & WiUdns, Baltimore, 1989.

(17) Encyclopedia of medical and dental materials.
ed. Williams D.E, Pergamon, Oxford, 1990.

(18) Physical properties of polymers.
Mark J.E., Eisenberg A., Graessley W.W., Mandelkern L., Samulski E.T., Koenig J.L. and Wignall G.D., ACS Professional Reference Book, Washington D.C., 1993.

(19) Defmtions in biocompatibility.
WilUams D.F., Elsevier, Amsterdam, 1987.

(20) Modem aspects of protein adsorption on biomaterials.
Missirlis Y.F. and Lemm W., Kluwer Academic Publishers, Dordrecht 1989.

(21) Molecular bioengineering of biomaterials in the 1990's and beyond: A growing liason of polymers with molecular biology.
Hoffman A.S., *Artificial Organs,* 16, 43-49, 1992.

(22) Polymer surfaces from physics to technology.
Garbassi F., Morra M. and OcchieUo E., John Wiley & Sons, Chichester, 1994.

(23) Biomolecules and surfaces.
Ramer B.D., Castner D.G., Horbett T.A., Lenk T.J., Lewis K.B. and Rapoza R.J., *Journal of Vacuum Science and Technology,* A8, 2306-2317, 1990.

(24) Polymer interfaces on a molecular scale: Comparision of techniques and some examples.
Stamm M., *Advances in Polymer Science,* **100,** 357-400, 1992.

(25) Characterization of biomaterial surfaces.
Ramer B.D., *Cardiovascular Pathology, 2,* 875-1005, 1993.

(26) Surface characterization of biomaterials by electron spectroscopy for chemical analysis.
Ramer B.D., *Annals of Biomedical Engineering,* 11, 313-336, 1983.

(27) Polymer surface characterization by XPS and SIMS.
Briggs D., in *Characterization of Solid Polymers New Techniques and Developments,* ed. SpeUs S.J., Chapman & Hall, London, 1994.

(28) Static secondary ion mass spectrometry of polymeric biomaterials.
Davies M.C. and Lynn R.A.P., *Critical Reveiws in Biocompatibility, S,* 297-341, 1990.

(29) Secondary ion imaging of heterogeneous organic polymer films.
Simko S.J., Bryan S.R., Griffis D.P., Murray R.W. and Linton R.W., *Analytical Chemistry,* 57, 1198-1202, 1985.

(30) Surface infrared spectroscopy.
Knutson K. and Lyman D.J., in *Surface and Interfacial Aspects of Biomedical Polymers,* ed. Andrade J.D., Plenum Press, New York, 1985, chapter 6.

(31) Comparison of attenuated total reflectance and photoacoustic sampling for surface analysis of polymer mixtures by fourier transform infrared spectroscopy.
Gardella J.A., Grobe III G.L., Hopson W.L. and Eyring E.M., *Analytical Chemistry,* 56, 1169-1177, 1984.

(32) Evaluation of dmg deUvery systems by electron microscopy techniques.
Pathak Y.V. and Labhashetwar V.D., *Cells and Materials,* 3, 51-66, 1993.

(33) Chemical and physical-properties of coUagen implants influence their fate in-vivo as evaluated by light and confocal microscopy.
Vardaxis N.J., Ruijgrok J.M., Rietveld D.C., Marres E.M. and Boon M.E., *Journal of Biomedical Materials Research,* 28, 1013-1025, 1994.

(34) Photon tunneling microscopy of polymeric surfaces.
Guerra J.M., Smivasarao M. and Stein R.S., *Science,* 262, 1395-1400, 1993.

(35) The contact angle and interface energetics.
Andrade J.D., Smith L.M. and Gregonis D.E., in *Surface and Interfacial Aspects of Biomedical Polymers,* ed. Andrade J.D., Plenum Press, New York, 1985, chapter 7.

(36) Observation of surface rearrangement of polymers using ESCA.
Lewis K.B. and Ramer B.D., *Journal of Colloid and Interface Science,* 159, 77-85, 1993.

(37) Electi-on microscopy and sphemUtic organization in polymers.
Bassett D.C, *CRC Critical Reviews in Solid State and Materials Science,* 12, 97-165, 1984.

(38) Surface studies by scanning tunneling microscopy.
Binnig G., Rohrer H., Gerber Ch. and Weibel E., *Physical Review Letters, 49,* 57-61, 1982.

(39) Surface electronic stmcmre of Si(l 1 l)-(7x7) resolved in real space.

Hamers R.J., Tromp R.M. and Demuth J.E., *Physical Review Letters,* 56, 1972-1975, 1986.

(40) Biological applications of the scanning probe microscope.
Lindsay S.M., in *Scanning Tunneling Microscopy and Spectroscopy Theory, Techniques and Applications,* ed. BonneU D.A., VCH Publishers Inc., New York, 1993.

(41) Atomic force microscopy and scanning tunneUng microscopy: refmüig techniques for studying biomolecules.
Roberts C.J., WiUiams P.M., Davies M.C, Jackson D.E. and Tendler S.J.B., *Trends in Biotechnology,* 12, 127-130, 1994.

(42) Atomic force microscope.
Binnig G., Quate CF. and Gerber Ch., *Physical Review Letters,* 56, 930-933, 1986.

(43) Contact faces of epitaxiaUy crystalUzed a- and γ phase isotactic polypropylene observed by atomic force microscopy.
Stocker W., Magonov S.N., Cantow H.J., Wittinan J.C. and Lotz B., *Macromolecules,* 26, 5915-5923, 1993.

(44) STM and AFM studies of biomaterials at a Uquid-soUd interface.
Lindsay S.M., Lyubchenko Y.L., Tao N.J., Li Y.Q., Oden P.I. and DeRose J.A., *Journal of Vacuum Science and Technology,* **All,** 808-815, 1993.

(45) Imaging crystals, polymers and processes in water with the AFM.
Drake B., Prater C.B., Weisenhom A.L., Gould S.A.C., Albrecht T.R., Quate C.F., CanneU D.S., Hansma H.G. and Hansma P.K., *Science* , **243**,1586-1589, 1989.

(46) Improved atomic force microscope images using microcantUevers with sharp tips.
Akamine S., Barrett R.C and Quate C.F., *Applied Physics Letters,* 57, 316-318, 1990.

(47) Novel optical approach to atomic force microscopy.
Meyer G. and Amer N.M., *Applied Physics Letters,* 53, 1045-1047, 1988.

(48) Interpretation issues in force microscopy.
Bumham N.A., Colton R.J. and PoUock H.M., *Journal of Vacuum Science and Technology,* A9, 2548-2556, 1991.

(49) Atomic force microscopy using optical interferometry.
Eriandsson R., McClelland G.M., Male CM. and Chiang S., *Journal of Vacuum Science and Technology,* A6, 266-270, 1988.

(50) Force microscopy with a bidirectional capacitance sensor.
Neubauer G., Cohen S.R., McCleUand G.M., Home D. and Mate CM., *Review of Scientific Instruments,* 61, 2296-2308, 1990.

(51) Piezoresistive strain sensor.
Tortonese M., Ban-ett R.C. and Quate C.F., *Applied Physics Letters,*

62, 834-836, 1993.

(52) Orientational ordering of polymers by atomic force microscope tip-surface interaction.
Leung O.M. and Goh M.C, *Science,* **255,** 64-66, 1992.

(53) Atomic force microscope - force mapping and profiting on a sub 100 Ang scale.
Martin Y., WUUams CC and Wickramasinghe H.K., *Journal of Applied Physics,* 61, 4723-4729, 1987.

(54) Force microscopy.
Bumham N.A. and Colton R.J., in *Scanning Tunneling Microscopy arui Spectroscopy Theory, Techniques and Applications,* ed. BonneU D.A., VCH Publishers Inc., New York, 1993.

(55) Tapping mode atomic force microscopy in liquids.
Hansma P.K., Cleveland J.P., Radmacher M., Walters D.A., HiUier P.E., Bezanilla M., Fritz M., Vie D., Hansma H.G., CB. Prater C.B., Massie J., Fukunaga L., Guriey J. and Elings V., *Applied Physics Letters,* 64, 1738-1740, 1994.

(56) Friction measurement on phase separated thin fihns with a modified atomic force microscope.
Ovemey R.M., Meyer E., Frommer J., Brodbeck D., Lüthi R., Howald L., Giintherodt H.-J., Fujihira M., Takano H. and Gotoh Y., *Nature,* **359,** 133-135, 1992.

(57) The chUdren of the STM.
Pool R., *Science,* **247,** 634-636, 1990.

(58) Near-field optics: Microscopy, spectroscopy, and surface modification beyond the diffraction Umit
Betzig E. and Trautman J.K., *Science,* **257,** 189-195, 1992.

(59) Scanning probe microscopy and magnetic resonance.
Manassen Y., *Advanced Materials,* **6, 401-404,** 1994.

(60) STM on metals.
Kuk Y., in *Scanning Tunneling Microscopy I,* Giintherodt H.-J. and Wiesendanger R., Springer Series in Surface Sciences 20, Springer-Verlag, Germany, 1992, chap. 3.

(61) STM on semiconductors.
Hamers R.J., in *Scanning Tunneling Microscopy I,* Giintherodt H.-J. and Wiesendanger R., Springer Series in Surface Sciences 20, Springer-Verlag, Germany, 1992, chap 5.

(62) Scanning tunneUng microscopy observations of benzene molecules on the Rh(111)-(3x3)($C_6H_6$+2CO) surface.
Ohtani H., WUson R.J., Chiang S. and Mate CM., *Physical Review Letters,* 60, 2398-2401, 1988.

(63) 7x7 reconstmction on Si(l 11) resolved in real space.
Binnig G., Rohrer H., Gerber Ch. and Weibel E., *Physical Review*

*Letters, 50,* 120-123, 1983.

(64) Biological applications of atomic force microscopy
Lal R. and John S.A., *American Journal of Physiology,* **266, 51-66,** 1994.

(65) Direct measurement of the forces between complemenatry strands of DNA.
Lee G.U., Chrisey L.A. and Colton R.J., *Science,* **266,** 771-773, 1994.

(66) Adhesion forces between individual Ugand-receptor pairs.
Florin E-L, Moy V.T. and Gaub H.E., *Science,* **264,** 415-417, 1994.

(67) Stmcture of the Extracellular Surface of the Gap Junction by Atomic Force Microscopy.
Hoh J.H., Sosinsky G.E., Revel J. and Hansma P.K., *Biophysical Journal,* **65, 149-163,** 1993.

(68) Atomic force microscopy of the electrochemical nucleation and growth of molecular crystals.
HiUier A.C and Ward M.D., *Science,* **263,** 1261-1264, 1994.

(69) Domian stmctures in LB fihns investigated by atomic force microscopy.
Chi L.F., Anders M., Fuchs H., Johnston R.R. and Ringdorf H., *Science* , **259,** 213-216, 1993.

(70) An atomic force microscopy study of a self-assembled octadecyl mercaptan monolayer adsorbed on gold(l 11) under potential control.
Pan J., Tao N. and Lindsay S.M., *Langmuir, 9,* 1556-1560, 1993.

(71) Atomic force microscopy of an organic monolayer.
Marti O., Ribi H.O., Drake B., Albrecht T.R., Quate CF. and Hansma P.K., *Science,* **239,** 50-53, 1988.

(72) Imaging and modification of polymers by scanning tunneling and atomic force microscopy.
Albrecht T.R., Dovek M.M., Lang C.A., Gmtter P., Quate C.F., Kuan S.W.J., Frank CW. and Pease R.F.W., *Journal of Applied Physics* , **64, 1178-1184,** 1988.

(73) Imaging steep, high stmctures by scanning force microscopy with electron beam deposited tips.
Keller D.J. and Chih-Chung C, *Surface Science,* **268,** 333-339, 1992.

(74) Envelope reconstmction of probe microscope images.
Keller D.J. and Franke F.S., *Surface Science, 294,* 409-419, 1993.

(75) Polymer crystaUization.
Keller A., *Philosophical Magazine,* **2, 1171-1174,** 1957.

(76) CrystaUine polymers: An introduction,
Keller A., *Faraday Discussions of the Royal Society of Chemistry,* **68,** 144-166, 1979.

(77) Atomic force microscopy on polymers and polymer related compounds 2. Monocrystals of normal and cyclic alkanes
Stocker W., Bar G., Kunz M., MoUer M., Magonov S.N., and Cantow H.J., *Polymer Bulletin,* 26, 215, 1991.

(78) Molecular folds in polyethylene observed by atomic force microscopy.
Patil R. and Reneker D.H., *Polymer,* 35, 1909-1914, 1994.

(79) Direct unaging of the surfaces of poIy(p)hydroxybutyrate and hydroxybutyrate oUgomers by atomic force microscopy.
Sykes K.E., McMaster T.J., Miles M.J., Barker P.A., Barham P.J., Seebach D., MüUer H.-M. and Lengweiler U.D., *Journal of Materials Science,* 30, 623-627, 1995.

(80) Atomic Force Microscopy of Extended-Chain Crystals of Polyethylene
Annis B.K., Reffner J.R. and Wunderiich B., *Journal of Polymer Science Part B,* 31, 93-97, 1993.

(81) Short-range order in extended-chain crystals of polyoxymethylene from a tme molecular perspective: An atomic force microscopy study.
Snétivy D., Yang H., Glomm B. and Vancso G.J., *Journal of Material Chemistry, 4,* 55-59, 1994.

(82) Toughened plastics.
Bucknall C.B., Applied Science PubUshers, London, 1977.

(83) Atomic force microscopy on polymers and polymer related compounds: 1. Cold-extmded polyethylene.
Magonov S.N., Qvamström K., Elings V. and Cantow H.-J., *Polymer Bulletin,* 25, 689-694, 1991.

(84) Atomic force microscopy of gel-drawn ultrahigh molecular weight polyethylene.
Magonov S.N., Sheiko S.S., Deblieck R.A.C and Möller M., *Macromolecules,* **26,** 1380-1386, 1993.

(85) Molecular resolution of thin, highly oriented poly(tetrafluoroethylene) fihns with the atomic force microscope.
Hansma H., Motamedi F., Smith P., Hansma P. and Wittman J.C, *Polymer,* 33, 647-649, 1992.

(86) Molecular stmcture and tiiickness of highly oriented poly(tetrafluoroethylene) fihns measured by atomic force microscopy.
Dietz P., Hansma P.K., Ihn K.J., Motamedi F. and Smith P., *Journal of Materials Science,* **28,** 1372-1376, 1993.

(87) Atomic force microscopy of crystals: 7. Chain packing, disorder and imaging of methyl groups in oriented isotactic polypropylene.
Snétivy D. and Vancso G.J., *Polymer,* 35, 461-467, 1994.

(88) Atomic force microscopy of polymer crystals: 7. Chain packing, disorder and imaging of methyl groups in oriented isotactic polypropylene.
Snétivy D. and Vancso G.J., *Polymer,* 35, 461-467, 1994.

(89) Scanning force microscopy of nanostructured uniaxiaUy oriented ultra thin film surfaces of isotactic polystryene.
Jandt K.D., Eng L.M., Petermann J. and Fuchs H., *Polymer ,* 33, 5331-5333, 1992.

(90) Scanning force microscopy of melt-crystallised metal-evaporated poly(butene-1) ultrathin films.
Jandt K.D., McMaster T.J., Miles M.J. and Petermann J., *Macromolecules,* 26, 6552-6556, 1993.

(91) Contact faces of epitaxiaUy crystaUized a- and γ- phase isotactic polypropylene observed by atomic force microscopy.
Stocker W., Magonov S.N., Cantow H.J., Wittman J.C. and Lotz B., *Macromolecules,* 26, 5915-5923, 1993.

(92) Direct observation of right and left handed heUcal hands of syndiotactic polypropylene by atomic force microscopy.
Stocker W., Schmacher M., Graff S., Lang J., Wittman J.C, Lovinger A.J. and Lotz B., *Macromolecules,* 27, 6948-6955, 1994.

(93) AnneaUng effect on the surface stmcmre of latex fUms studied by atomic force microscopy.
Goh M.C, Juhué D., Leung O.M., Wang Y. and Winnik M.A., *Langmuir, 9,* 1319-1322, 1993.

(94) Scanning tunneling microscopy and atomic force microscopy of polystyrene spin-coated onto silicon surfaces.
Stange T.G., Mathew R., Evans D.F. and Hendrickson W.A., *Langmuir,* 8, 920-926, 1992.

(95) Atomic force microscopy of polymer crystals 1. Chain fold domains in PEO lameUae.
Snétivy D. and Vaneso J., *Polymer ,* 33(2), 432, 1992.

(96) Scanning force microscopy of nanofibrillar structure of drawn polyethylene tapes: 1. Different modes and tips.
Sheiko S.S., Möller M., Cantow H.-J. and Magonov S.N., *Polymer Bulletin,* 31, 693-698, 1993.

(97) Anisotropic friction at the surface of lameUar crystals of poly(oxymethylene) by lateral force microscopy.
Nisman R., Smith P. and G.J. Vancso, *Langmuir,* 10, 1667-1669, 1994.

(98) Polymer blends and composites.
Woodward A.E., in *A tlas of Polymer Morphology,* Hanser Publishers, Oxford University Press, 1989, chap. 9.

(99) Surface enrichment in an isotopic polymer blend.
Jones R.A.L., Kramer E.J., Rafailovich M.H., Sokolov J. and Schwarz S.A., *Physical Review Utters,* 62, 280-283, 1989.

(100) Ordering of co-polymer thin fihns as revealed by atomic force microscopy.
Collin B., Chatenay D., Coulon G., Ausserre D. and Gallot Y.,

*Macromolecules* , **25,** 1621-1622, 1992.

(101) Determination of surface morphology of diblock copolymers of styrene and butadiene by atomic force microscopy.
Annis B.K., Schwark D.W., Reffner J.R., Thomas E.L. and Wunderiich B., ***Makromolekulare*** *Chemie,* **193,** 2589-2604, 1992.

(102) Morphological smdies of spin-coated fihns of poly(styrene-block-**methyl methacrylate)** copolymers by atomic force microscopy.
Nick L., Kindermann A. and Fuhrmann J., *Colloid and Polymer Science,* ***272,*** 367-371, 1994.

(103) Local properties of phase-separated polymer surfaces by force microscopy.
Motomatsu M., Nie H.Y., Mizutani W. and Tokomoto H., *Japanese Journal of Applied Physics,* **33,** 3775-3778, 1994.

(104) Early-stage phase separation in polyimide precursor blends: An atomic force microscopy study.
Saraf R.F., *Macromolecules,* 26, 2623-3630, 1993.

(105) Corona-treated isotactic polypropylene fUms investigated by friction force microscopy.
Ovemey R.M., Giintherodt H.-J and HUd S., *Journal of Applied Physics,* 75, 1401-1404, 1994.

(106) Surface **texturing** of PTFE film using non-equiUbrium plasmas.
Ryan M.E. and Badyal J.P.S., *Macromolecules,* 28, 1377-1382, 1995.

(107) Atomic force microscopy **study** of mbbed polyimide films.
Zhu Y-M, Wang L., Lu Z-H, Wei Y., Chen X.X. and Tang J.H., *Applied Physics Letters,* 65, 49-51, **1994.**

(108) Laser-induced sub-half-micrometer periodic stmcture on polymer surfaces.
Hiraoka H. and Sendova M., *Applied Physics Letters,* 64, 563-565, 1994.

(109) Surface morphology of poly(butyl **acrylate)/poly(methyl** methacrylate) core shell latex by atomic force microscopy.
Sommer F., **Duc** T.M., Pirri R., Meunier G. and Quet C, *Langmuir,* ***11,***440-448, 1995.

(110) Imaging surfaces of **hydrophilic** contact lenses with the atomic force microscope.
Baguet J., Sommer F. and **Duc** T.M., *Biomaterials,* 14, 279-284, 1993.

(111) The surface stmcture and morphology of **poly vinylidene** fluoride microfUtration membranes by atomic force microscopy.
Fritzsche A.K., Arevalo A.R., Moore M.D., **Elings** V.B., KjoUer K. and Wu CM., *Journal of Membrane Science* , 68, **65-78, 1992**

(112) Is the molecular surface of polystryene really glassy ?
Meyers G.F., DeKoven B.M. and Seitz J.T., *Langmuir,* 8, 2330-

2335, 1992.

(113) Submicrometer modification of polymer surfaces with a surface force microscope.
Jin X. and Unertl W.N., *Applied Physics Letters,* **61,** 657-659, 1992.

(114) Creation of Uquid crystal waveguides with scanning force microscopy.
Rüetschi M., Griitter, Fiinfschilling J. and Giintherodt H.-J., *Science,* **265,** 512-514, 1994.

(115) Microscope design and operation.
BonneU D.A., in *Scanning Tunneling Microscopy and Spectroscopy Theory, Techniques and Applications,* ed. BonneU D.A., VCH Publishers Inc., New York, 1993.

(116) Forces in atomic force microscopy in air and water.
Weisenhorn A.L., Hansma P.K., Albrecht T.R. and Quate C.F., *Applied Physics Utters,* **54,** 2651-2653, 1989.

(117) Atomic-scale resolution in atomic force microscopy.
Lin F and Meier D.J., *Langmuir,* **10,** 1660-1662, 1994.

(118) Atomic scale contrast mechanism in atomic force microscopy.
Heinzelmann H., Meyer E., Bridbeck D., Ovemey G. and Güntherodt H.-J., *Zeitschrift für Physik B- Condensed Matter,* **88,** 321-326, 1992.

(119) Interpretation of atomic force microscopy images: The mica (001) surface with a diamond apex.
Tang H., Joachim C and DeviUers J., *Journal of Vacuum Science Technology B.,* **12,** 2251-2253, 1994.

(120) Atomic-scale wear properties of muscovite mica evaluated by scanning probe microscopy.
Miyake S., *Applied Physics Utters,* **65,** 980-982, 1994.

(121) Atomic force microscopy of layered compunds.
Miller R.G. and Bryant P.J., *Journal of Vacuum Science and Technology, Al,* 2879-2881, 1989.

(122) Tme atomic resolution by atomic force microscopy through repiUsive and attractive forces.
Ohnesorge F. and Binnig G., *Science,* **260,** 1451-1456, 1993.

(123) Information on the Genesis II graphics system is available on the World Wide Web. The URL is http://pharml.pharm.nottingham.ac.uk/.

(124) Determination of the optical constants of metals by excitation of surface plasmons.
Kretschmann E., *Zeitschrift für Physik,* **241,** 313-324, 1971.

(125) Surface plasma oscUlations.
Raether H., in *Physics of Thin Films,* eds. Hass G., Francombe M.H. and Hoffman R.W., Academic Press, New York, 1977, vol. 9.

(126) A compact surface plasmon resonance sensor for measurement of water in process.
Matsubara K., Kawata S. and Minami S., *Applied Spectroscopy,* 42, 1375-1379, 1988.

(127) Dynamic, in-situ techniques for probing surface properties of biomaterials.
Davies J., Allen A, Burms Y., Bmce I., Heaney P.J., Hemming F.A., Nunneriey CS. and Skelton L., in *Surface Properties of Biomaterials,* ed. West R. and Batts G., (Butterworth-Heinemann Ltd, Oxford, 1994).

(128) Dynamic surface events measured by simultaneous probe microscopy and surface plasmon detection.
Chen X., Davies M.C., Roberts CJ., Shakesheff K.M., Tendler S.J.B. and WilUams P.M., *Analytical Chemistry,* submitted.

(129) Morphological characterization of bioerodible polymers. 3. Characterization of the erosion and intact zones in polyanhydrides usmg scanning electron microscopy.
Mathiowitz E., Jacob J., Pekarek K. and Chickerimg D., *Macromolecules,* 26, 6756-6765, 1993.

(130) Effects of roughness on the thrombogenicity of plastics.
Hecker J.F. and Edwards R.O., *Journal of Biomedical Materials Research,* 15, 1-7, 1981.

(131) Tissue engineering.
Langer R. and Vacanti J.P., *Science,* **260,** 920-926, 1993.

(132) Electron microscopy in polymer science.
Michler G.H., *Applied Spectroscopy Reviews,* 28, 327-384, 1993.

(133) Polymer microscopy.
Hobbs S.Y., *Journal of Macromolecular Science Reviews Macromolecular Chemistry,* **C19,** 221-265, 1980.

(134) The principles and practice of electron microscopy.
Watt I.M., Cambridge University Press, Cambridge, 1985.

(135) The influence of microstmcture and monomer properties on the erosion mechanism of a class of polyanhydrides.
Göpferich A. and Langer R., *Journal of Polymer Science: Part A: Polymer Chemistry,* 31, 2445-2458, 1993.

(136) Block co-polymers of L-lactide and poly(ethylene glycol) for biomedical applications.
Cerrai P., TricoU M., LeUi L., Guerra G.D., Sbarbati Del Guerra R., Cascone M.G. and Giusti P., *Journal of Materials Science: Materials in Medicine,* 5, 308-313, 1994.

(137) Histological evaluation of a biodegradable polyactive/hydroxyapatite membrane.
Jansen J.A., de Ruijter P.T.M. and Paquay Y.G.C.J., *Biomaterials,*

**16,** 819-827, 1995.

(138) New bioactivation mode for vascular protheses made of Dacron polyester.
Bonzon N., Lefebvre F., Ferre N., Daculsi G. and Rabaud M., *Biomaterials,* **16,** 747-751, 1995.

(139) Stmcture and behaviour in hydrophillic matrix sustained-release dosage forms. 3. The influence of pH on the sustained-release performance and intemal gel stmcmre of sodium algmate matrices.
Hodsdon A.C, Mitchell J.R., Davies M.C. and Melia CD., *Journal of Controlled Release, 33,* 143-152, 1995.

(140) Review and oudme of environmental SEM at present.
Damlatos G.D., *Journal of Microscopy,* **162,** 391-402, 1991.

(141) Introduction to the ESEM instmment
DanUatos G.D., *Microscopy Research and Technique,* 25, 354-361, 1993.

(142) Preparation, characterization, and dmg release from thermoresponsive microspheres.
D'Emanuele A. and Dinarvand R., *International Journal of Pharmaceutics,* **118,** 237-242, 1995.

(143) An investigation of the effects of ultrasound on degradable polyanhydride matrices.
D'Emanuele A., Kost J., HiU J.L. and Langer R., *Macromolecules,* 25, 511-515, 1992.

(144) AppUed polymer light microscopy.
Hemdsley D.A. ed, Elsevier Science Publishers Ltd., Barking, 1989.

(145) Degradation of high molecular weight poly(L-lactide) in alkaline medium.
Cam D., Hyon S-H. and Ikada Y., *Biomaterials,* **16,** 833-843, 1995.

(146) Degradation of polydispersed poly(L-lactic acid) to modulate lactic acid release.
von Recum H.A., Cleek R.L., Eskin S.G. and Mikos A.G., *Biomaterials,* **16,** 441-447, 1995.

(147) Poly(ethylene glycol) chemistry: Biotechnical and biomedical applications.
Harris M.J. ed., Plenum Press, New York, 1992.

(148) Protein-surface interactions in the presence of polyethylene oxide.
Jeon S.I., Lee J.H., Andrade J.D. and De Gennes P.G., *Journal of Colloid and Interface Science,* **142, 149-158,** 1991.

(149) A phenomenological dieory of spherulitic crystalUzation.
Keith H.P. and Padden F.J. *Journal of Applied Physics,* 34, 2409-2421, 1963.

(150) Polymer sphemlites.

Marentette J.M. and Brown G.R., *Journal of Chemical Education,* 70, 435-439, 1993.

(151) CaUbration of atomic force microscope tips using biomolecules. Thundat T., Zheng X.Y., Sharp S.L., AlUson D.P., Warmack R.J., Joy P.I. and FerreU T.L., *Scanning Microscopy,* 6, 903-910, 1992.

(152) Conformational and packing stabiUty of crystalUne polymers. III. Simplified method of energy calculation to set up heUcal molecular models for x-ray analysis. Sakakihara-Kitahama H. and Tadokoro H., *Journal of Macromolecular Science,* B9, 511-520, 1974.

(153) Polymer Handbook. Brandmp J. and Immergut E.H., 3rd edition, Wiley-Interscience, New York, 1989.

(154) The solid-liquid interface. Woodmff D.P., Cambridge University Press, Cambridge, 1973.

(155) Growth of fibrillar polymer crystals from flowing solutions. Pennings C.J., *Journal of Polymer Science: Polymer Symposium,* 59, 55-75, 1977.

(156) Evidence of DNA bending in transcription complexes imaged by scanning force microscopy. Rees W.A., Keller R.W., Vesenka J.P., Yang GuoUang and Bustamante C, *Science,* 260, 1646-1649, 1993.

(157) AFM studies of protein adsorption. 1. Time-resolved protein adsorption to highly oriented pyrolytic-graphite. CuUen D.C. and Lowe C.R. *Journal of Colloid and Interface Science,* 166, 102-108, 1994.

(158) Novel dmg deUvery. Prescott L.F. and Nimmo W.S. ed., John Wiley & Sons, Chicester, 1990, chapters 1-3.

(159) Pharmaceutical appUcations of controUed release: An overview of the past, present and future. Banker G.S., in *Medical Applications of Controlled Release,* Langer R.S. and Wise D.L., CRC Press, Inc., Florida, 1984, chapter 1.

(160) The time clock system - A new oral dosage form for the fast and complete release of dmg after a pre-determined lag time. Pozzi F., Furlani P., Gazzaniga A., Davis S.S. and Wilding I.R., *Journal of Controlled Release,* 31, 99-108, 1994.

(161) Enteric-coated tune release systems for colonic targetting. Wilding I.R., Davis S.S., Pozzi F., Furlani P., Gazzaniga A., *International Journal of Pharmaceutics,* 111,99-102, 1994.

(162) Factors influencing dmg and protein-transport and release from ionic hydrogels Amende M.T., Hariharan D. and Peppas N.A., *Reactive Polymers,*

**25,** 127-137, 1995.

(163) Microscpheres for targeting dmgs to specific body sites.
Davis S.S., Illum L., Moghimi S.M., Davies M.C, Porter C.J.H., Muir I.S., Brindley A., Christy N.M., Norman M.E., WiUiams P. and Dunn S.E., *Journal of Controlled Release,* **24,** 157-163, 1993.

(164) Rate control in transdermal dmg delivery.
Guy R.H. and Hadgraft J., *International Journal of Pharmaceutics,* 82, R1-R6, 1992.

(165) Ultrasound-mediated transdermal protein delivery.
Mitragotri S., Blankschtein D. and Langer R., *Science,* **269,** 850-853, 1995.

(166) Dmg targeting and retrometaboUc dmg design approaches - Introduction.
Bodor N., *Advanced Drug Delivery Reviews,* **14,** 157-166, 1994.

(167) Design of prodmgs for improved gastrointestinal absorption by intestinal enzyme targeting.
Fleisher D., Stewart B.H. and Amidon G.L., *Methods in Enzymology,* **112, 360-381,1985.**

(168) Osmotic drug-delivery - A review of the patent literature.
Santus G. and Baker R.W., *Journal of Controlled Release,* **35,** 1-21, 1995.

(169) Placebo-controlled trial of safety and efficacy of intraoperative controlled delivery by biodegradable polymers of chemotherapy for recurrent gliomas.
Brem H., Piantadosi S., Burger P.C, Walker M., Selke R., Vick N.A., Black K., Sisti M., Brem S., Mohr G., Muller P., Morawetz R. and Schold S.C, *Lancet,* **345,** 1008-1012, 1995.

(170) Polymers for controUed parenteral deUvery of peptides and proteins.
*Heller* **J.,** *Advanced Drug Delivery Reviews, 10,* 163-204, 1993.

(171) ControUed dmg release from poly(ortho esters) - A surface erodmg polymer.
Heller J., 7. *Controlled Release, 2,* **167, 1985.**

(172) Polymeric Biomaterials.
Dumitriu S.ed., Marcel Dekker, Inc., New York, 1994, chapter 13.

(173) The acceleration of degradation-controlled dmg delivery from polyester microspheres.
Cha Y. and Pitt CO., *Journal of Controlled Release,* 8, 259-265, 1989.

(174) Present and future of PLA polymers.
Vert M., Schwarch G. and Coudane J., *Journal of Macromolecular Science: Pure and Applied Chemistry,* **A32, 787-796, 1995.**

(175) Polyanhydrides for controUed release of bioactive agents.

Leong K.W., Kost J., Mathiowitz E. and Langer R., *Biomaterials, 1,* 364-371, 1986.

(176) The development of polyanhydrides for fmg delivery applications. Tamada J. and Langer R., *Journal of Biomaterial Science Polymer Edition, 3,* 315-353, 1992.

(177) Bioerodible polyanhydrides as dmg-carrier matrices. 1. Characterization, degradation and release characteristics. Leong K.W., Brott B.C. and Langer R., *Journal of Biomedical Materials Research,* 19, 941-955, 1985.

(178) Polymer Blends. Paul D.R. and Newman S. eds., Academic Press, New York, 1979, vol 3.

(179) Encyclopedia of Polymers Science and Engineering. Paul D.R., Barlow J.N. and Keskkula H.ed., John Wiley & Sons, New York, 1988.

(180) Degradable polymer blends. 1. Screening of miscible polymers. Domb A. J., *Journal of Polymer Science: Part A:Polymer Chemistry,* 31, 1973-1981, 1993.

(181) Polymer blends and composites. Woodward A.E., in *Atlas of Polymer Morphology,* Hanser Publishers, Oxford University Press, 1989, chapter 9.

(182) Characterization of immiscible elastomer blends. Hess W.M., Herd C.R. and Vegvari P.C, *Rubber Chemistry and Technology,* 66, 329-375, 1993.

(183) Characterizing domain muting effects in hydrogen bond-compatibUized polymer blends. Taylor-Smith R.E. and Register R.A., *Journal of Polymer Science: Part B: Polymer Physics,* 32, 2105-2114, 1994.

(184) Electron-microscopic observation of spinodal decomposition in blends of tetramethyl polycarbonate and polystyrene. Shabana H.M., Guo W., OUey R.H. and Bassett D.C, *Polymer,* 34, 1313- 1315, 1993.

(185) Ruthenium tetraoxide staining of polymers - new preparative methods for electron-microscopy. Trent J.S., *Macromolecules,* 17, 2930-2931, 1984.

(186) Surface morphology of a polymer blend examined by laser confocal fluorescence microscopy. Li L., Sosnowski S., Chaffey C.E., Balke S.T. and WinnUc M.A., *Langmuir,* 10, 2495-2497, 1994.

(187) Polyanhydrides - synthesis and characterization. Domb A.J., Amselem S., Shah J. and Maniar M., *Advances in Polymer Science,* 107, 93-141, 1993.

(188) Surface analysis of biodegradable polymer blends of poly(sebacic anhydride) and poly(dl-lactic acid).
Davies M.C, Shakesheff K.M., Shard A.G., Domb A., Roberts C.J., Tendler S.J.B. and Williams P.M., *Macromolecules,* submitted.

(189) Peptide and protein dmgs. I. Therapeutic applications; absorption and parenteral administration.
Zhou X.H. and Li Wan Po A., *International Journal of Pharmaceutics,* 75,97-115, 1991.

(190) An analytical review of growth-hormone smdies im children after renal-transplantation.
Ingulli E. and Tejani A., *Pediatric Nephrology, 9,* 61-65, 1995.

(191) PulsatUe LHRH tiierapy in patients witii oligozoospermia and disturbed LH pulsatiUty.
Aulitzky W., Frick J. and HadziseUmovic F, *International Journal of Andrology,* 12, 265-272, 1989.

(192) A review of the clinical-studies of alpha-interferon in the management of multiple-myeloma.
Cooper M.R., *Seminars in Oncology,* 18, 18-29, 1991.

(193) Stand and deliver: Getting peptide dmgs imto the body.
WaUace B.M. and Lasker J.S., *Science,* **260,** 912-913, 1993.

(194) Transdermal deUvery of peptide and protein dmgs: An overview.
Amsden B.G. and Goosen M.F.A., *AIChe Journal,* 41, 1972-1997, 1995.

(195) A novel emulsification-solvent extraction technique for production of protein loaded biodegradable microparticles for vaccine and dmg delivery.
Yeh M.-K., Coombes A.G.A., Jenkins P.G. and Davis S.S., *Journal of Controlled Release,* **33, 437-445,** 1995.

(195) Penetration enhancement for polypeptides through epithelia .D. Routes of deUvery case smdies .8. The vaginal route of peptide and protein dmg delivery.
Richardson J.L. and Ilium L., *Advanced Drug Delivery Reviews,* 8, 341-366, 1992.

(196) In-vitro release profiles of eristostatin from biodegradable polymeric microspheres - protein aggregation problem.
Lu W.Q. and Park T.G., *Biotechnology Progress,* 11, 224-227, 1995.

(197) Poly(ortho esters)
Heller J., Sparer R.V. and Zenmer G.M., im *Biodegradable Polymers as Drug Delivery Systems,* ed. Chasin M and Langer R., Marcel Dekker, Inc., New York, 1990.

(198) Preparation of poly(ortho esters) by the reacion of ketene acetals and polyols.
Heller J., Penhale D.W.H. and Helwing R.F., *Journal of Polymer*

*Science: Polymer Letters Edition,* 18, 82-83, 1980.

(199) Some equiUbrium and kinetic aspects of water sorption in poIy(ortho esters).
Nguyen T.H., Himmelstein K.J. and Higuchi T., *International Journal of Pharmaceutics, 25,* 1-12, 1985.

(2(X)) Control of polymer surface erosion by the use of excipients.
Heller J., in *Polymers in Medicine II,* ed. Chielini E., MigUaresi P.C, Giusti S. and Nicolais L., Plenum Press, New York, 1986.

(201) Controlled release from erosible poly(ortho ester) dmg deUvery systems.
Sparer R.V., Chung S., Ringeisen CD. and Himmelstein K.J., *Journal of Controlled Release, 1,* 23-32, 1984.

(202) The use of poly(ortho esters) for the controUed release of 5-fluorouracU and a LH RH analogue.
Heller J., Ng S.Y., Penhale D.W.H., Fritzinger B.K., Sanders L.M., Bums R.A. and Bhosale S.S., *Journal of Controlled Release, 6,* 217-224, 1987.

(203) Controlled release from poly(ortho esters).
Heller J., *Annals of the New York Academy of Sciences,* **446, 51-66,** 1985.

(204) Computational studies in scanning probe microscopy.
WiUiams P.M., thesis submitted to The University of Nottingham, 1995.

(205) Computer-assisted microscopy: The measurement and analysis of images.
Russ J.C, Plenum Press, New York, 1992.

(206) Non-assumptive analysis of SPM data.
WiUiams P.M., Shakesheff K.M., Davies M.C, Jackson D.E., Roberts C.J. and Tendler S.J.B., *Langmuir,* submitted.

(207) Real-time biospecific interaction analysis.
Lundström I., *Biosensors & Bioelectronics,* **9, 725-736,** 1994.

(208) Tobacco mosaic vims: A model antigen to smdy virus-antibody interactions.
Van Regenmortel M.H.V., Altschuh D. and Zeder-Lutz G., *Biochimie,* 75, 731-739, 1993.

(209) Lactose repressor-operator DNA interactions: Kinetic analysis by a surface plasmon resonance biosensor.
Bondeson K., Frostell-Karlsson A, Fägertam L. and Magnusson G., *Analytical Biochemistry,* **214,** 245-251, 1993.

(210) Epitope mapping and binding kinetics of monoclonal antibodies smdied by real time biospecific interaction analysis using surface plasmon resonance.
Johne B., Gadnell M. and Hansen K., *Journal of Immunological*

*Methods,* **160,** 191-198, 1993.

(211) Detection of antigen-antibody interactions by surface plasmon resonance. Apphcation to epitope mapping.
Fägertam L., FrosteU A, Karisson R., KuUman M., Larsson A., Malmqvist M. and Butt H., *Journal of Molecular Recognition,* 3, 208-214, 1990.

(212) Physics of biosensing witii an extended coupUng matrix and surface plasmon resonance.
Liedberg B., Lundström I. and Stenberg E., *Sensors and Actuators B,* **11,** 63-72, 1993.

(213) Use of scanning probe microscopy and surface plasmon resonance as analytical tools in the study of antibody-coated microtiter weUs.
Davies J., Roberts C.J., Dawkes A.C., Sefton J., Edwards J.C, Glasbey T.O., Haymes A.G., Davies M.C, Jackson D.E., Lomas M., Shakesheff K.M., Tendler S.J.B., WiUdns M.J. and Williams P.M., *Langmuir,* **10,** 2654-2661, 1994.

(214) The use of surface plasmon resonance and atomic force microscopy for the smdy of protem adsorption to model and protein resistant polymer surfaces.
Davies M.C, Green R., Chen X., Roberts C.J., Shakesheff K.M., Tendler S.J.B. and WUUams P.M., *Abstracts of Papers of the American Chemical Society,* **209,** 6-7, 1995.

(215) The effect of thin organic fdms on the surface plasmon resonance on gold.
Gordon II J.G. and Swalen J.D., *Optics Communications,* **22,** 374-376, 1977.

(216) Surface plasmon spectroscopy of organic monolayer assemblies.
Pockrand I., Swalen J.D., Gordon II J.G. and Philpott M.R., *Surface Science,* 74, 237-244, 1977.

(217) Surface plasmon resonance characterization of spin-deposited phthalocyanme fihns.
Vukusic P.S., Sambles J.R. and Wright J.D., *Journal of Material Chemistry,* **2,** 1105-1106, 1992.

(218) Monolayer and multUayer film characterization using surface plasmon resonance.
Cooke S.J. and Roberts G.G., *Thin Solid Films,* **210/211,** 685-688, 1992.

(219) A study of the adsorption of alkanes on a thin-metal film.
Bradberry G.W., Vukusic P.S. and Sambles J.R., *Journal of Chemical Physics,* 9%, 651-654, 1993.

# Acknowledgements

Throughout the three years of my Ph.D I have received exceptional support from many people in the Department of Pharmaceutical Sciences. I would like to start by thanking Martyn Davies and Saul Tendler for their excellent guidance in all aspects of my work and for their help in planning my future career. Widiout their hard work in setting up the Laboratory of Biophysics and Surface Analysis the opportunity to work in SPM would never have arisen. I hope to get the chance to work with both of them again in the future.

From the first day of my Ph.D, Clive Roberts has offered guidance and experimental advice which has been invaluable. I would particularly like to thank him for passing on his experience in SPM in the first year, which gave me a flying start and was an excellent foundation for all the degradation smdies. Thanks also for beating me at nearly every sport in which we have competed (except golf).

I would also like to express my appreciation for the work and help of PhU WiUiams, whose Genesis system has contributed superbly to the analysis of the SPM data. Thanks also for the hard work setting up the back-up and retrieval systems, which save everyone in the Lab a lot of time and worry.

Thanks also to everyone in the Lab for keeping me entertained. Good luck with your Ph.Ds.

Special thanks to all my family for their support through the years. Especially to my Mum, Dad and Claire who have always encouraged me in every way. Good luck Claire with your GCSEs, the hard work will be worthwhile. Thanks also to all my Grandparents who always provide encouragement by being genuinely proud of the achievements of all their grandchildren. Fmally, thanks to Stephanie Ann for making me very happy for aU the three years.

## Appendix Lectures Attended

Rapid Identification of Proteins by Peptide Mass Fmgerprinting.
Dr. Daryl Pappin, Imperial Cancer Research Fund, London.

Sialylation of Gonococcal Lipopolysaccharide by Host Factors: A Major Impact on Pathogenicity.
Prof. Harry Smith, University of Birmingham School of Medicme.

Monitoring Exposure to Alkylating Agents by Determmation of DNA and Protein Adducts.
Dr. Peter Farmer, MRC Toxicology Unit Leicester University.

Pharmaceutical R & D - How and Why?.
Dr. J. Gareth Bowen, Head of Biology, Boots Pharmaceuticals, Nottingham.

Tumour PermeabiUty and Dmg DeUvery.
Dr. Len Seymour, Department of CUnical Oncology, University of Birmmgham School of Medicine.

Probing Antibody-Antigen Interactions - Watching it all Happen.
Dr. John Davies, Kodak Clinical Diagnostics Ltd.

Development of Anti-Cancer Agents: Discovery to Market
Dr. Brent Vose, Zeneca Pharmaceuticals, Macclesfield.

Endosomes / Lysosomes: The Commonality in Ideopathic and Transmissible Neurodegenerate Diseases.
Prof John Mayer, Department of Biochemistry, University of Nottingham.

Isotope-Aided NMR Studies of Protein-Ligand Interactions.
Dr. Jim Feeney, Laboratory of Molecular Stmcmre, National Institute for Medical Research, MiU Hill.

Transglutaminase, Programmed Cell Death and Tumour Progression.
Prof Martin Griffin, Department of Life Science, Nottingham Trent University.

Sequence-Specific Recognition of DNA: Approaches to Gene Regulation.
Prof Stephen Neidle, CRC Biomolecular Stmcmre Unit, Institute of Cancer Research, University of London.

Resistance-Modifyṁg Agents in Cancer Chemotherapy.
Dr. Roger Griffin, Department of Chemistry, Newcastie University.

Practice Research ṁ a Health Services Related Context
Prof Peter Noyce, Department of Pharmacy, Manchester University.

Fish Odour Syndrome.
Dr S MitcheU, Dept of Pharmacology and Toxicology, St Mary's Hospital Medical School, London.

Morphine and Pain.
Dr R A Moore, Oxford Regional Pain Relief Unit

Mickey Mouse Donning a lab coat
Prof A Li Wan Po, Dept of Pharmaceutical Sciences, University of Nottingham.

Combinatorial Chemistry.
Dr R Shute, Compound Libraries Group, Zeneca Pharmaceuticals.

Polymers do it at interfaces.
Dr T Cosgrove, School of Chemistry, University of Bristol.

A.C electrokinetic characterisation and manipulation of bioparticle
Prof R Pethig, University of Bangor.

Novel chemistry and approaches utUizing solid-phase peptide synthesis.
Dave Evans

Characterization of PLA-PEG copolymers for use as dmg delivery systems.
Sue Hagan

Synthesis and development of a series of novel acridine anti-tumour agents.

Damien Hagan

Uptake of colloidal particles by the lymphatic system.
Ann Hawley

The incorporation of computational chemistry algorithms into a multimedia environment.
Richard Hyde

Synthesis of lactones.
Barrie KeUam

Formulation of a non-toxic amphotericin B emulsion.
Martin Lance

An investigation into the mechanism of action of nasal absorption enhancers.
Susan Mayor

Biophysical smdies of biomolecules related to cancer.
Kathryn Measures

Mucins in breast cancer: the science to the cUnic.
Andrea Murray

Investigating HPLC stationary phases.
Rick Watson

The use of echo-planar magnetic resonance imaging to assess retained water volume in the distal smaU bowel.
Dawn Adkin

Protein adsorption to polymeric microspheres: its impUcations for dmg targeting.
Ian Armstrong

Evaluation of 153Sm-DTPA for radiolabeUing of pharmaceutical dosage forms by neutron activation.

Mohammed Awang

Surface analysis of starch granules.
Paul Baldwin

Characterization of homologous regulatory genes involved in carbapenem antibiotic biosynthesis and bioluminescence in bacteria.
Pan Chan

Polymers for colonic dmg deUvery.
Walter Cook

The fine stmcmre of mucin glycoproteins.
Gareth Davies

The biological fate of novel microspheres designed for site specific dmg targeting.
Sue Dunn

An investigation into the mechanism of action and optimisation of a dmg carrier conjugate.
John Fitzpatrick

Mechanisms of cysteine conjugate toxicity.
Peter Gaskin

Synthesis of novel tyrosine kinase inhibitors.
Margaret Joyce

Characterization, regulation and vaccine potential of transferrin binding proteins in *Haemophilus influenzae* type b.
Tina Parsons

Biodegradable microparticles as deUvery systems for allergens.
Sameena Sharif

Some new reactions of azidophenyl-heterocycles.
Dong-Fang Shi

The effect of dmgs on polyurethane catheters.
JuUet Smith

The potential use of chitosans as safe and effective nasal absorption promoters.
Tmdi Aspden

Bioadhesion in gastro-intestinal dmg deUvery: Chitosan - a candidate mucoadhesive polymer under scmtiny.
Immo Fiebrig

Peptide derivatives of the anti-tumour unidazotetrazinones.
J Arrowsmith

Methodology in phosphoric acid synthesis.
M Boyd

The surface characterization of regenerated ceUulose and related polymers by scanning probe microscopy.
R Frazier

Percutaneous delivery of Ugnocaine to the newborn.
I Goswami

Development of methodology for the soUd phase synthesis of Argiotoxin-636 and other related spider toxins.
I Nash

The synthesis of potential immunomodulators.
D Hannah

Conti-oUed release of H2 antagonists from bioadhesive chitosan microspheres.
P He

Antibiotic therapy in *Helicobacter Pylori* infection.

M Jessa

The use of SPR and correlative techniques to investigate biomedical interface phenomena.
R Green

ControUed release of protein from resorbable microparticles prepared by novel solvent extraction techniques.
M-K Yeh

Delivery of antisense oligonucleotides using cationic polymer carriers.
F McLaughlin

RadiolabeUing of modified Poloxamer and Poloxamine copolymers.
J Neal

The apphcation of SPM and TEM to smdy Alzheimer's Disease related self-assembling synthetic ß-amyloid (1-40) peptide.
A Shivji

The regidation of multiple phenotypes in *Chromobacterium Violaceum.*
*A* Taylor

Formulation of a viral vaccine.
R Peagram

Novel pharmaceuticals for the treatment of breast cancer.
S Wrigley

Visualizing and measuring dynamic events inside pharmaceutical systems.
L Cutts

A novel carboxy protecting group for peptide syndiesis.
D Evans

Stmcture of flocculated aerosol suspensions in a shear field.
C Bower

Characterization of PLA-PEG copolymers for use as a dmg delivery system.
S Hagan

The ïntegration of computational chemistry tools in computer-aided learning.
R Hyde

Development of a reversible chromatographic probe for potential peptide purification.
B Kellam

Formulation and evaluation of novel amphotericin B emulsions.
M Lance

The characterization of HPLC stationary phase materials.
R Watson